Magnetized Plasma Pressure Filaments: Thermal Diffusion Waves and Multi-Filament Dynamics

by

Scott Graham Karbashewski

A thesis submitted in partial fulfillment of the requirements for the degree of

Doctor of Philosophy

Department of Physics
University of Alberta

Abstract

One of the prominent areas of interest in current plasma science is focused on understanding the mechanisms of heat transport beyond classical Coulomb collisions. The topic has applications in many areas of plasma physics, such as the solar corona and nuclear fusion devices. In strongly magnetized plasmas the thermal conductivity parallel to the magnetic field is numerically quite large and orders of magnitude larger than the transverse conductivity; thus, the effective study of heat transport in these conditions requires a large system that is much longer along the magnetic axis than across. In this thesis, results are presented from basic heat transport experiments using magnetized plasma pressure filaments. The experiments are performed in the Large Plasma Device (LAPD) at the Basic Plasma Science Facility (BaPSF) at the University of California, Los Angeles (UCLA). A cerium hexaboride crystal cathode injects low-energy electrons along a magnetic field into the centre of a pre-existing, cold, quiescent plasma forming a hot electron filament embedded in a colder plasma. Previous experiments observed gradient-driven drift-Alfvén waves that lead to enhanced cross-field transport; and a spontaneous thermal diffusion wave that was speculated to meet a quarter-wave resonance of the filament length.

In the first set of experiments, a low amplitude sinusoidal perturbation is added to the cathode discharge bias that creates an oscillating heat source capable of driving large amplitude electron temperature oscillations. Langmuir probes are used to measure the amplitude and phase of the thermal wave field over a wide range of driver frequencies. The results are used to verify the excitation of thermal waves in magnetized plasma and confirm the presence of thermal resonances of the filament. The diagnostic potential of thermal waves is demonstrated through measurement of

the parallel thermal diffusivity and distinguishing between classical transport, drift-Alfvén growth, and turbulent transport regimes using the cross-field structure. Two models for the thermal wave field are investigated and used to describe the experiment results; a two-dimensional homogeneous model based on a Green function approach and a one-dimensional inhomogeneous model based on a classical mechanics approach using the Hamilton-Jacobi equation.

The second set of experiments have used three crystal cathodes in a triangular configuration to investigate the interactions between multiple pressure filaments with varying separation distances. The results are used to establish the scale length of interaction between the filaments. Within an electron skin depth, enhanced cross-field transport from chaotic $\mathbf{E} \times \mathbf{B}$ mixing rapidly relaxes the gradients in the inner triangular region of the filaments and leads to the growth of global nonlinear drift-Alfvén modes that are driven by the thermal gradient in the outer region of the filament bundle. Linear stability analysis of the temperature, density, and transverse flow profiles is used to accurately predict the observed wave modes. Coupling between the global modes leads to large intermittent transport events that are characterized by exponential frequency spectra and Lorentzian-shaped pulses that are signatures of chaotic dynamics. Mode decomposition and conditional averaging are used to reconstruct the pulse events and demonstrate that they are driven by nonlinear interactions between drift-Alfvén wave modes. The time series analysis tools of the complexity-entropy plane and Hurst exponent are used to investigate the chaotic nature and memory of the intermittent fluctuations. Last, the addition of a sinusoidal driver to one of the filaments in the configuration facilitates driving of the drift-Alfvén modes. The driver is shown to synchronize with several eigenmodes at once due to the asymmetric perturbation.

Preface

This thesis is an original work by myself, Scott Karbashewski, with the research completed in collaboration with a team of researchers: Prof. Richard D. Sydora at the University of Alberta was the principal investigator; Dr. Bart Van Compernolle was a staff scientist at the Basic Plasma Science Facility (BaPSF) at the University of California, Los Angeles (UCLA) where the experiments contained in this thesis were performed and is now at General Atomics; and Dr. Matthew Poulos was a UCLA graduate student engaged in modelling the experiments and is currently at Princeton Plasma Physics Laboratory. Our team was supported by the BaPSF staff and several individuals: Prof. George Morales at UCLA, who acted in an advisory role; Patrick Pribyl, Avdit Kohli, and Trevor Karbashewski, who assisted with the electronic hardware; and undergraduate students Thomas Simala-Grant, Jared Loughran, Aparajit Gnanasekaran, Samraat Thakur, Drew Bremeault, and Nurlan Rzayev, who completed research projects related to the work presented herein.

Much of the work presented in this thesis has been published as articles in academic journals. These articles are not reproduced in whole within this thesis; however, significant portions are contained throughout the chapters. Adjustments and additions have been made to the original text to expand on the details of the research and create a more cohesive document.

Finally, it is my opinion that it is a failing of the plasma physics community to have not widely adopted the International System of Units (SI) over the cgs-Gaussian system that dominates the field. While saying nothing of the advantages of adopting SI, one simple example that illustrates the need to discard the cgs-Gaussian system is the "statcoulomb", which gives electric charge the incomprehensible dimensions: $[\text{length}]^{3/2}[\text{mass}]^{1/2}[\text{time}]^{-1}$. Advocating for a widespread change in the field is not an objective of this thesis and I have chosen to follow the current unit conventions. Thus, units such as the erg (1×10^{-7} joules), the gauss (1×10^{-4} tesla), and the electronvolt ($11,605$ kelvin) will make appearances; the last is neither a cgs-Gaussian nor SI unit but remains a common measure of plasma temperature in the dimension of energy. Perhaps one day a physicist reading this will also have to consult a history book.

Table of Contents

List of Figures

Publications

[1] S. Karbashewski, R.D. Sydora, B. Van Compernolle, and T. Simala-Grant "Time-Series Analysis of Intermittent Transport Events in Bundled Plasma Pressure Filaments", IEEE Transactions on Plasma Science **Submitted** (2021)

[2] S. Karbashewski, R.D. Sydora, B. Van Compernolle, and M.J. Poulos, "Stimulated Excitation of Thermal Diffusion Waves in a Magnetized Plasma Pressure Filament", Physics of Plasmas **28**, 092112, (2021)

[3] R.D. Sydora, S. Karbashewski, B. Van Compernolle, M.J. Poulos, and J. Loughran, "Drift-Alfven Fluctuations and Transport in Multiple Interacting Temperature Filaments", Journal of Plasma Physics **85**, 905850612 (2019)

[4] S. Karbashewski, R.D. Sydora, B. Van Compernolle, and M.J. Poulos, "Driven Thermal Waves and Determination of the Thermal Conductivity in a Magnetized Plasma", Physical Review E **98**, 051202 (2018)

[5] R.D. Sydora, B. Van Compernolle, S. Karbashewski, G.J. Morales, and J.E. Maggs, "Nonlinear Convective Heat Transport in Multiple Magnetized Electron Temperature Filaments", Problems of Atomic Science and Technology **23**, 100 (2017)

CHAPTER 1.

Introduction

A plasma is a state of matter best described as a gaseous collection of positively charged ions and negatively charged electrons. Plasmas are electrically conductive and interact strongly with electromagnetic fields to produce complex motions and structures. Some common plasma examples are neon signs, lightning, auroras, stars, and fusion reactor cores. A prominent area of research in plasma physics is electron energy transport or understanding how heat within a plasma is transported to the rest of the volume. Classical diffusive transport in plasmas is facilitated by Coulomb collisions between particles; however, experimental studies of transport rates across the field lines of magnetized plasmas are often higher than classical predictions when large temperature gradients are involved. Thus, there is a need to improve the understanding of mechanisms of heat transport in magnetized plasmas beyond classical Coulomb collisions. These so-called anomalous transport processes are often associated with filamentary structures that exist in an array of plasma environments, ranging from the naturally occurring plasmas of the solar corona [1, 2] and planetary aurora [3–5] to laboratory plasmas produced in magnetic confinement fusion devices [6–10].

Naturally occurring plasmas and high-temperature fusion experiments are complex systems, difficult to reliably reproduce, and limited in diagnostic capabilities; these characteristics make them ill-suited for the controlled study of transport phenomena. Further complicating the problem, in strongly magnetized plasmas the thermal conductivity parallel to the magnetic field is numerically very large and several

orders of magnitude larger than the transverse conductivity [11]; thus, a basic laboratory study of heat transport in magnetized filamentary structures requires a large system that is much longer along the magnetic axis than across.

The research of this dissertation is based on a series of basic, low-temperature laboratory plasma experiments in a long, linear, solenoidal device using small heat sources to create plasma pressure filaments. These experiments have the unique ability to study isolated filamentary structures and related transport phenomena in detail and offer the opportunity to validate theory and modelling. The heat sources can be used to study a range of transport phenomena, including the generation of drift wave turbulence and chaotic dynamics; the interactions of multiple filaments leading to enhanced convective transport; and the driving of thermal waves and their diagnostic uses in measuring the thermal conductivities. In addition to executing and analyzing the experiments, this research entails the development of analytical models of the thermal wave field in a magnetized plasma in homogeneous and inhomogeneous plasmas with anisotropic thermal conductivities.

1.1 Pressure Filament Experiments

The experiments that are the focus of this research are performed in the Large Plasma Device (LAPD) [12] at the Basic Plasma Science Facility (BaPSF) at the University of California, Los Angeles (UCLA). The LAPD is a linear plasma device that produces a cylindrical, quiescent magnetized plasma column that is 18 m long and 60 cm in diameter – making it ideal for simultaneous study of axial and radial transport. The experiments consist of a small crystal cathode inserted in the vacuum chamber that injects a thermionic electron beam into a cold, afterglow-plasma generating a heat source that rapidly conducts along the axial magnetic field lines of the LAPD to produce a long filamentary structure with steep radial (cross-field)

temperature gradients. The size of the LAPD confinement chamber in comparison to the pressure filament embedded in the plasma eliminates the effects of the chamber walls and plasma edge dynamics, creating a controlled environment for studying the filament evolution.

Over the past two decades, a series of nearly identical experiments have been performed in the LAPD, with each rendition building on past results [13–20]. Previous work established that after a period of classical transport [16] the temperature gradients become unstable and drive the growth of drift-Alfvén wave modes, a hybrid mode composed of pressure gradient drift waves and magnetic Alfvén waves [21]. The drift-Alfvén wave modes enhance the cross-field transport and eventually lead to a turbulent state [17]. The turbulent temporal signals are characterized by exponential frequency spectra and intermittent transport events with Lorentzian shaped pulses [19, 20] that are associated with chaotic dynamics [22]. Additionally, the filament experiences low-frequency excitation of thermal oscillations that are highly localized to the centre of the filament [15]; this thermal mode was identified as a spontaneous thermal wave [18] and modelling of the filament has suggested that the frequency of this mode meets a quarter-wave resonant condition for the length of the filament.

The current rendition of experiments aims to investigate the use of a perturbation to the electron beam heat source to drive thermal waves and to study the transport dynamics and interactions between multiple filaments. Central to this work is the replication of past results; this establishes continuity and reproducibility of the experiments and is vital for providing a base case of study before extending to the driven excitation of thermal waves and multiple heat source experiments.

1.2 Thermal Waves

There exists an unconventional class of waves known as thermal diffusion waves, or simply thermal waves, that are produced using sinusoidally, time-varying heat sources [23]. First observed by Ångström in 1862 [24], thermal waves remained largely unstudied for nearly the next century due in part to their heavy spatial attenuation and limited technology for performing accurate and precise experiments. The first-order time derivative in the heat equation instead of the familiar second-order time derivative in the traditional wave equation gives thermal waves unique properties, such as infinite phase speed, an accumulation-depletion law instead of a reflection-refraction law at boundaries, and the aforementioned heavy spatial attenuation [25]. Since the arrival of the laser, a variety of novel techniques for observing thermal waves in condensed and gaseous matter have been developed, with an emphasis on diagnostic applications[25, 26].

These recent advancements resulted in the construction of thermal wave resonator cavities (TWRCs) [27] capable of sustaining quasi-standing thermal waves. Driven thermal resonators in conjunction with frequency and cavity length scanning [28] have been used to measure the thermal properties of solids [29], liquids [30], and gases [31]. The materials science community has created other novel technologies such as thermal wave depth profiling [32] used to detect subsurface material defects [33] and reconstruct inhomogeneous material conductivities [34]; carrier-diffusion wave methods for analyzing ion implantation in semi-conductors [35]; and biomedical applications for measuring bone composition[36], blood glucose levels [37], and tooth decay detection[38].

The overwhelming success of thermal wave diagnostic techniques with different forms of matter motivates the application of similar methods to magnetized plasma

where electron heat transport processes are a central research topic and of particular importance to magnetic confinement fusion devices [39]. The potential of thermal waves in plasmas remains largely untapped but has seen some attention in pulsed heating experiments in large fusion devices [40–47].

Recent LAPD pressure filament experiments [18] reported that the filament behaves as a TWRC in the axial direction and exhibits spontaneous thermal fluctuations meeting the conditions for a quarter-wavelength resonance of the filament length. The conclusion of Ref. [18] suggests the development of oscillatory electron beam sources for probing anomalous transport phenomena with thermal waves. While advanced thermal wave diagnostics for plasmas are not yet attainable, practical advancement towards thermal wave diagnostics in the plasma regime includes experimentally demonstrating the stimulated excitation of thermal waves in plasma and illustrating the diagnostic potential.

Much of the body of knowledge on thermal waves is dedicated to homogeneous problems in one or more dimensions [23], though there exist promising approaches to one-dimensional modelling of thermal waves in inhomogeneous media [32, 48, 49]. The heat transport in the pressure filaments, and many plasma problems, is inherently an inhomogeneous and anisotropic system that presents significant challenges to both experiment analysis and modelling. A more complete understanding of thermal waves in the plasma regime and successful implementation of diagnostics based on thermal waves will require the development of multi-dimensional thermal wave field models with inhomogeneous and anisotropic thermal conductivities.

1.3 Turbulence and Intermittent Transport

From detailed measurements in the laboratory and by satellites, filamentary structures are often associated with turbulent fluctuations that are spontaneously generated through free energy sources, such as gradients in their macroscopic plasma parameters [3, 13, 17, 50]. The properties of turbulence appearing in such structures is relevant to the plasma edge region of magnetic confinement devices where large fluctuation bursts and cross-field blob and filament transport is connected with non-linear interactions of Alfvénic fluctuations [10, 51]; in particular, at the boundary of fusion plasmas, radially propagating filaments are believed to dominate the transport across the scrape-off layer (SOL) [52]. In the last two decades, there is mounting experimental evidence from toroidal and linear magnetized plasma devices that coherent structures in the plasma turbulence, referred to as blobs or magnetic field-aligned filaments, lead to intermittent convective cross-field transport of particles, energy, and momentum [53]. The transverse scale of filamentary plasma structures can vary widely, from the collision electron skin depth to several times the ion Larmor radius. Plasma non-uniformities on these scales can induce low-frequency excitations such as drift-Alfvén waves and vortices [54].

The excitation of drift-Alfvén wave modes has previously been investigated using the temperature filament [14, 15, 17, 19, 20]. In the transition from classical transport to a turbulent regime localized drift-Alfvén eigenmodes are driven unstable by the temperature gradient in the filament edge. As the plasma conditions change the highly coherent eigenmodes evolve into broadband drift-Alfvénic turbulence [19, 20], often associated with coupling between multiple wave modes in experiments [55–57] and modelling [58–60]. The broadband turbulence is characterized by an exponential frequency spectrum and intermittent Lorentzian shaped pulses that are signatures of

chaotic dynamics [22]. The chaotic temporal signals and Lorentzian pulses are part of a larger body of evidence that the plasma edge or gradient turbulence is inherently a deterministic chaotic process [61–63].

The experiments motivated numerical modelling studies of $\mathbf{E} \times \mathbf{B}$ advection in the potential fields of low-frequency drift waves [64]. It was found that above a certain threshold amplitude the interaction of spatially and temporally coherent drift waves resulted in advecting structures and chaotic particle orbits [61]. The temporal signal of the temperature fluctuations constructed from these orbits consists of Lorentzian-shaped pulses which have a frequency spectrum that is exponential and consistent with diagnostic probe measurements [19, 20, 22, 61, 63]. This study was followed by three-dimensional gyrokinetic simulations of cross-field transport driven by drift-Alfvén waves in a single magnetized temperature filament [65]. The simulations demonstrated the excitation of convective cells from non-linear drift-Alfvén mode interactions and enhanced cross-field transport through $\mathbf{E} \times \mathbf{B}$ advection in the filament.

Filamentary structures that occur naturally in plasmas are generally not isolated but may occur in bundles, unlike past experiments; this motivates the study of interactions between multiple filamentary structures. Controlled studies in the LAPD offer the opportunity to study the scale lengths of interaction between the drift-Alfvén eigenmodes, perform statistical analyses of turbulent fluctuations, and further investigate the deterministic chaotic nature of intermittent transport events.

1.4 Objectives

The objective of this work is to address two problems in plasma science using basic laboratory experiments: (i) development of diagnostic methods capable of making direct measurements of thermal transport coefficients in magnetized plasma; (ii) improved understanding of the dynamics of enhanced thermal transport associated with filamentary structures occurring in natural and laboratory plasmas. The complexities of natural and high temperature laboratory settings create difficulties in addressing these problems; the basic, controlled experiments presented here are well-suited for detailed investigations that can be compared with models. Below, the main outcomes of our experiments in pursuit of these goals are highlighted.

(i) The materials science community has developed accurate and reliable diagnostic techniques using thermal diffusion waves. In our experiments, we extend these techniques to the plasma regime with the main goal of using a modulated electron beam heat source to drive thermal waves in a magnetized plasma pressure filament. To successfully achieve this we design a system for adding the modulation to the source; characterize the response of the source and plasma filament to modulation; and compare the experimental results with models to confirm the excitation of thermal waves. We demonstrate the diagnostic potential of thermal waves by measuring the parallel thermal diffusivity of the magnetized plasma; central to this outcome is the construction of a homogeneous and anisotropic model of the thermal wave field using a Green function approach. The driven thermal waves are used to investigate the previously observed thermal resonance. Frequency scanning confirms the presence of thermal resonances; measurements of the filament length demonstrate the resonance conditions; and broadband pulsing is shown to excite a ringing of the natural resonant frequency. We make detailed measurements of the cross-field structure of the thermal

wave field to show that thermal waves can be used to distinguish between classical and anomalous transport regimes. To describe the complex features of the cross-field wave field an inhomogeneous model is constructed by treating the heat equation as a thermal harmonic oscillator and solved using a classical mechanics Hamilton-Jacobi approach.

(ii) Past filamentary experiments have demonstrated there is a transition from classical transport to a turbulent state due to the interaction of gradient-driven drift-Alfvén modes. Our experiments extend the past work to the situation of multiple filamentary structures. To perform such studies several crystal cathodes for producing the filaments are arranged in the plasma to generate the desired filament configurations. The separation distance between the filaments is varied to identify the scale length of interaction. We characterize the evolution of the plasma density, temperature, and space potential when the filaments are in a tight bundle and highly interactive. In this configuration, we observe the growth of global drift-Alfvén waves around the filament bundle. Linear stability analysis of the pressure profile in the presence of shear flows is used to predict the observed modes. The coupling between these modes leads to a turbulent state and the probability distribution function is used to show the fluctuations are characterized by intermittent pulses. These events are shown to have a Lorentzian shape and exponential spectra that are associated with chaotic dynamics. Conditional averaging is used to perform a spatiotemporal reconstruction of a single event and provides evidence that the pulse structures are generated by interactions among the drift-Alfvén modes. Last, we use the tools of the complexity-entropy and Hurst exponent to reveal the chaotic nature and dual time-scale memory of the turbulent fluctuations.

1.5 Thesis Outline

In the next chapter, Chapter 2, we begin with a presentation of the experimental methods. This entails a description of the Large Plasma Device, the diagnostics used for these experiments, and the crystal cathode sources and electronics. The chapter ends with an overview of the single filament dynamics investigated in past experiments. In Chapter 3 the models developed for the thermal wave experiments are presented. This begins with a description of the heat transport equation in a magnetized plasma followed by the two approaches investigated: a two-dimensional, homogeneous, and anisotropic model based on Green functions; and a one-dimensional inhomogeneous model based on a thermal harmonic oscillator description, extensions to a two-dimensional, inhomogeneous, and anisotropic model are discussed. Chapter 4 reports the results and analysis procedures of the driven thermal wave experiments performed to meet the first objective outlined above. Chapter 5 presents the observations and analysis of the multi-filament experiments carried out in pursuit of the second objective. Finally, this thesis and possible extensions on the results herein are summarized in Chapter 6.

CHAPTER 2.

Experimental Methods

2.1 Experiment Setup

2.1.1 The Large Plasma Device (LAPD)

The upgraded Large Plasma Device[12] (LAPD) is pictured in Fig. 2.1 and represented schematically in Fig. 2.2(a). The cylindrical vacuum chamber is filled with helium (He) gas and encircled by electromagnets that produce a background magnetic field. A hot barium oxide (BaO) coated cathode is mounted at one end of the chamber with a mesh anode 50 cm away. The main plasma column is created using a bias on the order of -70 V at the cathode with respect to the anode that causes thermionic emission of electrons from the cathode. The accelerated electrons stream through the mesh anode into the main plasma chamber and collisionally ionize the He gas filling the chamber and create a magnetically confined plasma column 18 m in length and 60 cm in diameter. The electron temperature in this phase is $T_e \sim 5$ eV, the density is $n \sim 2 \times 10^{12}$ cm^{-3}, and the ion temperature, T_i, is less than 0.5 eV. The main discharge phase lasts for 12 ms before the bias is eliminated and the plasma enters the afterglow phase. The LAPD is a pulsed device and the discharge is repeated at a

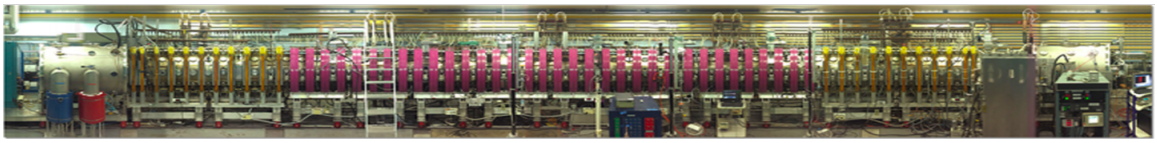

Figure 2.1: Image of the Large Plasma Device from Reference [12].

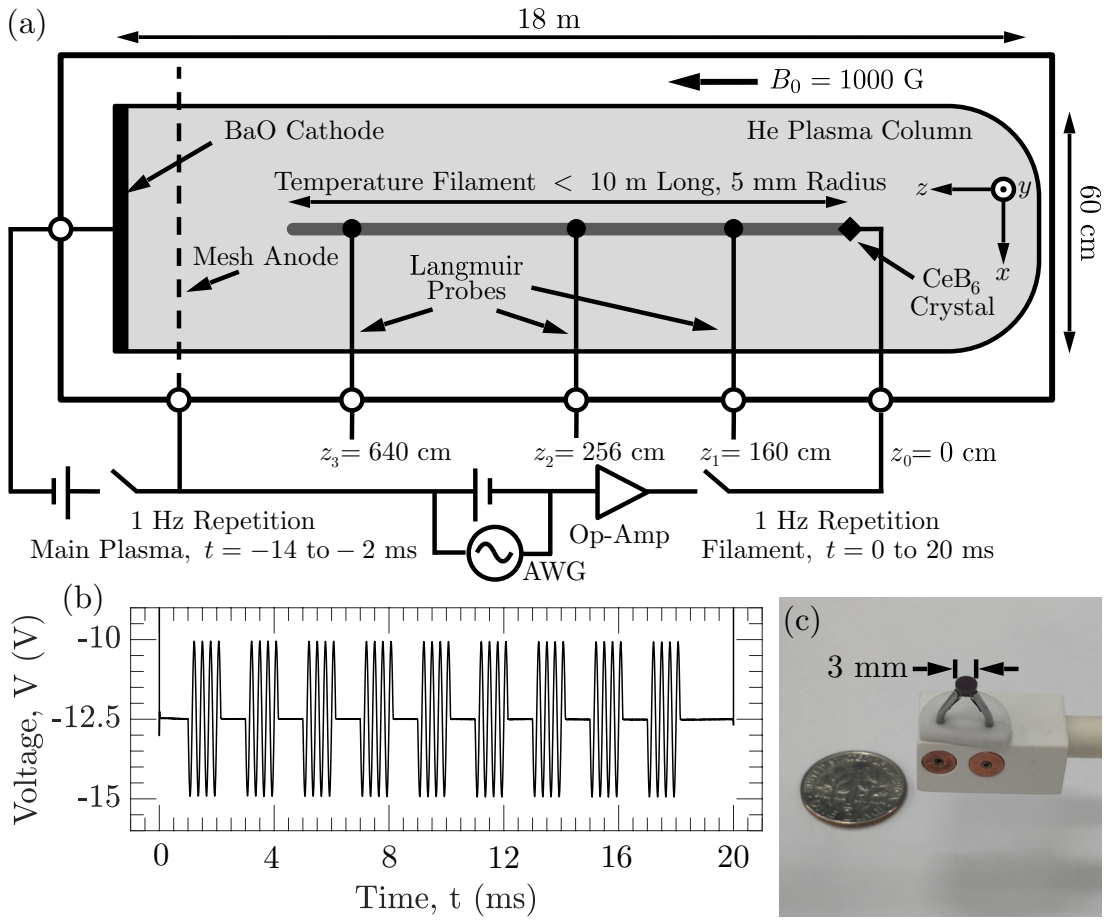

Figure 2.2: (a) Schematic (not to scale) of the experimental setup on the LAPD. (b) The discharge voltage applied between the CeB_6 crystal and the mesh anode to generate an oscillating heat source. (c) Image of the CeB_6 crystal mounted on the end of a probe shaft and next to an American dime for scale.

1 Hz rate, 24 hours a day, and 7 days a week with a high degree of reproducibility.

The evolution of the background plasma temperature and density during the afterglow is depicted in Fig. 2.3 where the end of the main plasma discharge is observed at $t = -2$ ms followed by a rapid transition to the afterglow. The plasma rapidly cools to T_e less than 0.25 eV and the density decays exponentially with a time constant on the order of 10 ms. This cold, quiescent plasma is the phase where our experiments are conducted and the parameters of the afterglow are summarized in Table 2.1.

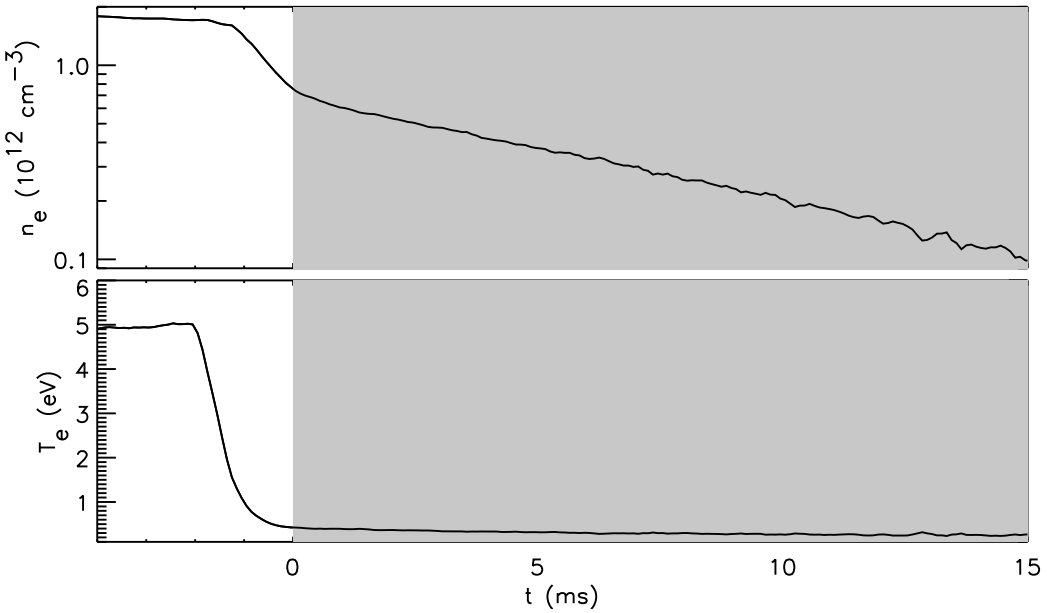

Figure 2.3: Temporal evolution of the (a) density and (b) electron temperature of the afterglow plasma phase of the LAPD cycle.

Table 2.1: Parameters in the LAPD Helium Afterglow Plasma

Parameter	Symbol	Value
Magnetic Field	B_0	1 kG (0.1 T)
Vacuum Fill Pressure	p_v	$\sim$ 0.15 mTorr (0.02 Pa)
Neutral Density	n_n	$\sim 4 \times 10^{12}$ cm^{-3}
Plasma Density	n	$\sim 1 \times 10^{12}$ cm^{-3}
Electron Temperature	T_e	≤ 0.5 eV
Ion Temperature	T_i	≤ 0.5 eV
Electron Plasma Frequency	$\omega_{pe}/2\pi$	9 GHz
Ion Plasma Frequency	$\omega_{pi}/2\pi$	1 MHz
Electron Cyclotron Frequency	$\Omega_e/2\pi$	2.8 GHz
Ion Cyclotron Frequency	$\Omega_i/2\pi$	384 kHz
Electron Skin Depth	δ_e	0.53 cm
Alfvén Speed	v_A	1.1×10^8 cm/s
Ion Acoustic Speed	c_s	5×10^5 cm/s
Ion Sound Length	ρ_s	0.2 cm

2.1.2 Filament Creation

Each of the filamentary plasma structures is created using a 3-mm-diameter crystal cathode of cerium hexaboride (CeB_6) mounted on a probe shaft and inserted into the plasma 1500 cm from the BaO source axially and roughly centered in the transverse plane of the chamber. The schematic in Fig. 2.2(a) shows the setup with a single cathode and in Fig. 2.2(c) is a mounted crystal next to an American dime for scale. The crystal is supported by current carrying wires mounted on a ceramic base that has been slightly modified to a semi-circle shape. The modified ceramic base is being held by a boron nitride rectangular prism mounted on a probe shaft. The rigid wire mounts are connected to insulated wires inside the prism that extend through the probe shaft to outputs accessible from the end of the probe outside the LAPD vacuum chamber. CeB_6 has a low work function and high electron emissivity when it is heated to an operating temperature of around 1400 °C; the heating is accomplished ohmically with around 10 W of power to the crystal using a dc power source.

Starting 2 ms after the main discharge, indicated by the shaded grey region in Fig. 2.3, the crystal cathode is biased at varying discharge voltages < 20 V below the mesh anode for 15–20 ms, injecting thermionic electrons with energy below the ionization energy of helium (24.6 eV). The beam injection time, 14 ms into the LAPD cycle, is established as time $t = 0$ for the filament experiments. The low-energy electron beam thermalizes in the region of plasma in front of the CeB_6 source creating a hot temperature plume < 1 m in extent and a few millimeters in diameter. The thermal conduction in a magnetized plasma is anisotropic and characterized by the parallel and cross-field (perpendicular) classical thermal conductivities ($\kappa_\parallel, \kappa_\perp$) [11]. The extent of anisotropy in the conductivities is related to T_e and B_0 through the

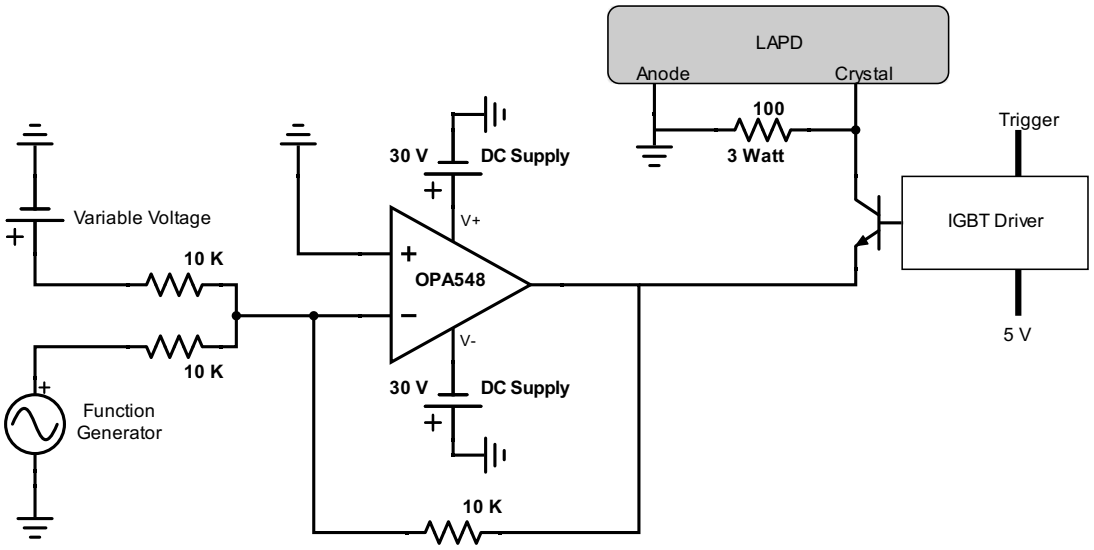

Figure 2.4: Circuit designed for adding modulation to the bias applied to the crystal cathodes. Circuits designed and built by S. Karbashewski, electronics box assembled by T. Karbashewski.

proportions $\kappa_\parallel \propto T_e^{5/2}$ and $\kappa_\perp \propto n^2 T_e^{-1/2} B_0^{-2}$; the anisotropy is typically on the order of 10^6. Thus, thermal transport rapidly conducts heat down the length of the device with minimal radial diffusion creating a filamentary region of elevated temperature and density less than 10 m in length with a symmetric, Gaussian-like transverse profile less than 2 cm in diameter. The peak temperature near the heat source is 3–5 eV depending on the bias voltage and decreases continuously toward the end of the filament where the temperature equilibrates with the cold background plasma.

The most recent experiments noted a barrier to investigating thermal waves further was encountered when trying to modulate the electron beam [66]. We designed the current electronic hardware with the ability to easily modulate the bias of the crystal cathode with respect to the anode. This is accomplished using a high-voltage, high-current operational amplifier (op-amp) and an arbitrary waveform generator (or

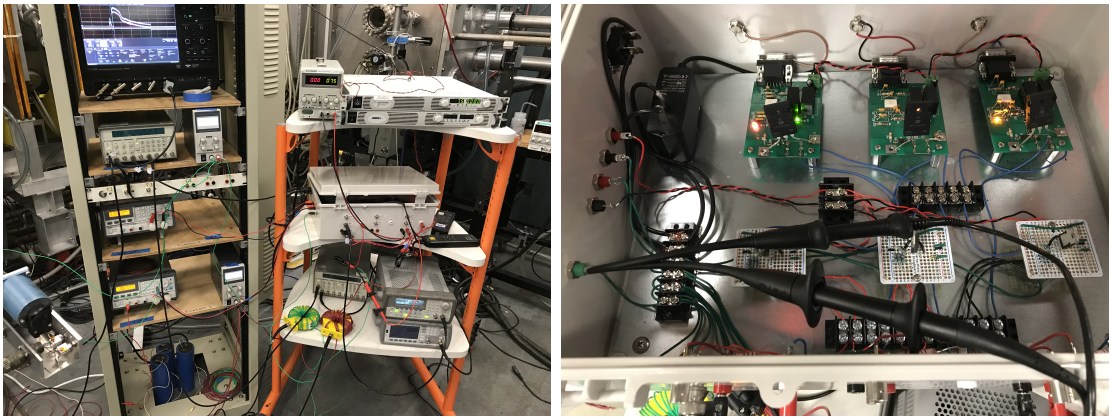

Figure 2.5: (Left) Electronic hardware for heating and biasing the temperature filaments. (Right) Interior of electronics box housing the IGBT and op-amp circuits.

function generator). The circuit designed for this application is shown in Fig.2.4. The op-amp outputs the addition of a variable dc bias voltage and arbitrary signal from a function generator. The output signal of the op-amp is only applied to the crystal cathode when a triggering pulse is applied to the isolated gate bipolar transistor driver (IGBT driver). The full hardware setup for heating and biasing the CeB_6 cathode(s) is shown in the left image of Fig. 2.5; on the right is an image of the inside of the electronics box housing three identical circuits for biasing up to three crystal cathodes independently.

In previous experiments only constant discharge voltages were used for creating the filaments and are defined as "dc shots" throughout this document. Using the operational amplifier to add an arbitrary signal to the dc bias creates an oscillating beam current (and, by extension, an oscillating heat source). The modulation frequency f_{ac}, is kept below 65 kHz ($\omega_{\mathrm{ac}} < 0.17\Omega_i$ where Ω_i is the ion cyclotron frequency). Plasma shots with added signals are referred to as "ac shots" throughout this document. Chapter 4 reports primarily on experiments where the ac signal is a single frequency sinusoid added in the form of pulses $\sim$ 1 ms long and spaced 1 ms apart;

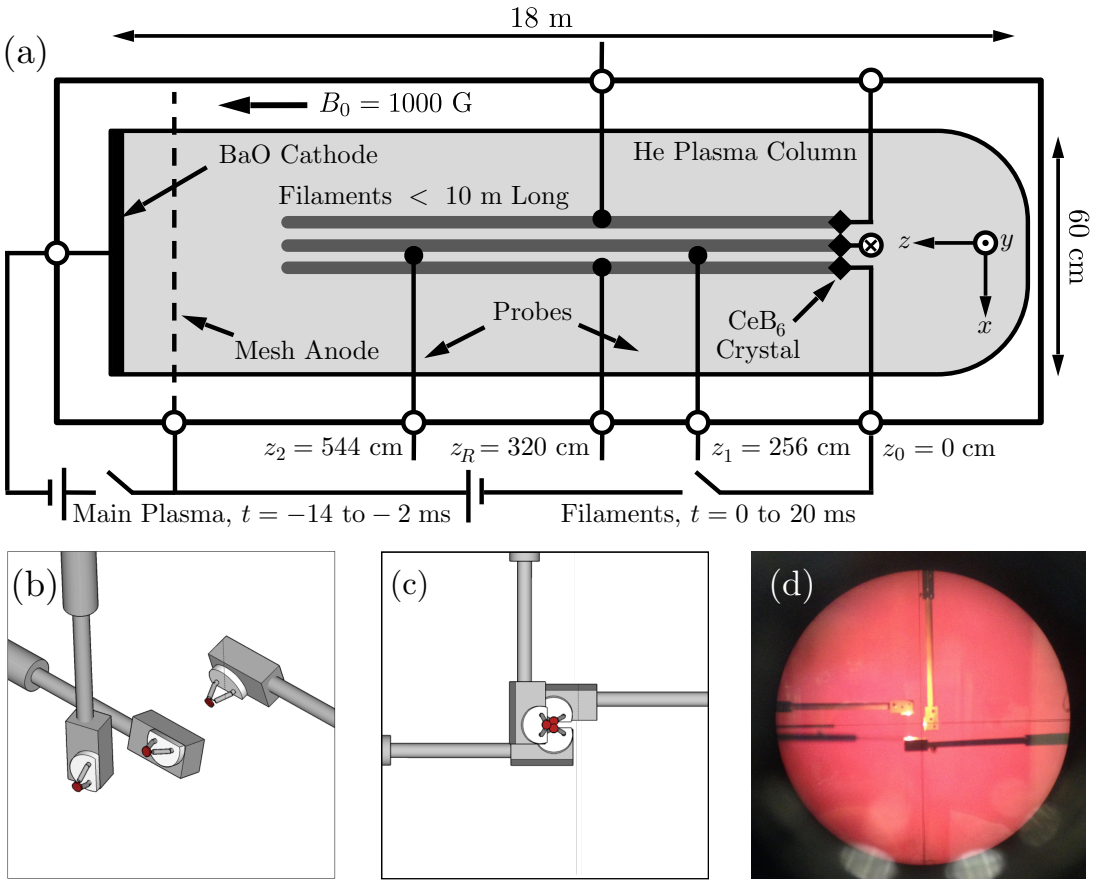

Figure 2.6: (a) Schematic of the experiment setup on the LAPD (not to scale). The probes with crystal cathodes on the end are inserted through ports on the east, west, and top of plasma chamber. (b) View of the cathode probes from an angle showing the axial offset and angling of the tips. (c) z-axis view of the crystals in the closest configuration. (d) Axial image of the crystals separated seen from a scope looking through a viewing port opposite the anode.

an example of this cathode bias is displayed in Fig. 2.2(b) with a 12.5 V dc offset, 2.5 V ac amplitude, and ac frequency of 7 kHz. Additionally, Section 4.1.3 reports on the results of short, broadband pulses applied to the discharge.

To align three of the crystals in the LAPD at once one probe is inserted from each side of the device and one from the top, this is shown schematically in Fig. 2.6(a). The mounting structures and probe shaft geometry were designed such that the CeB_6

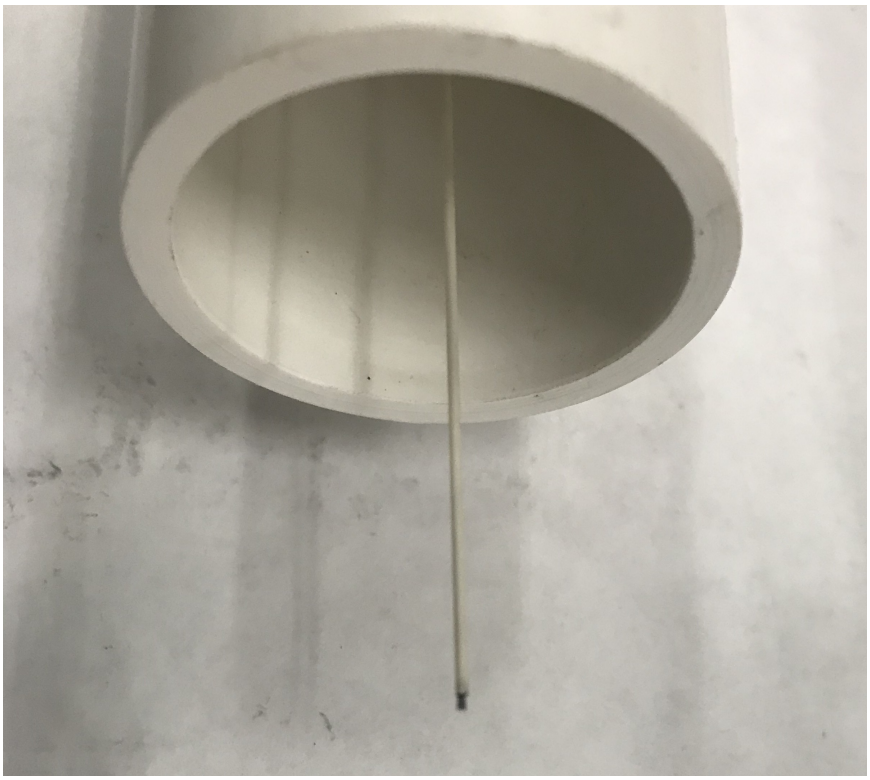

Figure 2.7: Image of a small Langmuir probe used in the experiments.

crystals can be positioned arbitrarily close to each other when viewed along the magnetic field line (z-axis), as shown in Fig. 2.6(c). In order to achieve this, the crystals are set-back by a few cm in the z-direction (Fig. 2.6(b)). From the position shown in Fig. 2.6(c) the crystals can be separated to any inter-crystal distance required by the experiment. The image in Fig. 2.6(d) is taken through a surveying scope aligned along the axis of the LAPD and shows the crystals aligned in a quasi-symmetric filament bundle with diagnostic probes visible in the distance. The aligning of the probes is completed manually by three team members: one manually moving the probes, one checking the alignment through the scope at the end of the device, and one relaying the communication over the noise of the laboratory equipment.

2.1.3 Diagnostics

The LAPD has access ports spaced 32 cm apart along the axial length of the device. The most common probe used in our experiments is the Langmuir probe with a small, flat, metallic face or tip with an area ~ 1 mm^2 and pictured in Fig. 2.8. The Langmuir probes are inserted into the access ports to sample the temporal evolution of plasma parameters. Due to the high repetition rate and high reproducibility of the plasma a probe at axial location z can be placed at one position in the transverse (x, y) plane, collect several nearly identical shots, then be moved to a new position and repeat the process. The shots from one position create an ensemble average of the measurement. The process of moving the probes and collecting the data is entirely automated with the probes mounted on probe drives capable of 0.5 mm accuracy.

The operation of the Langmuir probe was first described by Harold Mott-Smith and Irving Langmuir in 1926 [67]. The probe operates by collecting a current from the plasma that can be related to the plasma parameters. Varying the bias (with respect to the machine walls) on the probe and measuring the collected current results in a characteristic I–V curve with an example provided by the blue diamonds in Fig. 2.8; the current scale is inverted and thus the electron current is positive and the ion current is negative, this is common practice within plasma physics. The curve has five main features, indicated in the figure: (i) Floating potential, V_f, is where the probe collects no current and is easily identifiable. (ii) Space potential, V_s, is the potential of the plasma with respect to the machine walls. In a plasma with zero temperature the space and floating potentials would be equal, however, in reality V_f is slightly lower than the space potential due to the higher thermal speed of electrons compared to ions. V_s can be approximated through several techniques, most commonly where the second derivative of the curve is zero [68]. (iii) Ion saturation current, I_{sat}, is

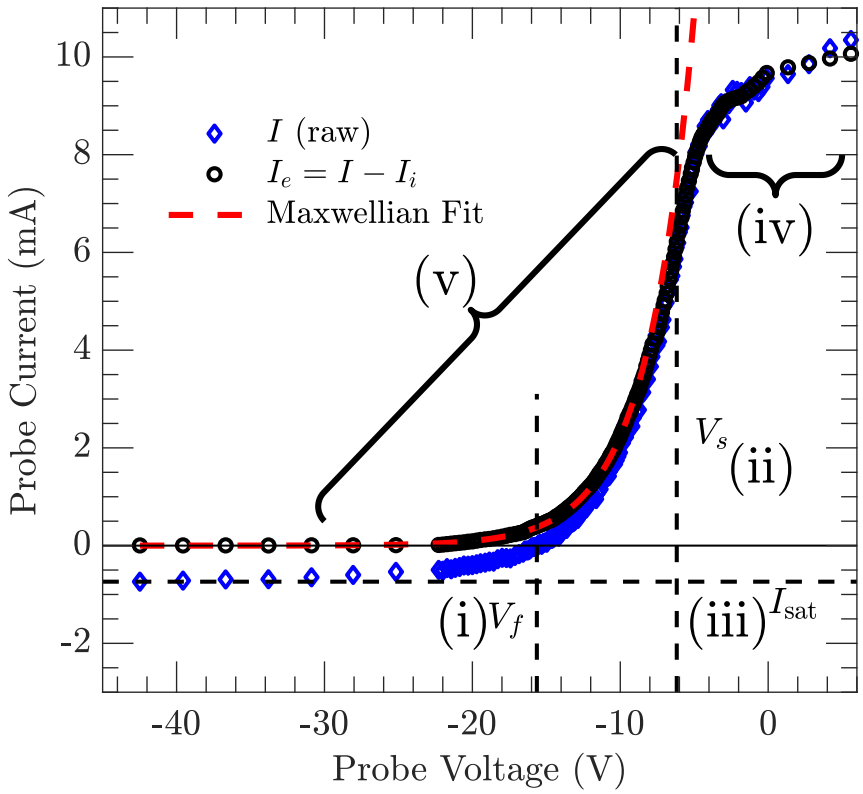

Figure 2.8: Example of a reconstructed Langmuir probe I–V curve. The blue diamonds represent the raw current collected by the probe, the black circles are the adjusted electron current, and the red dashed line is the Maxwellian fit to the electron current. The main features described in the text are labelled by the roman numerals (i)–(v).

the current limit when the probe is biased sufficiently below the space potential. The negative bias repels all the electrons and only ions are collected; $I_{\rm sat}$ is easily identified in the I–V curve and has the relation $I_{\rm sat} \propto n\sqrt{T_e}$ [69]. (iv) Electron saturation current, $I_{\rm esat}$, occurs when the probe is biased above V_s and all the ions are repelled. In practice, $I_{\rm esat}$ does not saturate at V_s in high density plasmas (such as the LAPD) and continues to increase as the sheath around the probe expands and begins to perturb the plasma; thus, the electron saturation is not particularly useful and the large currents are damaging to the probes and avoided when possible. (v)

the transition region between V_s and $I_{\rm sat}$ is where only some electrons are repelled by the probe and can be used to extract information about the electron distribution. If the plasma is Maxwellian the electron contribution to the current, I_e, will have the relation $I_e \propto \exp[e(V - V_s)/kT_e]$, where k is the Boltzmann constant. A fit to the ion saturation region can be used to approximate the ion contribution I_i [68] and remove it from the total current to give a measure of I_e, shown by the black circles in Fig. 2.8. The I_e current can be fit to an exponential (in practice, a linear line on a log-linear plot) to give an accurate measure of T_e, and when combined with $I_{\rm sat}$ the density can also be determined.

Three types of measurement techniques are used with Langmuir probes, ion saturation current, temporal Langmuir sweeps, and reconstructed Langmuir sweeps. In the first, $I_{\rm sat}$ is continuously collected by the probe to sample high temporal resolution fluctuations in the plasma. Often, $I_{\rm sat}$ measurements (and other quantities) are reduced to a fluctuating component, δI_{sat}, by removing frequency content below $\sim$ 1 kHz, and a time-averaged component $\langle I_{\rm sat}\rangle$ so that $I_{\rm sat} = \langle I_{\rm sat}\rangle + \delta I_{\rm sat}$. The brackets indicating time-averaging, $\langle ...\rangle$, may be dropped for convenience where fractional amplitudes, $\delta I_{\rm sat}/I_{\rm sat}$, are used. Temporal Langmuir sweeps are acquired by repeatedly varying the probe voltage in a linear saw-tooth over a short time scale (200–400 μs) to obtain measurements of n, T_e, V_s, and V_f using the I–V curve techniques described above; this method only requires 5-10 shots at each position but has a poor temporal resolution and the fitting can be inaccurate in plasmas with high fluctuations. An ensemble-averaged instantaneous I–V curve may be reconstructed from many thousands of shots at a single position taken over a range of probe voltages. These so-called reconstructed sweeps are time intensive and impractical to implement at many positions but are necessary to obtain a high temporal resolution of plasma parameters. The data in Fig. 2.8 are an example of a reconstructed sweep and depict

a single time step composed of nearly 5000 plasma shots.

The LAPD is equipped with numerous other diagnostics for monitoring the plasma discharge, gas content, pressure, main cathode temperature, background magnetic field, and other machine state variables. Vital for calibrating the Langmuir probes are a series of interferometers that collect the integrated density of transverse lines of the plasma column; the line integrated density can be compared with full machine lines of I_{sat} from the Langmuir probe in the cold afterglow where the temperature across the plasma column is constant. Rogowski coils are used for measuring the filament discharge current and voltage sensors for measuring the crystal cathode biases. Last, some measurements are made using two-sided or six-sided Mach probes for determining the plasma flow velocity, and so-called "B-dot" probes that measure the time derivative of the magnetic field components, $\partial \mathbf{B}/\partial t = \dot{\mathbf{B}}$, to determine the structure of time-dependent magnetic fields; often these probes are nearly as large as the filament and easily perturb the experiment so we rarely use them except where necessary to qualitatively analyze the experiment.

2.2 Pressure Filament Overview

2.2.1 Single Filament

Once the injected beam thermalizes less than 1 m from the cathode source, in the axial direction, the heated region follows classical diffusion to form a long filamentary structure with a peaked symmetric profile in temperature and density, and a symmetric well in space potential. The T_e, n, and V_s transverse profiles collected using temporal sweeps are shown in Fig. 2.9 for a 15 V discharge bias at $t = 1.5$ ms and $z = 256$ cm. These planes have a dual spatial scale, one in physical units and the other normalized to the electron skin depth, δ_e. Previous experiments were critical in establishing the basic evolution of the plasma after the beam injection and provide a benchmark to compare with current and future experiments. Two clear discrepancies are the peaked density profile and a potential well observed in our experiments but not

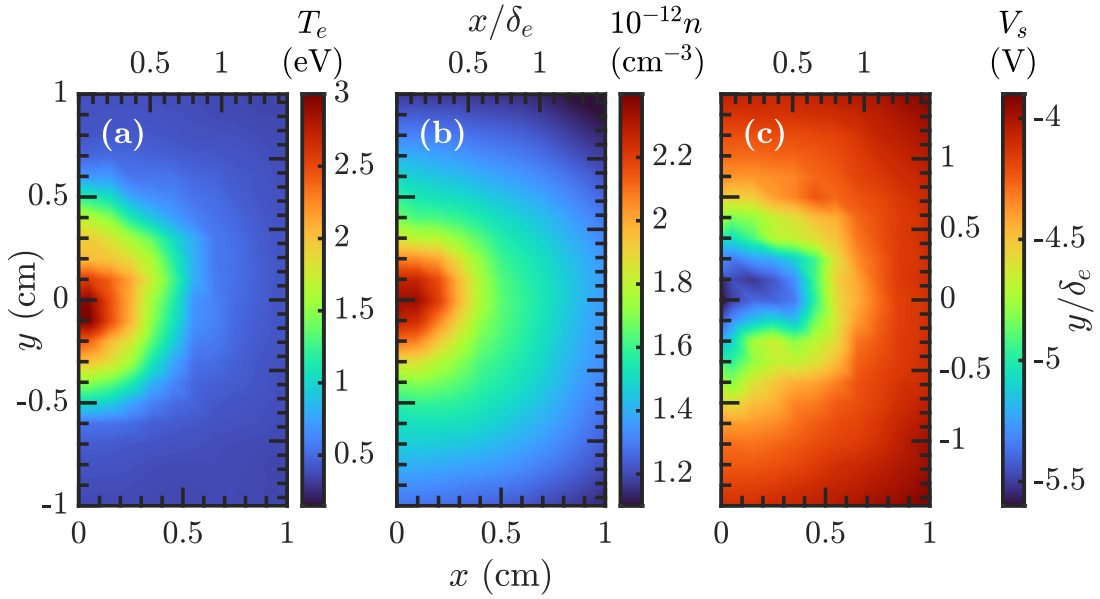

Figure 2.9: (a) Temperature, (b) density, and (c) space potential transverse planes at $z = 256$ cm for a 15 V discharge bias at time $t = 1.5$ ms. The top and right axes are normalized to the electron skin depth.

in previous experiments [14, 16, 19]. Past experiments relied on the assumption that density increases would only result from beam energies above the ionization energy of He and not from transport processes. The current results are supported by similar (and more recent) transport experiments with a ring-shaped LaB_6 (similar to CeB_6) source [70] that reported increases in density with beam electrons below the ionization energy of He. The most plausible explanation is the density transport is related to opposing axial flows from the axial pressure gradient of the pressure filament and the background plasma streaming at the sound speed to the ends of the device [70]; this description is supported qualitatively by numerical transport simulations [71]. The space potential is now clearly understood to be a result of the emissive CeB_6 cathode in the plasma and can be accurately modelled [72]; this model is used to predict the potential profile in a multi-filament configuration in Sec. 5.1.

The evolution of plasma parameters for a transverse line at $x = 0$ cm and $z = 256$ cm are shown in Fig 2.10 for a 15 V discharge, the same as in Fig. 2.9. In addition to the absolute values on the left axis of Fig 2.10, the normalized parameters are shown on the right with space normalized to the ion sound length before beam injection, ρ_{s0}, time normalized to the ion cyclotron frequency, Ω_i, electron plasma pressure to magnetic pressure, $\beta = P/P_{mag}$, and temperature and density normalized to values before the CeB_6 discharge, T_{e0} and n_0, respectively. Before beam injection at $t = -0.5$ ms the electron temperature, density, and space potential are all nearly uniform. Once the beam is injected, T_e rapidly reaches a stable temperature profile at $t = 1.5$ ms, with a peak temperature ~ 3 eV [Fig. 2.10(a)]. The temperature has a steep transverse profile < 1 cm in radius that changes little throughout the discharge at this power level. At lower discharge power the profile builds up more slowly, obeying classical transport to a peak temperature before transitioning to an anomalous cross-field transport regime [15, 16]; this slower evolution also occurs for

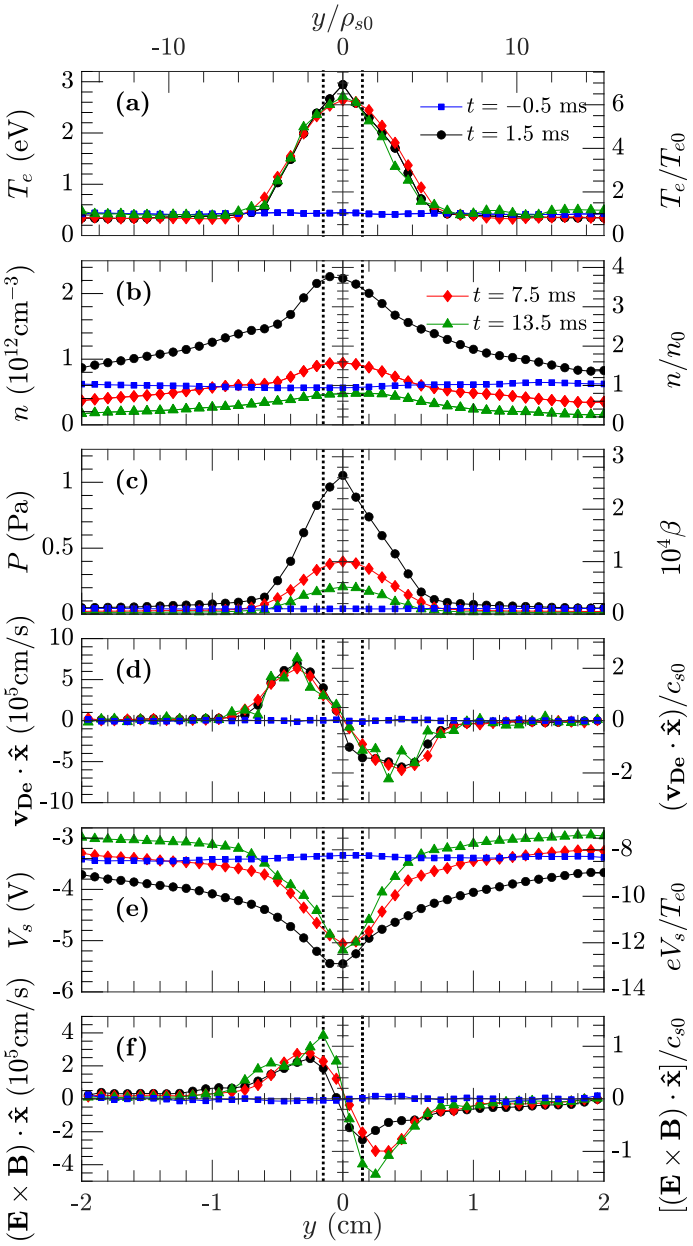

Figure 2.10: (a) Temperature, (b) density, (c) pressure, (d) diamagnetic drift, (e) space potential, and (f) $\mathbf{E} \times \mathbf{B}$ drift profiles for a 15 V discharge bias at times $t = -0.5$ ms (blue squares), $t = 1.5$ ms (black circles), $t = 7.5$ ms (red diamonds). The left axis indicates absolute values and the right axis is in normalized form. The scale factors T_{e0}, n_0, c_{s0} and ρ_{s0} correspond to the temperature, density, ion sound speed, and ion sound length calculated using average values prior to biasing of the CeB_6 crystal cathode at $t = -0.5$ ms.

axial planes further down the device.

The density experiences a rapid increase to peak densities over 2×10^{12} cm^{-3}. The transverse scale of the density increase is much larger than for the temperature and exceeds a 2 cm radius. The exponential decay of the density is still observed and results in a flattening of the density profile as time progresses (red and green curves, Fig. 2.10(b)). The exponential decay of the density causes a net decrease in the pressure of the filament throughout the shot (Fig. 2.10(c)) and a substantial change in the pressure gradient but does not affect the diamagnetic drift profile (Fig. 2.10(d)). At lower beam powers, the density increase is still rapid but has a lower peak value.

The potential well, like the density, has a larger radial extent than the temperature. Initially, the well ($t = 1.5$ ms) extends beyond a 2 cm radius but over time it steepens in the centre and becomes more shallow on the edges beyond 1 cm. The static radial electric field associated with the potential creates sheared $\mathbf{E} \times \mathbf{B}$ flows with peak velocity on the order of the ion sound speed, $c_{s0} = \rho_{so}\Omega_i$.

Fig. 2.11(a) shows ion saturation current fluctuations for two radial positions at $z = 256$ cm for a 15 V discharge. The corresponding power spectrum for the highlighted regions of the fluctuations are provided in Fig. 2.11(b). Two distinct wave modes develop during the filament evolution, drift-Alfvén waves (DW) and thermal waves (TW). The TWs have been previously proposed as a spontaneous mode that meets a quarter-wave resonance condition for the axial length of the filament [18], with frequencies in the range of $f_{TW} = 5$–10 kHz, shown clearly in the inset of Fig. 2.11(b). The TW resonance is confined to a 0.3 cm radius in the centre of the filament with an $m = 0$ azimuthal mode structure, visualized in Fig. 2.12(a) using the cross-correlation of the transverse plane probe with a fixed reference probe located at an axial position further from the source.

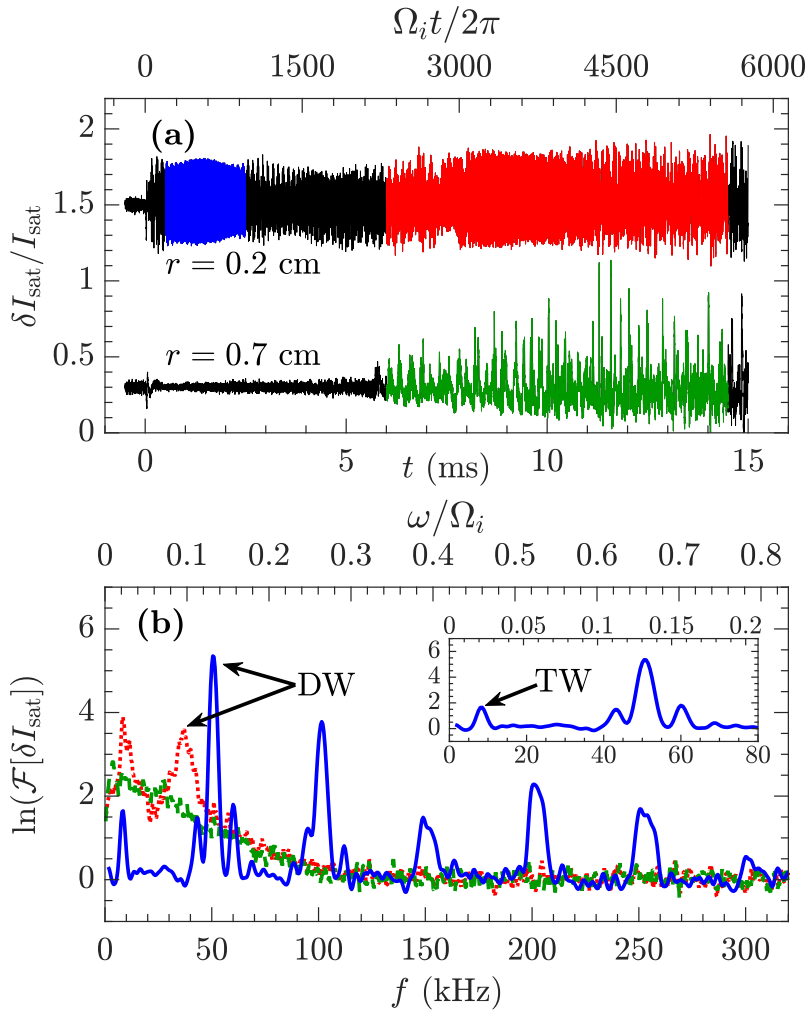

Figure 2.11: (a) Ion saturation current fluctuations greater than 1 kHz near the center and edge of the plasma pressure filament. The fluctuations are normalized to the long time average of the ion saturation current, the dc offset is arbitrary. (b) Power spectrum of the highlighted regions in (a), the inset is a reduced frequency scale to highlight the low frequency thermal resonance in the centre of the filament. The power spectra of background fluctuations (no filament) are removed.

As the temperature and density profiles steepen they become unstable to drift-Alfvén wave modes [17], a hybrid mode that results from a coupling of Alfvén modes and drift modes through the temperature and density gradients [21]. The frequencies

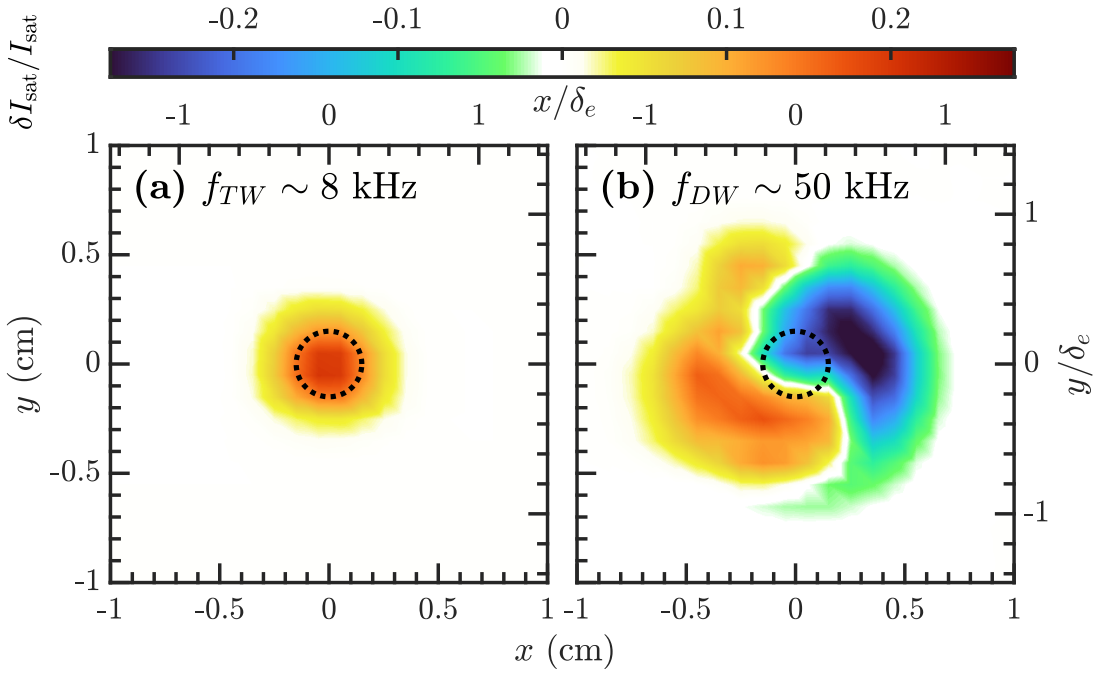

Figure 2.12: Transverse planes of the cross-correlation between the moving probe and a reference probe. (a) Thermal wave at $f_{TW} = 8$ kHz (b) Drift-Alfvén wave at $f_{DW} = 50$ kHz. The black circles indicates the size of the CeB_6 crystal cathode.

are in the range of $f_{DW} = 25$–50 kHz ($0.065\Omega_i$–$0.130\Omega_i$) and can be accurately modelled using the radial density and temperature profiles [21], and more recently with an inclusion of the potential profile [73] to include $\mathbf{E} \times \mathbf{B}$ flows. The most unstable mode in Fig. 2.12(b) has azimuthal mode number $m = 1$. The large amplitude of the drift waves results in non-linear effects such as wave-steepening, visible in the form of harmonic generation in Fig. 2.11(b). The sidebands on the fundamental drift wave corresponding to $f_{SB} = f_{DW} \pm f_{TW}$ are evidence of mode coupling between the TW and DW; this interaction remains unexplored in theory and modelling and is an opportunity for future study.

The DW growth eventually leads to a turbulent state (beyond 6 ms in Fig. 2.11(a)) characterized by intermittent transport (green and red regions). The intermittent fluctuations have been identified as Lorentzian shaped pulses [19, 20] that produce the

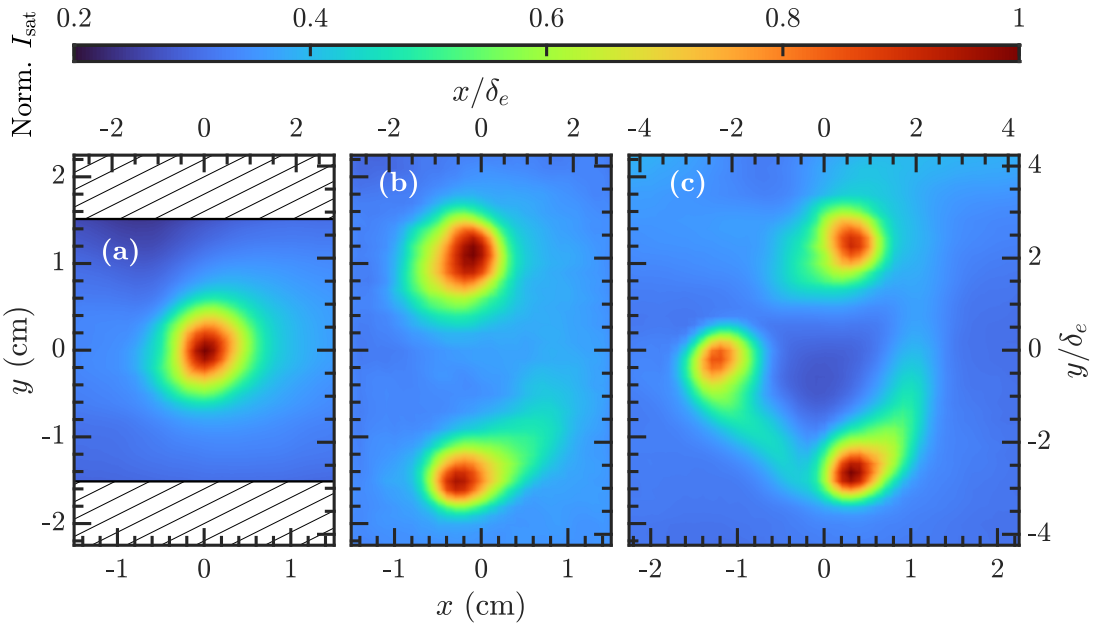

Figure 2.13: Different filament configurations investigated; (a) single filament, (b) assymmetric two filament configuration, (c) quasi-symmetric three filament configuration. For the two and three filament configurations several inter-filament separation distances have been investigated. I_{sat} is normalized to the maximum in each frame.

characteristic exponential frequency spectrum in Fig. 2.11(b) (red and green curves). The temporal Lorentzian pulses and exponential frequency spectra have been linked to chaotic dynamics [22] and are a ubiquitous feature in the edges of magnetized plasma devices where steep gradients occur [63]. This section concludes with a note that all analysis of the non-driven filament has been previously performed in the references provided and can be compared with the current replication of these results. The reproduction of past results is a critical step in moving forward with investigations into modulating a single source and introducing multiple heat sources.

2.2.2 Multi-Filament Configurations

The ability to independently control the location and strength of heat sources from the crystal cathodes, described in Section 2.1.2, has allowed us to investigate several different filament configurations. After characterizing a single source, we have studied

the interaction with a second source of equal strength and with a third source placed in such a way that a triangular pattern is created. An I_{sat} plane, located at axial position $z = 256$ cm, for each of these cases is shown in Fig. 2.13. It is interesting to note that for filaments of ∼1 cm width ($\sim 2\delta_e$) there is noticeable interaction at separations of ∼3 cm ($\sim 5\delta_e$), or greater than twice the filament widths, in both the two and three filament arrangements. This interaction is characterized by the formation of tail-like structures extending from each filament in Figs. 2.13(b) and (c) driven by $\mathbf{E} \times \mathbf{B}$ flows and asymmetric drift wave modes that then develop on the tails [73]. In Chapter 5 we will discuss the configuration in Fig. 2.13(c) further but the main focus will be on a tight tri-filament bundle where the distance of the cathodes from a central origin is adjusted to be ∼5 mm ($1\delta_e$) or in terms of inter-filament separation, approximately 0.85 cm ($1.6\delta_e$).

To provide an overview of the multi-filament experiments we compare the global profiles of electron temperature, density and space potential for the case of a single filament and the three filaments in close proximity. In the first case, we take an azimuthal average at different radial positions from the center of the single filament and in the latter case, we take an azimuthal average from the center of the triangular pattern. It is demonstrated in Section 5.1 that the azimuthal average of the filament bundle is a good approximation due to the quasi-symmetry of the tight configuration [73]. The comparison of the profiles for the two cases is shown in Fig. 2.14. The electron temperature and space potential of the multi-filament configuration in Fig. 2.14(b) are broadened as expected with the temperature peaking off-axis and exhibiting a gradient reversal within the core region. In both cases the observed well in the space potential of the plasma and associated radial electric field gives rise to sheared $\mathbf{E} \times \mathbf{B}$ flows in the azimuthal direction; as previously mentioned, the potential profiles are a result of the introduction of the CeB_6 crystals to the plasma. An

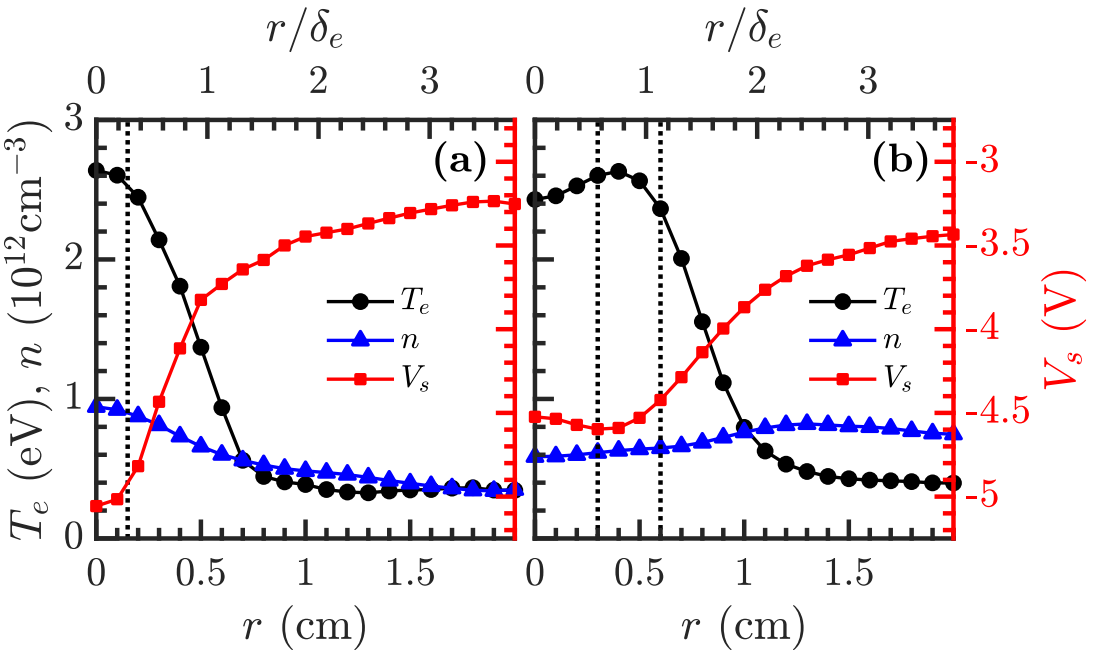

Figure 2.14: Comparison of plasma parameters between (a) the single filament and (b) the three filament azimuthal average. Electron temperature, T_e, is shown by black circles; the density, n, by blue triangles; and space potential, V_s, by red squares. The dotted black lines indicate the radial location of the CeB_6 crystal(s).

interesting feature is the reversal of the density gradient in the tri-filament configuration, which peaks outside the higher temperature region of the bundle as compared with the single filament density that peaks near the center. In both cases the density is relatively flat, indicating it is the electron temperature gradient that is the dominant free energy source for the development of drift wave instabilities investigated in Sec. 5.1 that are the main source of turbulent fluctuations studied in Sec. 5.2.

CHAPTER 3.

Thermal Wave Modelling

We begin in Section 3.1 with a description of the heat equation and the defining thermal wave equation that is the basis of both models. Next, we derive the homogeneous model using a Green function approach in Section 3.2. In Section 3.3 we solve the inhomogeneous problem using a Hamilton-Jacobi approach from the perspective of a thermal harmonic oscillator.

3.1 The Heat Equation

The starting point for modelling thermal waves is the heat equation for a magnetized plasma; in relation to the experiment it is natural to work in cylindrical coordinates with the transverse plane as the polar coordinates ($x = r\cos\theta, y = r\sin\theta$). The equation of heat balance for the electron temperature is,

$$\nabla_{\parallel}(\kappa_{\parallel}\nabla_{\parallel}T_e) + \nabla_{\perp}(\kappa_{\perp}\nabla_{\perp}T_e) - \frac{3}{2}n\frac{\partial T_e}{\partial t} = -Q \tag{3.1}$$

where $T_e = T_e(\mathbf{r}, t)$ is the electron temperature [erg], and $Q = Q(\mathbf{r}, t)$ is an arbitrary thermal source volumetric density [$\mathrm{erg \cdot cm^{-3}s^{-1}}$]. The coefficients $(\kappa_{\parallel}, \kappa_{\perp})$ are the parallel and cross-field classical thermal conductivities [$\mathrm{cm^{-1}s^{-1}}$] given by [11],

$$\kappa_{\parallel} = \frac{3.16nT_e\tau_e}{m_e}, \qquad \kappa_{\perp} = \frac{1.47\kappa_{\parallel}}{\Omega_e^2\tau_e^2} \tag{3.2}$$

where m_e is the electron mass [g], Ω_e is the electron cyclotron frequency [rad/s], $\tau_e = (3.44 \times 10^5) T_e^{3/2}/n\Lambda$ (with T_e in eV) is the electron collision time [s], and Λ is the Coulomb logarithm [74]. The extent of anisotropy in the conductivities of Eq. (3.2) is related to T_e, n, and B_0 through the proportions $\kappa_\parallel \propto T_e^{5/2}$ and $\kappa_\perp \propto n^2 T_e^{-1/2} B_0^{-2}$. For typical experiment parameters $n = (0.1\text{–}1) \times 10^{12}\,\mathrm{cm}^{-3}$ and $T_e = 1\text{–}5\,\mathrm{eV}$ the anisotropy is on the order of $\kappa_\parallel/\kappa_\perp \sim 10^5\text{–}10^9$ and the heat transport is dominated by field-aligned heat conduction over cross-field.

Now defining the Fourier transform as,

$$\begin{aligned} \tilde{F}(\mathbf{r},\omega) &= \mathcal{F}[F(\mathbf{r},t)] = \int_{-\infty}^{\infty} F(\mathbf{r},t) e^{-i\omega t} dt \\ F(\mathbf{r},t) &= \mathcal{F}^{-1}[F(\mathbf{r},\omega)] = \frac{1}{2\pi} \int_{-\infty}^{\infty} \tilde{F}(\mathbf{r},\omega) e^{-i\omega t} d\omega \end{aligned} \tag{3.3}$$

and under the assumption that the transforms of the temperature and source exist the heat equation is transformed to the defining thermal wave equation [23],

$$\nabla_\parallel(\kappa_\parallel(\mathbf{r})\nabla_\parallel \tilde{T}_e(\mathbf{r},\omega)) + \nabla_\perp(\kappa_\perp(\mathbf{r})\nabla_\perp \tilde{T}_e(\mathbf{r},\omega)) - \frac{3}{2} i\omega n(\mathbf{r}) \tilde{T}_e(\mathbf{r},\omega) = -\tilde{Q}(\mathbf{r},\omega) \tag{3.4}$$

where $\tilde{T}_e(\mathbf{r},\omega)$ is defined as the thermal wave field. In arriving at Eq. (3.4) coupling to the plasma flow in the heat balance equation is neglected. No assumption has been made about the homogeneity of the temperature and density spatial profiles in response to a time-independent source term, and therefore the homogeneity of the thermal conductivities; however, the changes to the conductivities in response to oscillations in the temperature are neglected and the temperature dependence in Eq. (3.2) is only due to the time-independent profiles. In relation to the experiments, over short time scales (∼1 ms) the temperature and density can be approximated to be constant for the purpose of having time-independent conductivities.

3.2 Homogeneous – Green Function Approach

This section presents the derivation of thermal wave fields using Green Functions [23]. This method is useful for systems with homogeneous plasma conductivity, but is less useful for inhomogeneous problems. The advantage of this method is that once one has obtained the Green function solution for a given set of boundary conditions, the thermal wave field $\tilde{T}(\mathbf{r},\omega)$ can be easily obtained for arbitrary surface and volume source distributions. The conductivities are now assumed to be homogeneous in space and changes to the conductivity by thermal fluctuations are ignored; furthermore, the experiments presented in Chapter 4 reveal that the spontaneous thermal wave, as well as the driven thermal modes, pertain to $m = 0$ azimuthal mode numbers and we consider only these modes by assuming azimuthal symmetry. Under the assumption of homogeneous conductivities and azimuthal symmetry Eq. (3.4) becomes,

$$\frac{\partial^2}{\partial z^2}\tilde{T}_e - \frac{\kappa_\perp}{\kappa_\parallel}\frac{1}{r}\frac{\partial}{\partial r}\left(r\frac{\partial}{\partial r}\tilde{T}_e\right) - k_\parallel(\omega)^2\tilde{T}_e = -\frac{1}{\kappa_\parallel}\tilde{Q} \tag{3.5}$$

and $k_\parallel$ is defined as,

$$k_\parallel(\omega) = \sqrt{i\frac{3n\omega}{2\kappa_\parallel}} = (1+i)\sqrt{\frac{3n\omega}{4\kappa_\parallel}} = (1+i)\sqrt{\frac{\omega}{2\alpha_\parallel}} \tag{3.6}$$

and $\alpha_\parallel = (2/3)\chi_\parallel$, where $\chi_\parallel = \kappa_\parallel/n$ is the parallel thermal diffusivity [$\mathrm{cm^2 s^{-1}}$]. The physical interpretation of $k_\parallel(\omega)$ is that of a complex wave number with units [$\mathrm{cm^{-1}}$].

Eq. (3.5) can be solved using the Green function approach by solving the inhomogeneous heat equation for an impulsive ring source at r_0, z_0, and t_0,

$$\frac{\partial^2}{\partial z^2}G - \frac{\kappa_\perp}{\kappa_\parallel}\frac{1}{r}\frac{\partial}{\partial r}\left(r\frac{\partial}{\partial r}G\right) - k_\parallel(\omega)^2 G = -\frac{1}{2\pi\alpha_\parallel r}\delta(r-r_0)\delta(z-z_0)\delta(t-t_0) \quad (3.7)$$

$$\frac{\partial^2}{\partial z^2}\tilde{G} - \frac{\kappa_\perp}{\kappa_\parallel}\frac{1}{r}\frac{\partial}{\partial r}\left(r\frac{\partial}{\partial r}\tilde{G}\right) - k_\parallel(\omega)^2 \tilde{G} = -\frac{1}{2\pi\alpha_\parallel r}\delta(r-r_0)\delta(z-z_0) \quad (3.8)$$

where in Fourier transforming from (3.7) to (3.8) the Green function $\tilde{G}(\mathbf{r}|\mathbf{r_0},\omega,t_0)$ has been defined as,

$$\tilde{G}(\mathbf{r}|\mathbf{r_0},\omega,t_0) = \tilde{G}(\mathbf{r}|\mathbf{r_0},\omega)e^{i\omega t_0}$$

and only $\tilde{G}(\mathbf{r}|\mathbf{r_0},\omega)$ needs to be found as the common $e^{i\omega t_0}$ term may be removed (recall, $\mathcal{F}[\delta(t-t_0)] = e^{i\omega t_0}$). On solving for $\tilde{G}(\mathbf{r}|\mathbf{r_0},\omega)$ the general solution for $\tilde{T}_e(\mathbf{r},\omega)$ is [23],

$$\begin{aligned}\tilde{T}_e(\mathbf{r},\omega) = \frac{2}{3n}\iiint_{V_0}\tilde{Q}(\mathbf{r_0},\omega)\tilde{G}(\mathbf{r}|\mathbf{r_0},\omega)\,dV_0 \\ + \frac{2\kappa}{3n}\oint_{S_0}\left[\tilde{G}(\mathbf{r}|\mathbf{r_0},\omega)\nabla_0\tilde{T}_e(\mathbf{r_0},\omega) - \tilde{T}_e(\mathbf{r_0},\omega)\nabla_0\tilde{G}(\mathbf{r}|\mathbf{r_0},\omega)\right]dS_0 \quad (3.9)\end{aligned}$$

where the first integral is for sources at $\mathbf{r_0}$ inside the volume V_0 and the second integral is for temperature or heat flux prescribed on the surface S_0 bounding V_0.

Upon solving for $\tilde{T}_e$ the thermal wave field is commonly split into a magnitude $A(\mathbf{r},\omega) = |\tilde{T}_e|$ and phase $\varphi(\mathbf{r},\omega) = \angle\tilde{T}_e$ for each frequency component. Solutions to Eq. (3.5) for two geometries are now presented, in the interest of continuity we leave the derivations using the Green function approach to Appendix A.

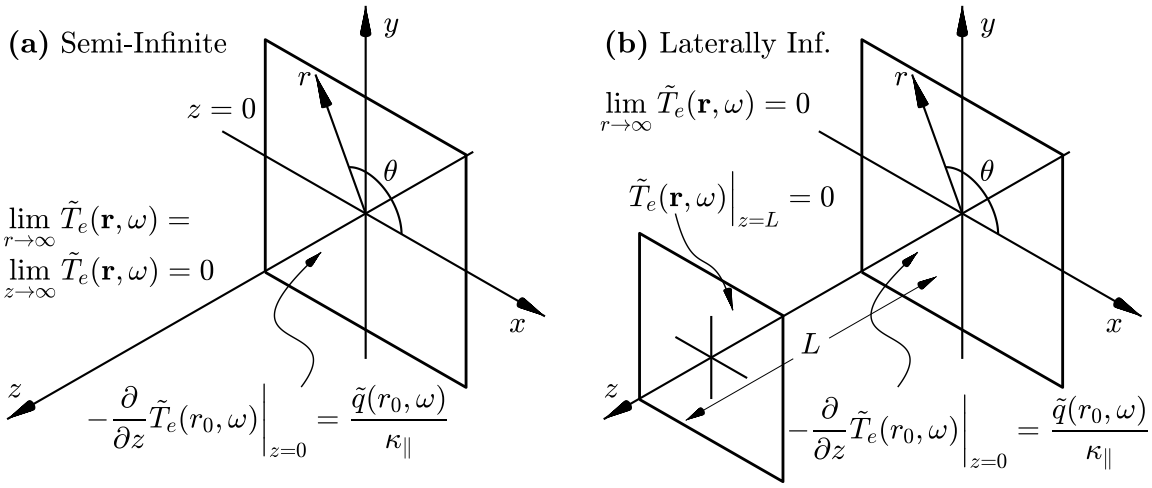

Figure 3.1: Geometry of the thermal wave models. (a) The semi-infinite case with only thermal flux prescribed at the surface $z = 0$ and (b) the bounded case with the same thermal flux at $z = 0$ and fixed field boundary at $z = L$.

3.2.1 Semi-Infinite Geometry

In this geometry the transverse plane is taken to be of infinite extent while a boundary is enforced at $z = 0$ limiting the parallel domain to $0 \leq z \leq \infty$. The solution $\tilde{T}_e(\mathbf{r}, \omega)$ must be bounded at ∞ requiring the conditions,

$$\lim_{r\to\infty} \tilde{T}_e(\mathbf{r}, \omega) = \lim_{z\to\infty} \tilde{T}_e(\mathbf{r}, \omega) = 0 \tag{3.10}$$

At the $z = 0$ boundary either a fixed field (Dirichlet) condition, fixed flux (Neumann) condition, or combination (third kind) condition can be prescribed – in relation to the experiment it is appropriate to choose an inhomogeneous Neumann condition to model the input of flux from the heat source created by the electron beam,

$$-\frac{\partial}{\partial z}\tilde{T}_e(r_0, \omega)\bigg|_{z=0} = \frac{\tilde{q}(r_0, \omega)}{\kappa_\parallel} \tag{3.11}$$

where $\tilde{q}(r_0, \omega) = \mathcal{F}[q(r_0, t)]$ is a thermal source flux density [erg $\cdot$ cm^{-2}s^{-1}] located on the plane $z = 0$ at source coordinate r_0 and directed into the enclosing volume. The geometry is depicted schematically in Fig. 3.1(a). The Green function solution for homogeneous boundary conditions in this geometry is given by,

$$\tilde{G}_{SI}(r, z|r_0; \omega) = \int_0^\infty \frac{J_0(\lambda r_0) J_0(\lambda r)}{2\pi\alpha_\parallel s} e^{-sz} \lambda \, d\lambda \tag{3.12}$$

where,

$$s = s(k_\parallel, \lambda) = \sqrt{k_\parallel(\omega)^2 + \frac{\kappa_\perp}{\kappa_\parallel}\lambda^2} \tag{3.13}$$

3.2.2 Laterally Infinite Geometry

The bounded geometry is taken to be a region of finite axial length L ($0 \leq z \leq L$) and infinite lateral extent with the same condition Eq. (3.11) at the $z = 0$ surface and a homogeneous Dirichlet condition on the boundary at $z = L$,

$$\tilde{T}_e(\mathbf{r}, \omega)\Big|_{z=L} = 0 \tag{3.14}$$

$$\tag{3.15}$$

This geometry with the two bounding planes is shown schematically in Fig. 3.1(b). The fixed field condition enforces a node at the boundary, which is expected if the filament does behave as a quarter wave resonator. The Green function solution for this geometry is,

$$\tilde{G}_{LI}(r, z|r_0; \omega) = \int_0^\infty \frac{J_0(\lambda r_0) J_0(\lambda r)}{2\pi\alpha_\parallel s(1 + e^{-2sL})} \times \left(e^{-sz} - e^{-s(2L-z)}\right) \lambda \, d\lambda \tag{3.16}$$

where the function s is again defined by Eq. (3.13). It can easily be verified that in the limit $L \to \infty$ Eq. (3.16) reduces to Eq. (3.12).

3.2.3 Thermal Wave Field

The solution for the the thermal wave field $\tilde{T}_e(\mathbf{r}, \omega)$ in Eq. (3.5) can be found using the Green functions for each geometry and Eq. (3.9) once the appropriate source conditions $\tilde{Q}(\mathbf{r_0}, \omega)$ and $\tilde{q}(r_0, \omega)$ are specified. To model the heat source in the experiment we assume no volume sources, thus the only source is the inhomogeneous heat flux boundary condition of Eq. (3.11). Under this specification Eq. (3.9) reduces to a single integral over the surface source coordinate r_0,

$$\tilde{T}_e(\mathbf{r}, \omega) = \frac{2\pi\alpha_\parallel}{\kappa_\parallel} \int_0^\infty \tilde{q}(r_0, \omega)\tilde{G}(r, z|r_0; \omega) r_0 \, dr_0 \tag{3.17}$$

To model the thermal flux source we choose $\tilde{q}(r_0, \omega)$ to be of the form,

$$\begin{aligned} \tilde{q}(r_0, \omega) &= \Pi_c(r_0)\frac{q_0}{2}(1 + e^{i\omega t}) \\ &= \frac{q_0}{2}(1 + e^{i\omega t}) \times \begin{cases} 1 & r_0 \leq a \\ 0 & r_0 > a \end{cases} \end{aligned} \tag{3.18}$$

where Π_c is the cylinder function, a is a constant [cm] defining the radius of the thermal flux source, and q_0 is a surface flux constant [$\mathrm{erg \cdot cm^{-2}s^{-1}}$]. The unity term in Eq. (3.18) will be ignored since we care only about the oscillating component; additionally, the $e^{i\omega t}$ term is generally omitted from the equation for the thermal wave field as the oscillating nature is implied and we continue that practice here. Substituting Eq. (3.18) into Eq. (3.17), using the appropriate Green function for each

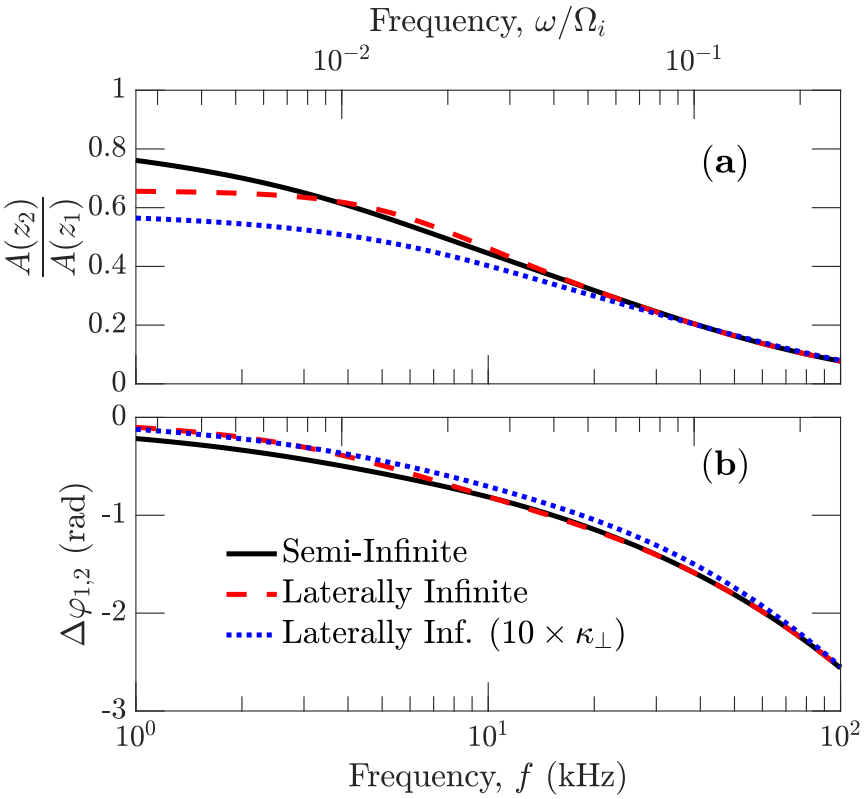

Figure 3.2: Comparison of the semi-infinite model (black solid), laterally infinite model (red dashed), and laterally infinite model with artificially increased cross-field conductivity (blue dotted). (a) Amplitude ratio. (b) Phase difference.

geometry, and simplifying the expressions the thermal wave fields are,

$$\tilde{T}_{eSI}(r,z|r_0;\omega) = \frac{q_0 a}{2\kappa_\parallel}\int_0^\infty \frac{J_0(\lambda r)J_1(\lambda a)}{s} e^{-sz}\, d\lambda \tag{3.19}$$

$$\tilde{T}_{eLI}(r,z|r_0;\omega) = \frac{q_0 a}{2\kappa_\parallel}\int_0^\infty \frac{J_0(\lambda r)J_1(\lambda a)}{s(1+e^{-2sL})}\left(e^{-sz} - e^{-s(2L-z)}\right)\, d\lambda \tag{3.20}$$

For experiments that sample the thermal wave field in the centre of the filament ($r = 0$) at two axial locations z_1 and z_2, the thermal wave field can be compared through their magnitude ratio $A(z_2)/A(z_1)$ and phase difference $\Delta\varphi_{1,2} = \varphi(z_2) - \varphi(z_1)$.

Fig. 3.2 displays the amplitude ratio and phase difference over an experimentally relevant frequency range between wave fields at $z_1 = 160$ cm and $z_2 = 256$ cm predicted by Eqs. (3.19) and (3.20) for a filament of length $L = 450$ cm, dc temperature $T_e = 3.5$ eV, density $n = 0.5 \times 10^{12}$ cm^{-3}, and source radius $a = 0.15$ cm. In both the phase and amplitude the semi-infinite (black solid) and laterally infinite (red dashed) models converge at high frequencies. This can be understood through the thermal wave diffusion length, $\mu_\parallel(\omega) = 1/\,\mathrm{Re}(k_\parallel(\omega))$, that decreases with increasing frequency. The reduced penetration of higher frequencies has the effect that the boundary at $z = L$ in the laterally infinite model is several diffusion lengths away and has little impact on the thermal wave field except in a region close to the boundary. Similar effects are observed if a zero-field boundary is imposed at a radius $R_0 \sim 1$ cm, but due to the anisotropy the effect is negligible in the center of the filament and unnecessarily complicates the model presented here.

At lower frequencies, thermal wave interference effects are observed in the laterally infinite model. The amplitude ratio saturates while the phase of the laterally infinite model leads the semi-infinite model; this result is due to quasi-reflections of thermal waves at the boundary, understood physically as depletion or accumulation of thermal wave power in the medium. The effects observed become more pronounced at higher frequencies for shorter filament lengths and thermal wave fields observed closer to the boundary. It is worth noting that Eq. (3.20) also predicts thermal resonances[27]; however, these resonances are only increases in amplitude *relative* to the thermal wave field of the semi-infinite model whereas the *absolute* amplitude of the thermal wave field still continuously decreases with frequency.

Included in Fig. 3.2 is the laterally infinite model with the anisotropy ratio $\kappa_\parallel/\kappa_\perp$ reduced by scaling the perpendicular component by a factor of 10. There is little change in the phase difference that is dominated by $\kappa_\parallel$, the precision required to detect

this change is well beyond the current experiment capabilities. However, the difference in the amplitude ratio between these two cases suggests that the spatial amplitude decay of thermal waves could be a useful tool for determining the anisotropy ratio independent of the equations for the thermal conductivities (Eq. (3.2)). Presently, the signal-to-noise ratio in the experiment is too poor to permit this measurement, but it is highlighted here as a potential use for thermal waves and to inform future experiments.

3.3 Inhomogeneous – Hamilton-Jacobi Approach

The homogeneous model works well as an approximation of the thermal wave field between two axial locations in the centre of the filament [75]. However, recent experimental data for the cross-field component of the thermal wave field suggests the inhomogeneous profiles play a larger role on the gradients, necessitating the need for a two-dimensional inhomogeneous model with anisotropic conductivities. While the Green function approach is a powerful technique for homogeneous media and is a common approach in the materials science community, it becomes a cumbersome method to apply to multi-dimensional inhomogeneous problems with anisotropic conductivities. For inhomogeneities in only one dimension, or one axis of a 2D or 3D problem, the Green function method can be employed by slicing the medium into many pieces and using the Green function in each domain [76]; if applying this to a two-dimensional problem the method quickly becomes unwieldy. In this section we investigate an approach based on classical mechanics, dubbed the Thermal Harmonic Oscillator [48, 49], that uses the Hamilton-Jacobi equation [77, 78] to solve for the thermal wave field with arbitrary conductivity and density profiles. We start with a description of a one-dimensional model and then discuss the route towards a two-dimensional model, which is still currently in development.

3.3.1 One-Dimensional Model

The one-dimensional model has been explored previously [48] and the objective here is to present a separate, more rigorous route to the Hamilton-Jacobi equation. This is to establish a methodology for approaching the two-dimensional inhomogeneous and anisotropic problem that is significantly more complex. We begin with Eq. (3.4) in one dimension with inhomogeneous parallel conductivity and density

profiles and no volume sources,

$$\frac{\partial}{\partial z}\left(\kappa_{\parallel}(z)\frac{\partial}{\partial z}\tilde{T}_e(z,\omega)\right) - \frac{3}{2}i\omega n(z)\tilde{T}_e(z,\omega) = 0 \tag{3.21}$$

Using Hamilton's principle in the variational form in the region $z = 0$ to $z = L$ where $L \leq \infty$,

$$\delta S = \int_0^L \left[\frac{\partial}{\partial z}\left(\kappa_{\parallel}(z)\frac{\partial}{\partial z}\tilde{T}_e(z,\omega)\right) - \frac{3}{2}i\omega n(z)\tilde{T}_e(z,\omega)\right]\delta\tilde{T}_e\, dx = 0 \tag{3.22}$$

and the properties of the variational derivative [77], the Lagrangian of the system is,

$$\mathcal{L} = \frac{1}{2}\kappa_{\parallel}(z)\frac{\partial^2\tilde{T}_e}{\partial z^2} + \frac{1}{2}i\omega\frac{3}{2}n(z)\tilde{T}_e^2 \tag{3.23}$$

The Hamiltonian can be found after the application of the Legendre transformation,

$$H = \tilde{p}_T\frac{\partial\tilde{T}_e}{\partial z} - \mathcal{L}, \qquad \tilde{p}_T = \frac{\partial L}{\partial(\partial\tilde{T}_e/\partial z)} = \kappa_{\parallel}(z)\frac{\partial\tilde{T}_e}{\partial z} \tag{3.24}$$

$$H = \frac{1}{2\kappa_{\parallel}(z)}\tilde{p}_T^2 - \frac{1}{2}i\omega\frac{3}{2}n(z)\tilde{T}_e^2 \tag{3.25}$$

The quantity $\tilde{p}_T$ is the generalized momentum and physically represents the heat flux, the field $\tilde{T}_e$ represents the generalized position often denoted q, z is the generalized time, and H is the generalized energy of the system. The Hamiltonian in Eq. (3.25) is an explicit function of z and makes any solution to $\tilde{T}_e$ difficult to find. To arrive at a generalized time-indepenent Hamiltonian (or space-independent) a canonical transformation is made, but must be done in *extended phase space* to allow for

transformations of the generalized time [79–84]. Extended phase space takes the form,

$$q_E = (\tilde{T}_e, z), \quad \text{Extended Positions} \tag{3.26}$$

$$p_E = (\tilde{p}_T, -\mathcal{H}), \quad \text{Extended Momenta} \tag{3.27}$$

where $\mathcal{H}$ is the instantaneous value of H. Rewriting the variational principle as,

$$\delta S = \delta \left\{ \int_0^L \left[\tilde{p}_T(z) \frac{\partial \tilde{T}_e(z)}{\partial z} - H(\tilde{T}_e(z), \tilde{p}_T(z), z) \right] \, dx \right\} = 0 \tag{3.28}$$

and then parametrizing z with respect to a new variable s gives,

$$\delta S = \delta \left\{ \int_0^L \left[\tilde{p}_T(s) \frac{d\tilde{T}_e(s)}{ds} - H(\tilde{T}_e(z), \tilde{p}_T(z), z) \frac{dx}{ds} \right] \, ds \right\} = 0 \tag{3.29}$$

Eq. (3.29) is the variational principle in extended phase space, whereupon defining the extended Hamiltonian as,

$$H_E(\tilde{T}_e, z, \tilde{p}_T, \mathcal{H}) = H(\tilde{T}_e, z, \tilde{p}_T) - \mathcal{H} \tag{3.30}$$

the equation takes on the familiar form of the variational principle,

$$\delta S = \delta \left\{ \int_0^L \left[\sum_j p_{E_j} \frac{dq_{E_j}}{ds} - H_E \right] \, ds \right\} = 0 \tag{3.31}$$

the subscript j represents the components of the extended phase space. In extended phase space there are equivalent extended canonical equations given by,

$$\frac{dq_{E_j}}{ds} = \frac{\partial H_E}{\partial p_{E_j}}, \quad \frac{dp_{E_j}}{ds} = -\frac{\partial H_E}{\partial q_{E_j}} \tag{3.32}$$

Since H_E is independent of s, its total derivative with respect to s is zero,

$$\frac{dH_E}{ds} = \sum_j \left(\frac{\partial H_E}{\partial q_{E_j}} \frac{dq_{E_j}}{ds} + \frac{\partial H_E}{\partial p_{E_j}} \frac{dp_{E_j}}{ds} \right) = 0 \tag{3.33}$$

Thus, the extended Hamiltonian is an invariant in extended phase space. Now, a canonical transformation is made in extended phase space to produce a time-invariant (i.e. z-invariant) Hamiltonian in the *ordinary* phase space. The transformation takes the form,

$$\tilde{T}_e \to \tau, \quad \tilde{p}_T \to p_\tau, \quad z \to \zeta, \quad H \to K \tag{3.34}$$

where the transformed coordinates and momenta satisfy Eqs. (3.31) and (3.32). The integrands of Eq. (3.31) in the original and transformed system can only differ by a total differential, dF_1/ds, and yield the relation,

$$\tilde{p}_T \, d\tilde{T}_e - H \, dz = p_\tau \, d\tau - K \, d\zeta + dF_1 \tag{3.35}$$

where $F_1 = F_1(\tilde{T}_e, \tau, z, \zeta)$ is the generating function of the desired transformations. The generating function may be chosen to depend on any pair of old or new positions and momenta using a Legendre transformation. For the problem at hand, a generating function of the form,

$$F_2(\tilde{T}_e, p_\tau, z, K) = F_1(\tilde{T}_e, \tau, z, \zeta) + \tau p_\tau - \zeta K \tag{3.36}$$

is desired and gives the following relationships for the canonical transform,

$$\tau = \frac{\partial F_2}{\partial p_\tau}, \quad \tilde{p}_T = \frac{\partial F_2}{\partial \tilde{T}_e}, \quad \zeta = -\frac{\partial F_2}{\partial K}, \quad H = -\frac{\partial F_2}{\partial z} \tag{3.37}$$

We have found a suitable generating function for producing a time-independent Hamiltonian,

$$F_2 = \left(\frac{3}{2}n(z)\kappa_\parallel(z)\right)^{1/4}\tilde{T}_e p_\tau - Km\int_0^z \left(\frac{3n(w)}{2\kappa_\parallel(w)}\right)^{1/2} dw \tag{3.38}$$

that yields the transformation,

$$\tau = \left(\frac{3}{2}n(z)\kappa_\parallel(z)\right)^{1/4}\tilde{T}_e \tag{3.39}$$

$$p_\tau = \frac{1}{\left(\frac{3}{2}n(z)\kappa_\parallel(z)\right)^{1/4}}\tilde{p}_T \tag{3.40}$$

$$\zeta = m\int_0^z \left(\frac{3n(w)}{2\kappa_\parallel(w)}\right)^{1/2} dw \tag{3.41}$$

$$K = \frac{1}{2m}p_\tau^2 + \frac{1}{2}k\tau^2 \tag{3.42}$$

where,

$$m^{-1} = \frac{1}{L}\int_0^L \left(\frac{3n(w)}{2\kappa_\parallel(w)}\right)^{1/2} dw \tag{3.43}$$

$$k = -i\frac{\omega}{m} \tag{3.44}$$

The only assumption in deriving the transformation is $de_\parallel(z)/dz \ll e_\parallel(z)$ where $e_\parallel(z) = \sqrt{\frac{3}{2}n(z)\kappa_\parallel(z)}$ is the thermal effusivity. The Hamiltonian in Eq. (3.42) is in the form of a *Thermal Harmonic Oscillator* (THO) with an effective mass m and spring constant k. the Hamiltonian K is a constant of the motion in the transformed phase space [48].

In the previous work on the harmonic oscillator approach to diffusion waves [32, 48, 49, 85] the generalized momentum transformation is incorrectly found to be $p_\tau = \tilde{p}_T$, perhaps because the extended phase space approach presented here was not used; this

has no effect on the final result for $\tilde{T}_e$ as the correct position transformation was used but it creates inconsistencies in the intermediate steps to solving for $\tilde{T}_e$. Notably, p_τ in our solution correctly yields the relationship $p_\tau = m\dfrac{\partial\tau}{\partial\zeta}$ (i.e. $\mathbf{p} = m\mathbf{v}$ in classical mechanics).

To solve for τ, the transformed thermal wave field, the Hamilton-Jacobi equation is used,

$$\frac{\partial S}{\partial \zeta} + K(\tau, \frac{\partial S}{\partial \tau}, \zeta) = 0 \tag{3.45}$$

where the momentum is replaced by the relation $p_\tau = \partial S/\partial\tau$ [78]. The Hamilton-Jacobi equation amounts to another canonical transformation to make all of the coordinates cyclic by transforming to a new Hamiltonian that is identically zero; the generating function of this transformation is just the action (Hamilton's Principal Function) S. The new stationary coordinates are generally found in terms of the initial conditions τ_0 and p_{τ_0}, in this case the values on the boundary $\zeta = 0$ ($z = 0$ in the original phase space). Since the generalized time ζ is already cyclic the method of separation of variables is used to solve the Hamilton-Jacobi equation,

$$S(\tau, \zeta, \mathcal{K}) = W(\tau, \mathcal{K}) - \mathcal{K}\zeta \tag{3.46}$$

where W is the abbreviated action (Hamilton's Characteristic Function). This has the well-known solution [78],

$$\tau(\zeta) = \sqrt{\frac{2\mathcal{K}}{m\Omega^2}}\sin(\Omega\zeta + \beta) \tag{3.47}$$

$$p_\tau(\zeta) = \sqrt{2m\mathcal{K}}\cos(\Omega\zeta + \beta) \tag{3.48}$$

where

$$\Omega \equiv \frac{k}{m} = \frac{i \exp[\frac{i\pi}{4}]\sqrt{\omega}}{m} \tag{3.49}$$

is the frequency of the THO and the generalized momentum $\mathcal{K}$ and generalized position β of the Hamilton-Jacobi transformation are equivalent to the initial energy and angle of the oscillator and are dependent on the initial (boundary) conditions according to,

$$\mathcal{K} = \frac{1}{2m} p_{\tau_0}^2 + \frac{1}{2} k \tau_0^2 \tag{3.50}$$

$$\beta = \tan^{-1}\left(m\Omega \frac{\tau_0}{p_{\tau_0}} \right) \tag{3.51}$$

If the energy is assumed to be split evenly between the kinetic and potential energy terms at the surface $z = 0$ (i.e. $\beta = \pi/4$)[85] the conditions are uniquely defined by one boundary condition, namely the one-dimensional equivalent of the flux condition Eq. (3.18) used in the Green function approach, in the transformed momentum this is,

$$p_{\tau_0} = -\frac{q_0}{2\sqrt{e(0)}}(1 + e^{i\omega t}) \tag{3.52}$$

Inverting the transformation for $\tilde{T}_e(z, \omega)$ yields,

$$\tilde{T}_{e_{in}} = \frac{1}{2\sqrt{e(z)}} \left\{ \left(\frac{p_{\tau_0} e^{i\pi/4}}{\sqrt{w}} + \tau_0 \right) \exp[f(z)] - \left(\frac{p_{\tau_0} e^{i\pi/4}}{\sqrt{w}} - \tau_0 \right) \exp[-f(z)] \right\} \tag{3.53}$$

where the subscript *in* indicates this is the thermal wave field for the inhomogeneous profiles and the function $f(z)$ follows from the definition of the time transformation

and frequency of the harmonic oscillator, $\Omega^2 = k/m$, and the term $\Omega\zeta$,

$$f(z) = \int_0^z (1+i)\left(\frac{3n(w)\omega}{4\kappa_\parallel(w)}\right)^{1/2} dw = \int_0^z k_\parallel(w)dw \tag{3.54}$$

and $k_\parallel(z)$ is the inhomogeneous thermal wave number. Eq. (3.53) can be used for any arbitrary inhomogeneous profiles. This exercise demonstrates the solution method that can be applied in the two-dimensional case and has been completed previously by others [48, 49, 85]. An exact analytic solution can be found for the exponential profile [85],

$$\alpha_\parallel(z) = \alpha_{\parallel_0}\left(\frac{1+\Delta e^{-\lambda z}}{1+\Delta}\right)^{1/2}, \quad \Delta = \sqrt{\frac{\alpha_{\parallel_0}}{\alpha_{\parallel_\infty}}} - 1 \tag{3.55}$$

where λ is a decay constant of the profile, and $\alpha_\parallel = 3/2\chi_\parallel$ where $\chi_\parallel$ is the thermal diffusivity $\kappa_\parallel/n$. This solution is not reproduced herein but is used to model the experimental data along a field line in the radial experiments of Section 4.2 for experimentally realistic parameters. An example is shown in Fig. 3.3 and demonstrates that the model can accurately describe the interference effects that will be presented later. The success of the simple one-dimensional exponential model in predicting the observed phase and amplitude from the experiment motivates the application to a two-dimensional model with anisotropic and inhomogeneous conductivities, which is not trivial. The needed extension to two-dimensions is what prompted us to investigate how to come up with the generating function for the transformation to the z-invariant Hamiltonian so the same method could be applied to more dimensions, in the previous work on the THO either no generating function was used or it is not communicated how the transformations were obtained.

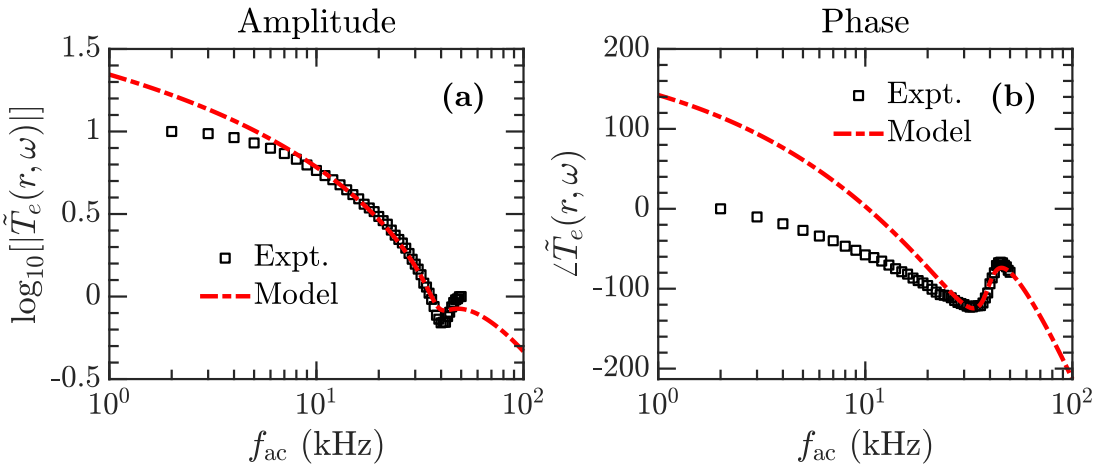

Figure 3.3: Comparison of the exponential inhomogeneous model (red solid) and the experimental wave field at $r = 1.5$ cm and $z = 190$ cm (black squares). (a) Amplitude (b) Phase

3.3.2 Two-Dimensional Model

When moving to two dimensions the theory moves from point mechanics to a field mechanics since there is a thermal field flux associated with each spatial coordinate. Further complicating the issue is the special role that time still plays in classical field theory. In the one dimensional case generalized time was easily treated as the single spatial coordinate, and the generalized position as the temperature field; in more dimensions, one of the spatial coordinates will receive preferential treatment as the generalized time. In formulating the multi-dimensional problem it will be useful to introduce the 4-momenta as done by de Donder [86] and Weyl [87] (sometimes called Covariant Hamiltonian Field Theory) that treats the space and time coordinates on equal footing. To demonstrate the differences in these approaches it is useful to examine the Hamiltonian in each formulation,

$$H_{PM} = \sum_{\alpha} p_\alpha \dot{x}_\alpha - \mathcal{L}_{PM}(x_\alpha, \dot{x}_\alpha, t), \quad p_\alpha = \frac{\partial \mathcal{L}_{PM}}{\partial \dot{x}_\alpha}, \quad \alpha = 1,2,3|(x,y,z) \tag{3.56}$$

$$H_{FM} = p_t\dot{\phi} - \mathcal{L}_{FM}(\phi, \dot{\phi}, \nabla_\alpha\phi, x_\alpha, t), \quad p_t = \frac{\partial \mathcal{L}_{FM}}{\partial \dot{\phi}}, \quad \alpha = 1, 2, 3|(x, y, z) \tag{3.57}$$

$$H_{DW} = \sum_\alpha p_\alpha \frac{\partial \phi}{\partial x_\alpha} - \mathcal{L}_{DW}(\phi, \frac{\partial \phi}{\partial x_\alpha}, x_\alpha), \quad p_\alpha = \frac{\partial \mathcal{L}_{DW}}{\partial \left(\frac{\partial \phi}{\partial x_\alpha}\right)}, \quad \alpha = 0, 1, 2, 3|(t, x, y, z) \tag{3.58}$$

While the extension of $\mathcal{L}_{FM}$ to $\mathcal{L}_{DW}$ appears trivial, the de Donder and Weyl Hamiltonian allows for a momentum associated with each of the field derivatives, not just the temporal momentum. This allows for each spatial coordinate of the inhomogeneous problem to be treated equally in the canonical transformation. There exists an equivalent DW extended phase space transformation [88, 89] where, in analogy to extended point mechanics treating generalized time and coordinates the same, the generalized field and coordinates are all treated the same. This allows for a transformation to an invariant extended de Donder and Weyl Hamiltonian with a suitable generating function. To solve the multi-dimensional THO there is the de Donder and Weyl Hamilton-Jacobi equation (DWHJ) [90],

$$\frac{\partial S_\alpha}{\partial x_\alpha} + H_{DW}\left(\phi, \frac{\partial S_\alpha}{\partial \phi}\right) = 0 \tag{3.59}$$

where the principal functions S_α for each dimension can each be separated as in the one-dimensional problem since H_{DW} is independent of the x_α as they will each be cyclic once the generating function is found. Solving the DWHJ equation will yield $\tilde{T}_e(r, z, \omega)$ for inhomogeneous and anisotropic conductivities, i.e. the equivalent of Eq. (3.4). The parallels to the one-dimensional case are obvious. The canonical transformation in an extended de Donder and Weyl is not trivial, this represents an ongoing piece of this project and the current progress will be left out of this thesis.

CHAPTER 4.

Thermal Wave Experiments

The inspiration for our thermal wave experiments stems from Ångström's work in 1862, "Neue Methode, das Wärmeleitungsvermögen der Körper zu bestimmen" ("New Method to determine the Thermal Conductivity of a Body") [24] in an experiment now often known as "Angstrom's Method" [91]. The experiment consists of a metal bar with a heat source at one end and several thermometers spaced along the length of the bar. The bar is then alternately heated and cooled at one end and the temporal response of the thermometers is recorded. Using the phase shift of the oscillating temperature at each location the thermal conductivity of the metal can be determined. The first set of experiments presented in Section 4.1 use this methodology to verify the excitation of thermal waves and measure the parallel thermal diffusivity of the plasma. The plasma column is analogous to the metal bar, and probes inserted at two axial locations can measure the phase shift of the thermal wave field. In Section 4.2 the measurement technique is improved and a detailed analysis of the cross-field structure of the thermal wave field in various transport regimes is presented. The inhomogeneous model discussed in Section 3.3 is used to describe the features of the cross-field structure.

4.1 Axial Experiments

The experiment setup for this series of experiments is identical to that displayed in Fig. 2.2(a). In these experiments there is only a single filament source and Langmuir

probes are inserted at port locations $z_1 = 160$ cm, $z_2 = 256$ cm, and $z_3 = 640$ cm, as measured from the crystal cathode. There is a voltage sensor measuring the bias between the crystal cathode and mesh anode, and Rogowski coils measure the electron current to the crystal cathode and from the anode.

4.1.1 Beam Oscillations

This section describes the results of applying an oscillating voltage to the cathode. Fig. 4.1(a) displays the 100 shot averages of voltage and current for a 20 ms discharge. The applied dc voltage, $V_{\rm dc}$, is 12.5 V and the 7 kHz sinusoidal pulses have a duration of 1 ms, are spaced 1 ms apart, and have an amplitude of $V_{\rm ac} \sim 2.5$ V. The current has a linear response to the applied voltage pulses but the impedance is not purely resistive. Figs. 4.1(b) and 4.1(c) indicate the magnitude and phase response, respectively, of the current for each applied pulse over a range of driver frequencies, $f_{\rm ac} = 2$–64 kHz. Both the fluctuating voltage and current are normalized to their respective dc levels, where the voltage amplitude remains fixed for every pulse at $\delta V/V \sim 20\%$. The phase reference is the voltage and a positive phase shift indicates a leading current. The current response is both frequency-dependent and time-dependent. There is an amplitude resonance at 23 kHz, with a corresponding inflection point in the phase, that increases in quality as the time of pulse application delays. Fig. 4.1 indicates that injected power of the ac modulation is not consistent over the frequency range investigated; when analyzing the response of plasma parameters only a relative amplitude and phase should be compared across different frequencies. The consistent frequency of the amplitude resonance indicates the response is not related to the drift-Alfvén wave, which can have a similar frequency but changes throughout the shot. It can be speculated that the parameter most likely responsible for the temporal changes of the amplitude and phase is the plasma density

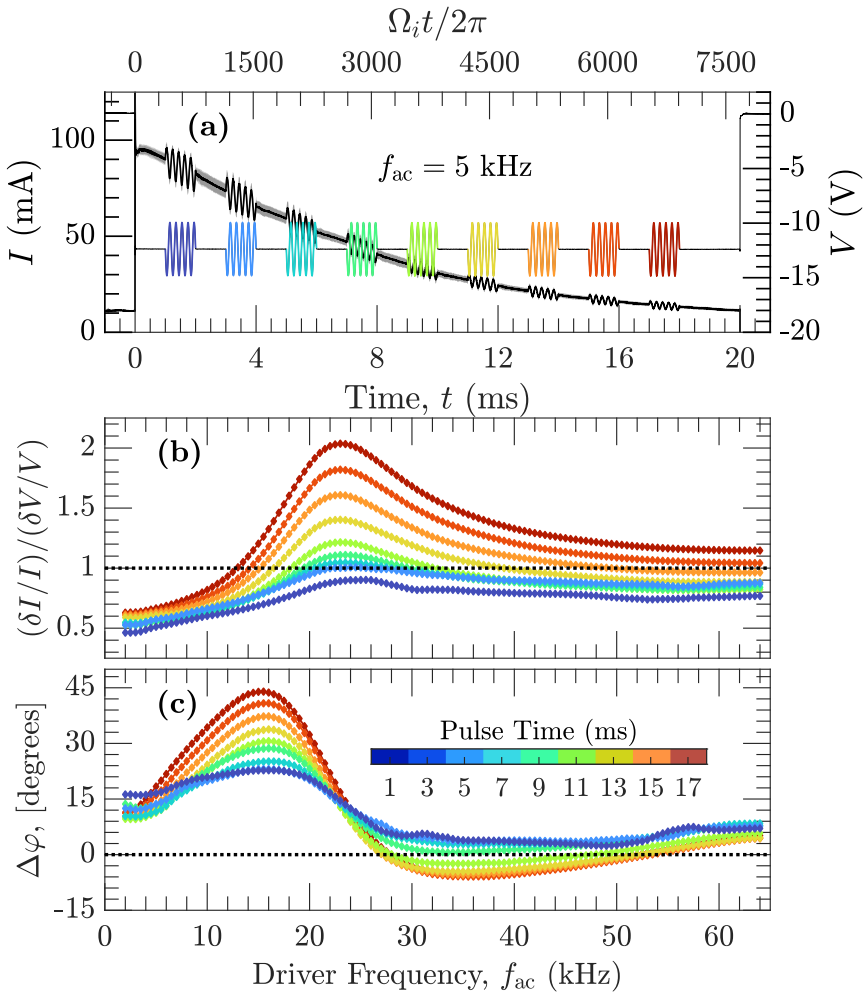

Figure 4.1: Modulated voltage and current relationship of the emissive cathode (100 shot average). (a) Temporal evolution of the mean cathode current (left axis, black) in response to an applied voltage with ac oscillations at 5 kHz (right axis, multi-coloured). The standard error of the mean current is the shaded region (grey), the standard error of the mean voltage is less than 10 mV. Amplitude (b) and phase (c) response of each applied pulse in (a). The phase reference is the voltage signal.

as it continuously decreases throughout the experiment. The emissive cathode model used previously to accurately depict the steady-state (dc) operation of the cathode does not currently predict the observed ac relationship [72]; the success of the cathode model in predicting past experiment results [73, 92] suggests it should be a strong candidate for an extension to time-dependent effects.

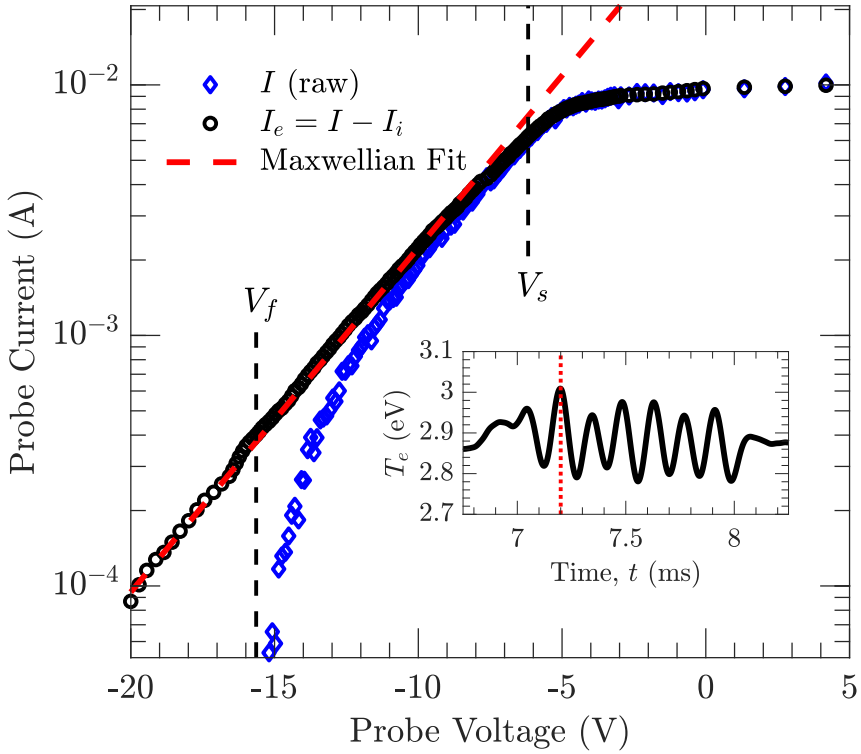

Figure 4.2: Current collected by the probe during an applied oscillation. The blue diamonds represent the raw current collected by the probe, the black circles are the adjusted electron current, and the red dashed line is the Maxwellian fit to the exponential region of the electron current. The black dashed lines indicate the floating potential and space potential. The inset figure shows a driven temperature oscillation and the dotted red line indicates the time the data in the main figure was collected.

To determine the time-resolved response of T_e, n, V_s, and V_f to the applied beam oscillations the reconstructed sweeps technique must be employed. At each measurement location the probe bias is held fixed over an entire shot and the shot is repeated 40 times. The probe bias is then increased by a small amount and the process is repeated. At each time-stamp, a quasi-instantaneous I–V curve is reconstructed to obtain high temporal resolution measurements. Fig. 4.2 shows a reconstructed sweep on a semi-log scale during one of the applied oscillations; the raw I–V curve (blue diamonds) is processed to determine the floating potential, V_f, space potential, V_s,

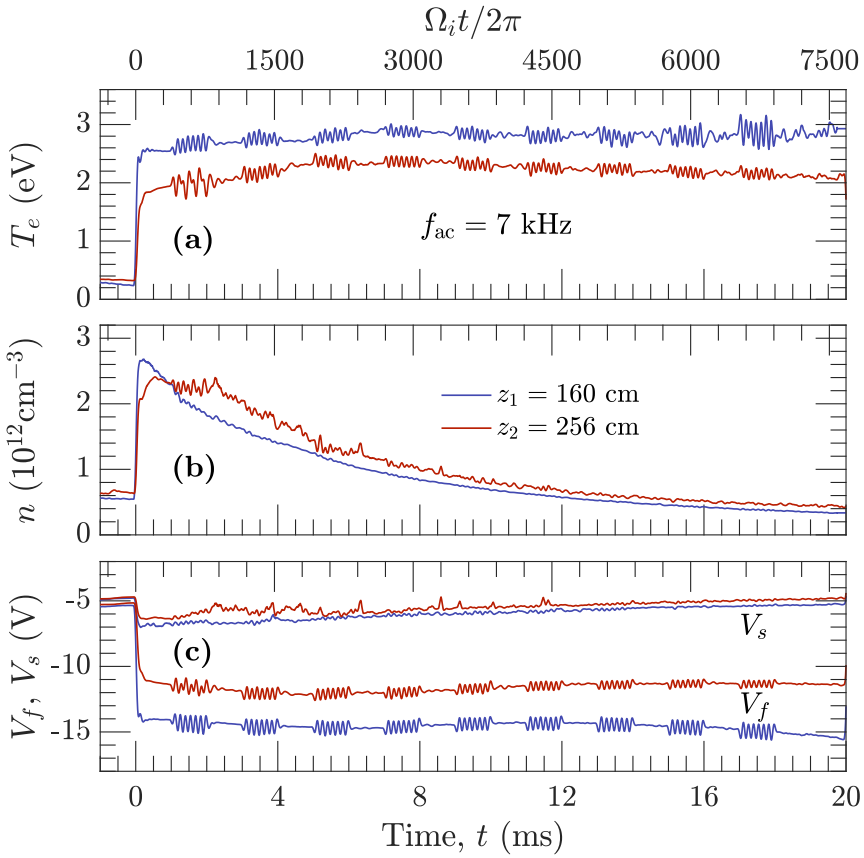

Figure 4.3: Response of plasma parameters to driven oscillations at two locations, $z_1 = 160$ cm (blue), and $z_2 = 256$ cm (red). (a) T_e, electron temperature, (b) n, density, (c) V_f, floating potential and V_s, space potential.

density, and electron temperature [68]. The quality of the data from these reconstructed sweeps provides a strong level of confidence in the post-processing results. The addition of the ac driver means that during each of the repeated shots the response of the plasma to the triggered oscillation is preserved as seen in the inset of Fig. 4.2 that shows a temperature oscillation in response to the beam oscillation. During the beam oscillation, the electron distribution remains Maxwellian as indicated by the linear fit (dashed red) of the electron portion of the probe current (black circles).

Fig. 4.3 shows the response of the plasma to the beam oscillations in the centre

of the filament at two axial locations, $z_1 = 160$ cm and $z_2 = 256$ cm for the same discharge as in Fig. 4.1(a). In Fig. 4.3(a) there are clear temperature oscillations with each applied pulse; at the further axial location, only the first pulse shows strong non-linear effects. While the actual beam power drops throughout the shot, the power per particle remains mostly constant due to the density decay and this results in a similar temperature oscillation amplitude for each pulse. The density in Fig. 4.3(b) shows nearly no response to the oscillating heat source except the first pulse at z_2, consistent with the non-linear response in the temperature at the same time and location; it is not presently understood what causes this result but it does not persist beyond the first pulse. During the first pulse the filament is still experiencing an increase in temperature at z_2 as the heated region extends further down the device; in contrast, the temperature at z_1 has reached a more stable state and this difference may be related to the non-linear oscillation and density perturbation. Together, Fig. 4.3(a) and Fig. 4.3(b) demonstrate that the oscillating input power drives thermal fluctuations and negligible density fluctuations, thus coherent fluctuations in ion saturation current from the ac driver can be interpreted as purely thermal beyond the first pulse. This aspect significantly reduces the time required to investigate the driver over many frequencies and improves the quality of the signal as no post-processing of I–V curves is required. Fig. 4.3(c) shows the response of the floating potential of the probe and the space potential of the plasma. Two features immediately stand out, the oscillations in floating potential and the distinct lack of oscillations in space potential; since $T_e \propto (V_s - V_f)$ this further confirms the oscillations are associated with temperature. The V_f oscillations provide a route for future experiments to more easily measure the temperature oscillations using a floating probe, instead of ion saturation current as the I_{sat} signal decays with the density. Preliminary analysis of the oscillations collected using a floating probe show significantly improved measurements over I_{sat}

due to a lower signal-to-noise ratio.

4.1.2 Thermal Waves and Resonance

With confirmation from the reconstructed sweeps that the driven oscillations correspond to temperature oscillations, measurements of the driver signal in the ion saturation current can be directly converted to oscillations in temperature using a second order expansion,

$$\delta T_e \approx 2\langle T_e \rangle \left(1 - \sqrt{1 - 2\frac{\delta I_{\rm sat}}{\langle I_{\rm sat}\rangle}}\right) \tag{4.1}$$

For a given driver frequency the Fourier transform of δT_e is equivalent to the thermal wave field at that frequency, $\mathcal{F}[\delta T_e(\mathbf{r}, t, \omega_{\rm ac})] \equiv \tilde{T}_e(\mathbf{r}, \omega_{\rm ac})$. The thermal wave field in the centre of the filament can then be constructed from collecting $I_{\rm sat}$ measurements across a range of driver frequencies and different axial locations. The ac shots at each driver frequency are repeated 100 times and averaged, the error in the wave field is determined from the standard deviation of the individual shots. As the fractional amplitude of the driver power is not constant in frequency or time (Fig. 4.1), the amplitude and phase $\mathcal{F}[\delta P/P] = |\tilde{P}(\omega_{\rm ac})|\angle\tilde{P}(\omega_{\rm ac})$ provide a convenient normalization for the thermal wave field at a single location.

Fig. 4.4(a) shows the amplitude of the thermal wave field at each pulse time for a single axial location, $z_1 = 160$ cm. The striking discontinuities at $t = 1, 3$, and 5 ms in the range of $\sim$ 20–30 kHz will be addressed first; as was shown in our earliest experiments [75] these features are due to the drift-Alfvén wave that has a large amplitude during the start of these shots. In the vicinity of the frequency of the large drift wave the averaged $I_{\rm sat}$ signal cannot be considered to be only from the thermal wave; there is likely to be a coupling of the thermal waves to the natural drift wave through the gradient. The coupling of the drift waves and thermal waves is outside

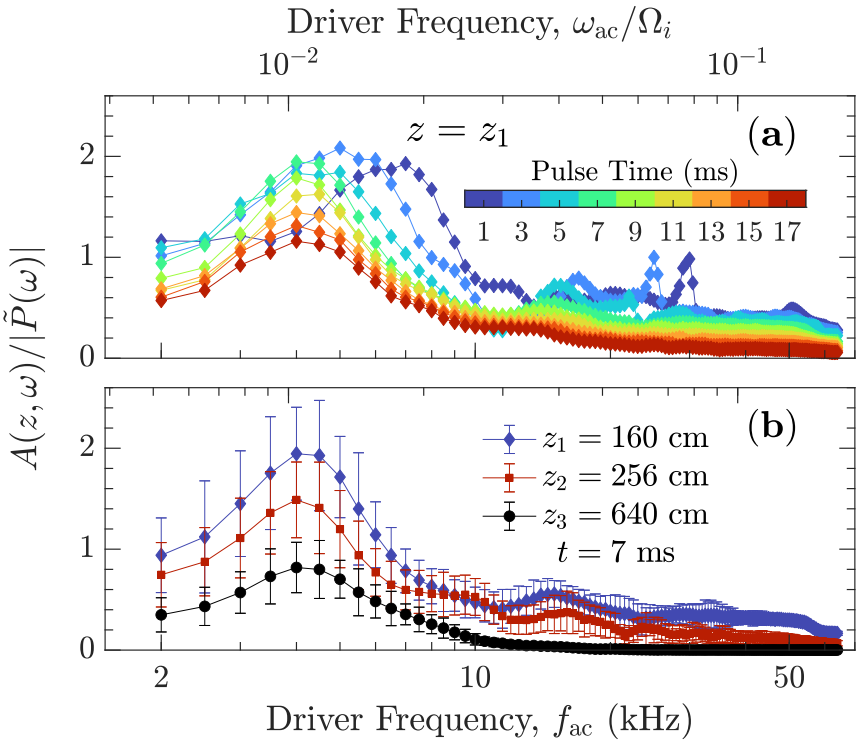

Figure 4.4: Thermal wave field amplitude $A(z,\omega)$ normalized to the fractional amplitude of the driver power $|\tilde{P}(\omega)|$. (a) Wave field at $z_1 = 160$ cm for each pulse. (b) Wave field for the pulse at $t = 7$ ms at three axial locations, z_1, $z_2 = 256$ cm, and $z_3 = 640$ cm. The error bars in (b) for z_1 are similar for each case in (a).

the present study and we note only the probable cause of these features. Beyond $t = 6$ ms the amplitude of the drift-Alfvén wave begins to reduce and the coupling becomes minimal.

A clear thermal resonance is observed between 2 kHz and 10 kHz, corresponding to the spontaneous mode observed in the dc shots. In the dc shots, the spontaneous thermal mode is not present throughout the entire discharge; the consistent peak in the ac shots demonstrates that the resonance condition exists even when the spontaneous mode is not excited naturally in the filament. The resonant frequency is initially closer to 8 kHz and decreases to a stable resonant frequency of around 4 kHz. In Fig. 4.4(b) the thermal wave field amplitude is shown for measurements at

three axial locations at $t = 7$ ms. At z_1 and z_2 the filament is present throughout the discharge, Fig. 4.3, while at $z_3 = 640$ cm, a defined filamentary structure is not established until just before the pulse at $t = 7$ ms. The resonance is observed to persist the length of the filament at a constant frequency, though at a reduced amplitude.

Previously, the origin of spontaneous thermal mode in the dc shots was proposed to correspond to a quarter-wave resonance and was supported by modelling of the filament length and thermal wave phase [18]; this is akin to the first acoustic resonance of the familiar single open-ended pipe. However, limited experimental evidence has been presented in support of this conclusion. If treating the filament homogeneously with the cathode end as a fixed-flux boundary (anti-node) and the opposite end as a fixed-field boundary (node) the resonant frequencies for the filament are approximately [27] (using Eq. (3.6)),

$$f_m \approx \frac{2\pi\chi_\parallel}{3}\frac{(m-\frac{1}{2})^2}{L^2}, \quad m = 1, 2, 3, ... \tag{4.2}$$

where $\chi_\parallel$ is an effective diffusivity over an effective filament length L, and m refers to the resonance order. With $m = 1$ corresponding to a $\lambda/4$ resonance, the effective length L can be determined from Eq. (4.2) using the resonant frequencies from Fig. 4.4(a) and the plasma parameters at $z_1 = 160$ cm for the effective diffusivity of the whole filament. Fig. 4.5 shows the comparison of the effective length over time with the known length of the filament determined from the time a signal is observed on probes at distant axial locations. Given the assumptions for determining the effective length, the experimental evidence strongly supports the previous conclusion that the resonance corresponds to a quarter-wave condition.

In Fig. 4.4(a) we note also the presence of a lower quality peak between 13 kHz and 20 kHz that may correspond to a second resonance. From Eq. (4.2) the $3\lambda/4$ resonance

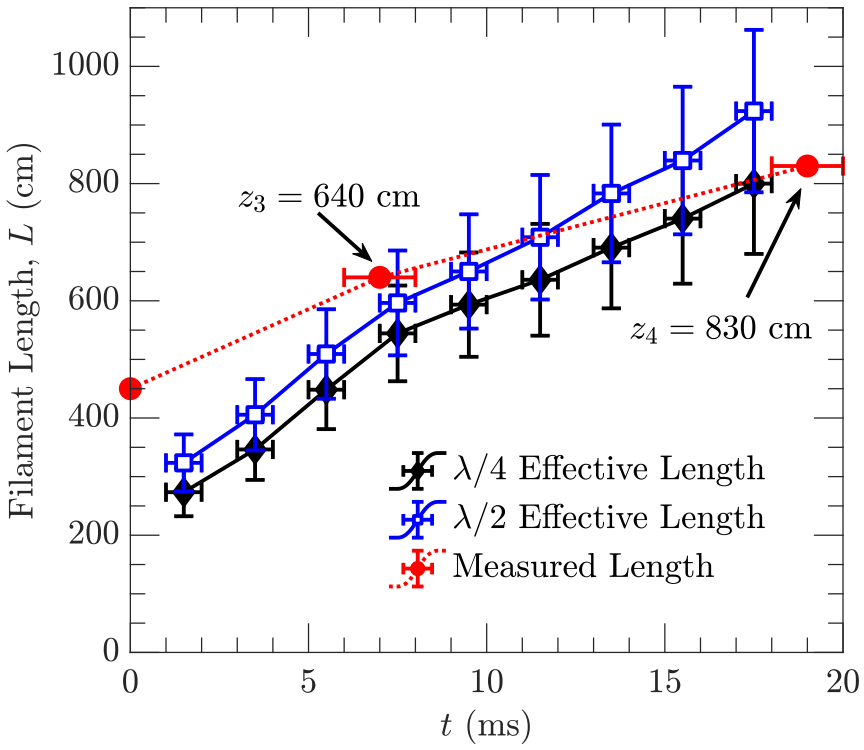

Figure 4.5: Comparison of the resonance conditions with the measured length of the filament. The measured length (circles, red dotted line) indicates the axial location and time when a signal from the filament is first seen on a probe. The effective length is determined for the quarter-wave resonance condition (diamonds, black solid line) using Eq. (4.2) for the first peak at around 4 kHz in Fig. 4.4(a), and for the half-wave resonance (open squares, solid blue line) using Eq. (4.3) and the second peak at around 15 kHz in Fig. 4.4(a).

would be expected to have frequencies, $f_{m2} = 9f_{m1}$, on the order of $35 - 70$ kHz, well beyond the observed resonance. While the far boundary was assumed to be fixed in Section 3.2, it cannot be expected to be perfectly insulating or perfectly thermally conducting and lies somewhere in between. Thus, thermal wave resonators can be expected to have resonances meeting both the node and anti-node boundary conditions [27]. Under fixed flux conditions at both ends of the filament, the resonant

frequencies are approximately,

$$f_m \approx \frac{2\pi\chi_\parallel}{3}\frac{m^2}{L^2}, \quad m = 1, 2, 3, ... \tag{4.3}$$

where m is the resonance order. Another estimate of the effective length can be made using the resonant frequencies of the second maximum and a half-wavelength condition ($m = 1$); this is shown in Fig. 4.5 and agrees favourably with the previous estimate. In light of the empirical evidence of both quarter and half-wave resonances, it is perhaps more appropriate to use a 3rd kind condition in the model; however, the quality of the half-wave resonance becomes very poor as the filament lengthens and does not exhibit any kind of spontaneous excitation indicating the boundary may be closer to the node condition. In this analysis the resonant frequency and an effective diffusivity are used to confirm the length; the opposite could also be done where the length of the filament and resonant frequencies are used to determine the diffusivity, as has been done in cavity length scanning experiments [28]. Additionally, we note that both resonances observed are *absolute* resonances in the amplitude; this behaviour is not predicted by homogeneous thermal wave models that only show resonances at Eqs. (4.2) and (4.3) relative to the semi-infinite field.

The phase of the thermal wave field normalized to the power is displayed in Fig. 4.6 in the same format as Fig. 4.4. Again, there is evidence of the drift wave interference in the first three pulses at z_1 in Fig. 4.6(a). The phase can, and does, lead the power at lower frequencies; this is a consequence of thermal waves lacking a physical definition of a wavefront. The pulse signal cannot violate causality and appear before the power is applied, however, the instantaneous phase of the thermal field can lead the phase of the source as there is no wavefront propagating through the plasma in analogy to hyperbolic wave equations. At the resonances, the phase lag is reduced as thermal

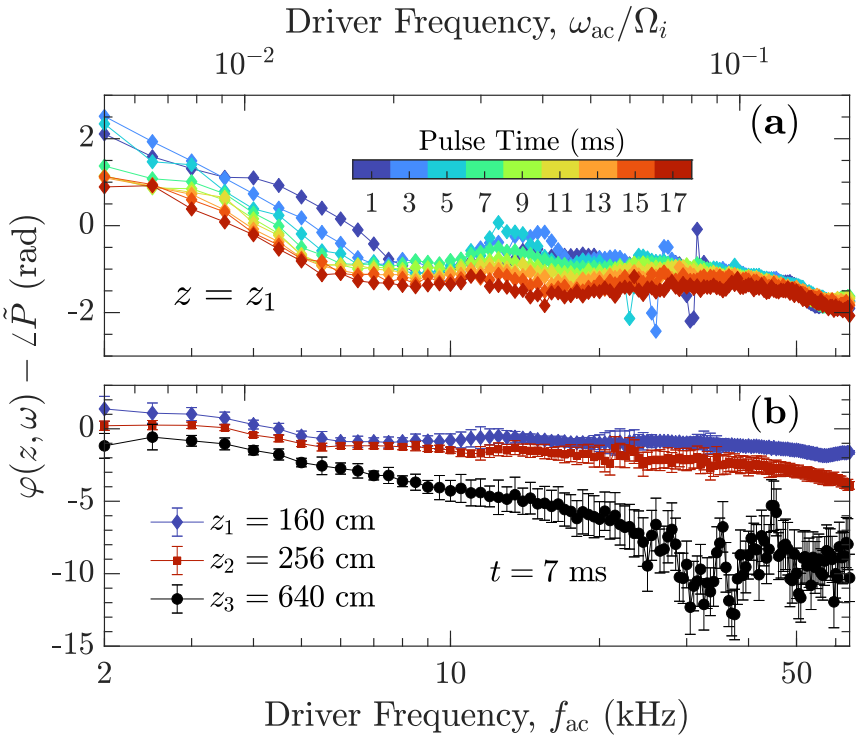

Figure 4.6: Thermal wave field phase $\varphi(z,\omega)$ normalized to the beam power fluctuation phase $|\angle P(\omega)|$. (a) Wave field at $z_1 = 160$ cm for each pulse. (b) Wave field for the pulse at $t = 7$ ms at three axial locations, z_1, $z_2 = 256$ cm, and $z_3 = 640$ cm. The error bars in (b) for z_1 are similar for each case in (a).

wave power accumulates. In Fig. 4.6(b) the phase is seen to lag with distance, as expected. At z_3 the disruption in the phase trend at high frequencies is believed to be an inhomogeneous conductivity effect, but could also be due to the poor signal strength seen in Fig. 4.4(b).

The phase and amplitude at a single location are a product of the inhomogeneous conductivities in the experiment and are not predicted well by the homogeneous model. An approximation to the homogeneous model presented in Section 3.2 can be obtained by using the phase difference and amplitude ratio between two axial locations near each other [75]. Fitting $\varphi_{1,2}$ or $A(z_2)/A(z_1)$ using the laterally infinite model returns a measurement of the parallel thermal diffusivity $\chi_\parallel$, and in principle,

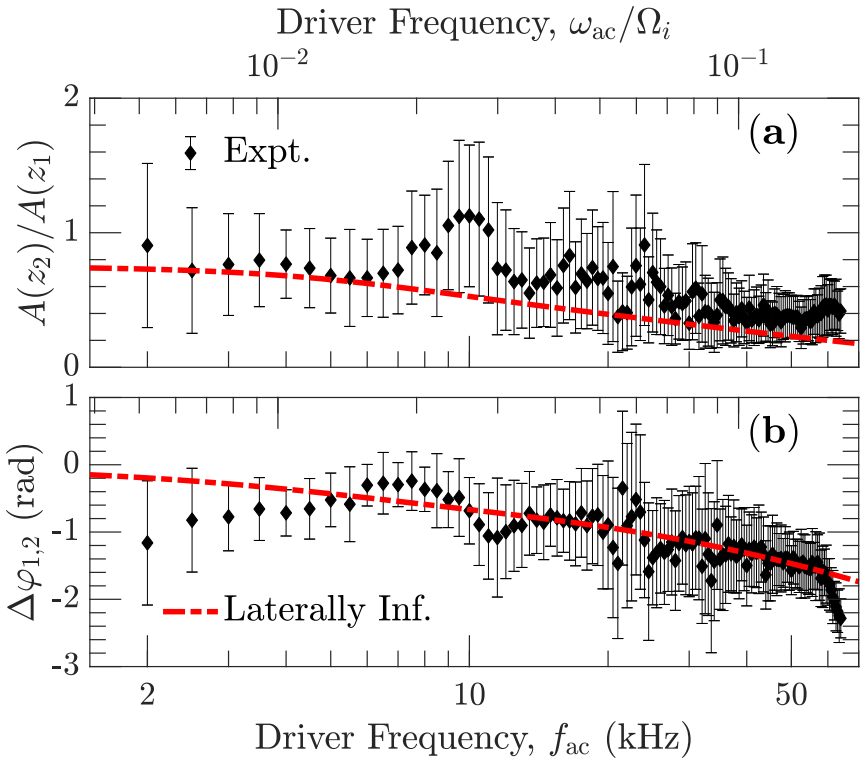

Figure 4.7: Thermal wave field comparison between experiment (black diamonds) and the laterally infinite model (red dashed) at two locations, $z_1 = 160$ cm and $z_2 = 256$ cm. (a) Amplitude ratio. (b) Phase Difference

the anisotropy ratio $\kappa_\parallel/\kappa_\perp$. In practice the phase is the more accurate measurement but has very little sensitivity to the anisotropy ratio making any estimates of it subject to a high degree of error, thus only $\kappa_\parallel$ and n are varied in the fit, while $\kappa_\perp$ is determined from Eq. (3.2) based on the variable parameters – this amounts to the assumption that the cross-field conductivity is classical when performing the fit. An improvement to the signal-to-noise ratio is required to make an accurate measurement of the anisotropy ratio.

The result of fitting the pulse at $t = 7$ ms between z_1 and z_2 is shown in Fig. 4.7. The fit is made to the phase, while the predicted amplitude based on this fit is compared to the measured amplitude. There is good agreement with the overall trend of

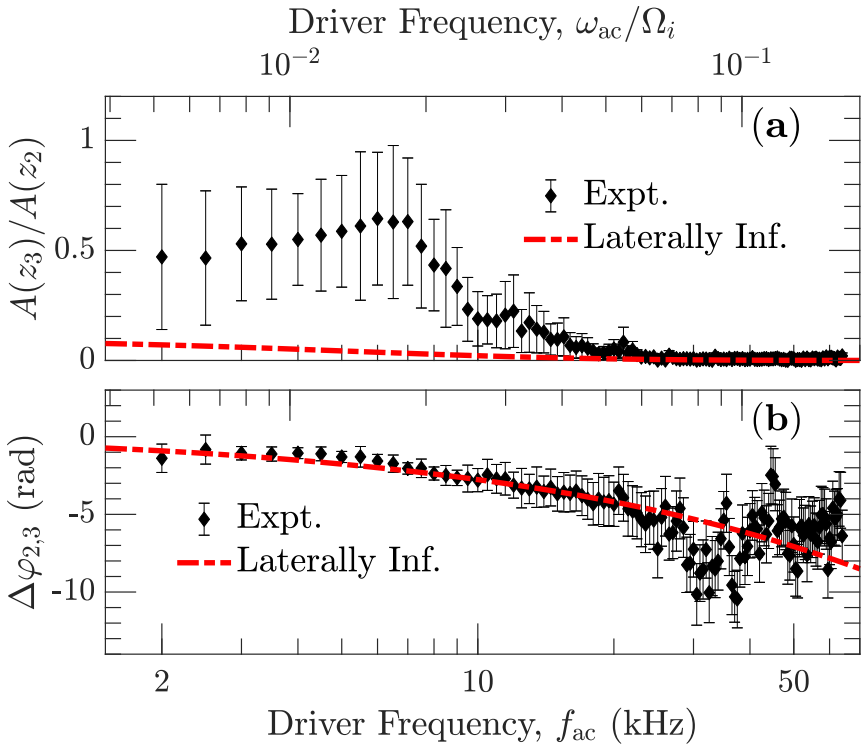

Figure 4.8: Thermal wave field comparison between experiment (black diamonds) and the laterally infinite model (red dashed) at two locations, $z_2 = 256$ cm and $z_3 = 640$ cm. (a) Amplitude ratio. (b) Phase Difference

the phase in Fig. 4.7(b). At low frequencies the phase lags more than predicted, the linear approximation is expected to break down at lower frequencies as the thermal diffusion length increases. The deviations at ~ 10 kHz and ~ 60 kHz are both due to the small oscillations that occur in the phase in Fig. 4.6(b); these are likely inhomogeneous conductivity effects observed at one location. The amplitude in Fig. 4.7(a) also agrees favourably with the predicted trend, notably the saturation predicted at low frequencies due to the fixed field boundary. A better fit to the amplitude can be made at the expense of fitting the phase. The peak at ~ 10 kHz is again due to small oscillations in the amplitude seen in Fig. 4.4(b). A minor effect of the drift wave is seen in both the phase and amplitude between 20 and 30 kHz.

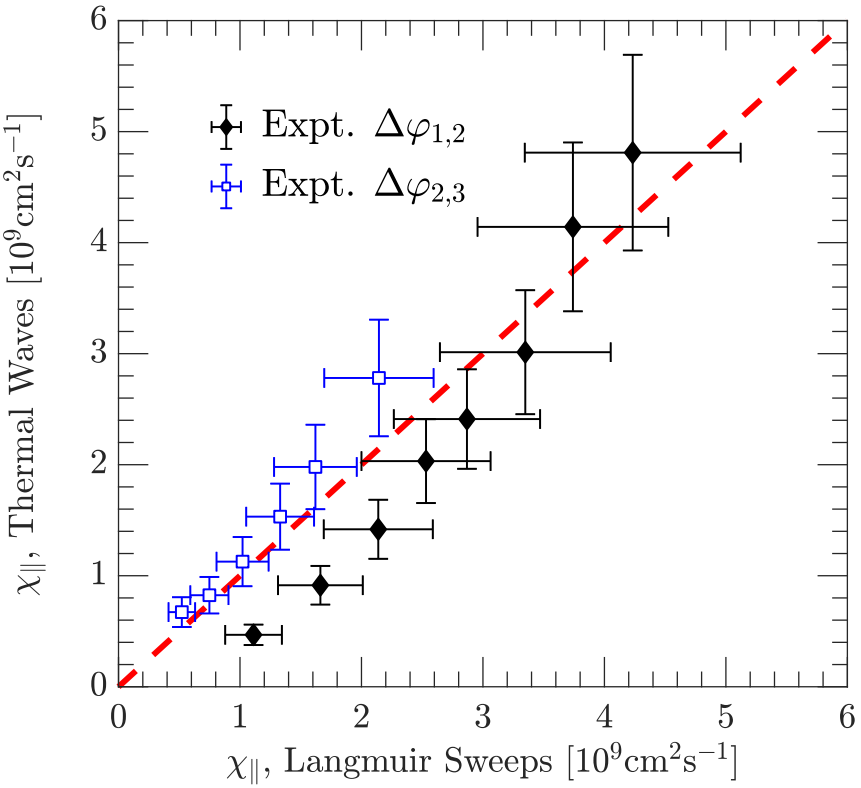

Figure 4.9: Comparison of parallel thermal diffusivity, $\chi_\parallel$, measured from the phase of the thermal wave field and calculated using Eq. (3.2) with average plasma parameters determined from the Langmuir I–V sweeps. The filled black diamonds indicate measurements between z_1 and z_2, the hollow blue squares indicate measurements between z_2 and z_3, and the red dashed line represents agreement between the two measurements. The plasma parameters used in Eq. (3.2) are the averages of the two locations.

The linear approximation can be further extended to measurements made at z_2 and z_3, being nearly 400 cm apart this stretches the limits of an approximation of homogeneity. Still, in Fig. 4.8(b) we see that the phase is a good fit over much of the frequency range investigated. The deviation at high frequencies is either an inhomogeneous effect or due to poor signal strength, as mentioned earlier. However, the model is clearly a poor fit for the amplitude ratio in Fig. 4.8(b). At low frequencies, the amplitude of the thermal waves at z_3 is much greater than expected by the

homogeneous model. The saturation of the amplitude at low frequencies still occurs, providing a qualitative agreement with the predictions of the bounded model.

To verify the thermal wave field fit, the $\chi_{\|}$ obtained from each pulse is compared with $\chi_{\|}$ calculated using Eq. (3.2) and the average parameters from the I–V sweeps; this result is shown in Fig. 4.9. The first pulse for $\varphi_{1,2}$ is omitted due to the clear non-linear oscillations at z_2 (Fig. 4.3) and $\varphi_{2,3}$ only for pulses after the $t = 5$ ms pulse as the filament is not yet at z_3. Given the assumptions of the model, namely homogeneous conductivities and no volume sources or sinks, the comparison provides strong experimental evidence that thermal waves are being excited by the driver and are a useful tool for estimating the thermal diffusivity independent of knowledge of the electron temperature.

4.1.3 Broadband Excitation

In our earliest experiments [75] it is observed that some sinusoidal pulses near the resonant frequency result in a ringing of the oscillations beyond the length of the driver signal and that excitation of the thermal resonance is sensitive to even small perturbations. In Fig. 4.10 the amplitude of the thermal wave is measured for varying amplitudes of the source modulation. At 8 kHz the thermal resonance is observed and persists across all the driver amplitudes. In particular, even at the lowest driver amplitude, $\delta V/V_{\mathrm{dc}} = 0.05$, the resonance is distinct and demonstrates that even a small perturbation is capable of exciting the resonator. The quality factor of a resonator, Q, is defined as,

$$Q = \frac{f_R}{\Delta f_R}, \quad \Delta f_R \equiv FWHM \tag{4.4}$$

where f_R is the peak frequency of the resonance and Δf_R is the width of the resonance defined by the full width at half maximum (FWHM). For the resonance in Fig. 4.10

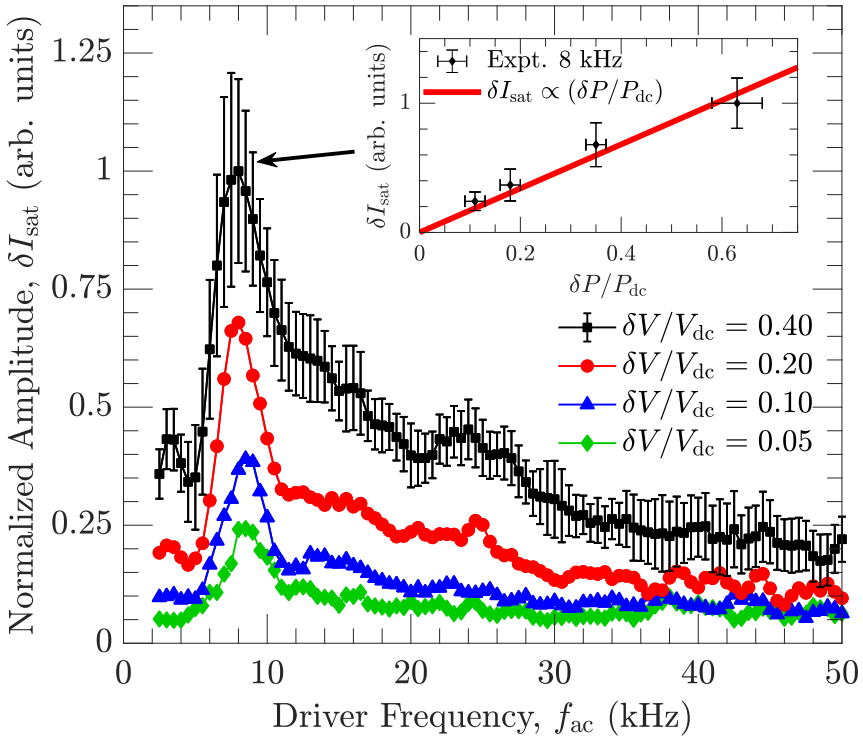

Figure 4.10: Thermal wave field amplitude at $z = z_2$ for different driver frequencies, $f_{\rm dc}$, and amplitudes, $\delta V/V_{\rm dc}$. The curves are all normalized to the maximum of the $\delta V/V_{\rm dc} = 0.40$ case and the fractional error at $\delta V/V_{\rm dc} = 0.40$ is similar for the other cases. Inset, the $\sim$ 8 kHz amplitude resonance shows a linear scaling of $\delta I_{\rm sat}$ with respect to the amplitude of the oscillations in the driving power.

this corresponds to $Q \sim 2$, and is consistent with the low quality factors associated with TWRCs in other forms of matter [27].

The inset of Fig. 4.10 shows the relationship at 8 kHz between $\delta I_{\rm sat}$ and the modulated input power to the heat source from the electron beam, $\delta P/P_{\rm dc}$, which shows a linear dependence. This demonstrates that the amplitude of the (driven) resonant temperature oscillations scales linearly with the amplitude of the oscillating heat source over the range investigated, since to first-order $\delta I_{\rm sat} \propto \delta T_e$ when the oscillations are purely temperature. This $\delta T_e \propto \delta P$ relationship is consistent with the result of the nonlinear transport code, described earlier, that models the experiment.

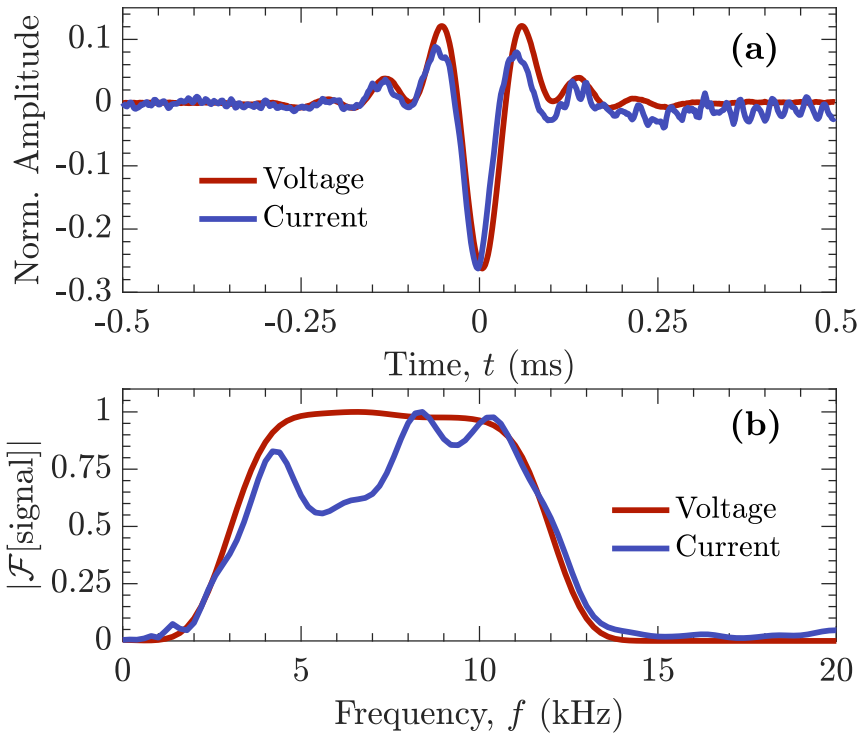

Figure 4.11: Voltage and current signals of the 3–12 kHz broadband pulse applied to filament. (a) temporal domain with amplitude normalized to the dc level (b) frequency domain normalized to peak frequency in the pulse range. The signals are from 20 shot averages of a 10 V dc discharge with a 4 V peak-to-peak ac amplitude.

Not shown in Fig. 4.10 is the maximum amplitude of the driver investigated, $\delta V/V_{\text{dc}} = 0.8$; at this amplitude, the relationship between driver and driven oscillations is no longer linear and the thermal oscillations are non-linear and over-driven.

To investigate the resonance excitation further a short broadband pulse is added to the discharge bias to perturb the filament before the spontaneous excitation of the thermal wave. The broadband pulse is constructed in the frequency domain from a rectangular function convolved with a Gaussian function and has the form of a bandpass filter with 9 kHz FWHM. The 3 dB point at the low-frequency band edge is 3kHz, and 12 kHz at the high-frequency band edge. A 20 shot average of the pulse in the discharge voltage and current is shown in the time and frequency domain in

Fig. 4.11; the dc voltage is 10 V and the ac amplitude is 4 V peak-to-peak.

In Fig. 4.12(a) a single dc shot (black trace) is displayed during the start of the discharge. Initially, there is a strong drift-Alfvén wave and at t greater than 3 ms the excitation of the spontaneous mode is observed. Also included in Fig. 4.12(a) is the single-shot filtered over the range $3 - 12$ kHz (red trace), and a 20 shot average (blue trace). The 20 shot average shows nearly no evidence of the spontaneous thermal mode (or drift wave) due to the shot-to-shot phase variability. However, the time when the thermal mode becomes unstable and grows is consistent between the shots with the spontaneous excitation occurring between 3 and 3.25 ms. The spontaneous resonance remains until ~ 8 ms when the filament transitions to a more turbulent state and it experiences strong damping.

Figs. 4.12(b), (c), and (d) show the 4 V amplitude pulse applied at different times, t_p, prior to the excitation of the spontaneous mode. For $t_p = 1$ ms the pulse produces a non-linear ringing of the pulse and eventually a small amplitude sinusoidal oscillation before the spontaneous mode is expected; this is observed as a modulation of the drift wave in the raw data and clearly in the filtered time trace. The frequency of these non-driven oscillations closely matches the spontaneous mode. The amplitude then grows at the same time as the dc excitation, leading to the conclusion that this growth is from the normal excitation mechanism. However, the 20 shot average shows that the phase of the excited oscillations is not repeatable shot-to-shot. Pulses applied before 1 ms produce only short-lived non-linear oscillations as the filament is generally still setting up.

At $t_p = 1.5$ ms a similar result is observed with the main difference being the perturbation creates a stronger ringing and the 20 shot average shows the initial phase of the excited resonance is more consistent and the pulse rings down slowly as the phase begins to drift in each shot. At $t_p = 2.5$ ms the stimulated excitation has an

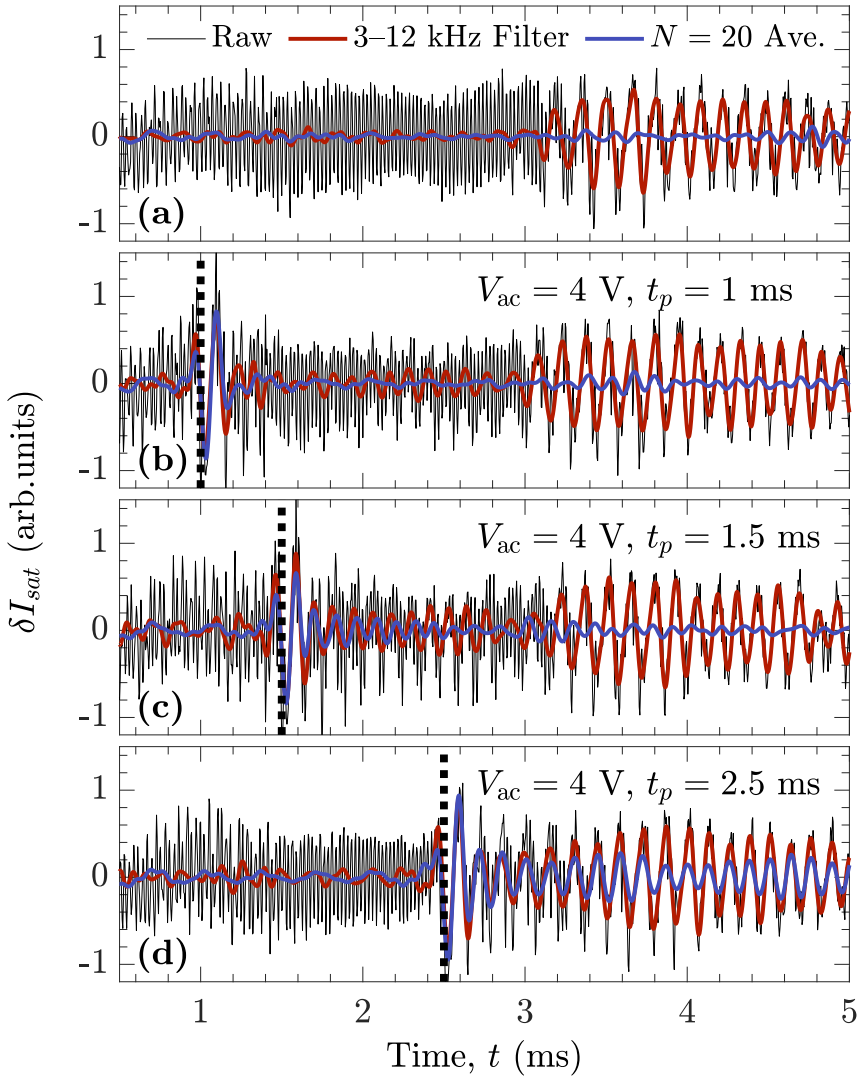

Figure 4.12: Filament response to broadband pulses with $V_{ac} = 4$ V peak-to-peak at different times, t_p, before the spontaneous thermal resonance is excited. (a) dc shot with $V_{dc} = 10$ V showing the drift-Alfvén wave and excitation of the spontaneous thermal mode at $t > 3$ ms. (b), (c) and (d) show broadband ac shots with the pulse applied at $t_p = 1.0$, 1.5, and 2.5 ms, respectively. The black trace shows a raw single shot, red the same shot band-pass filtered between 3 and 12 kHz, and blue the average of 20 repeated shots. Data collected at $z_2 = 256$ cm.

amplitude comparable with the spontaneous oscillations that begin shortly after. The 20 shot average shows the application of the perturbation produces a synchronization of the phase that persists into the natural resonance. The same result is observed if the pulse is applied closer to 3 ms or even after the spontaneous mode has already appeared.

In Fig. 4.13 the variation of the amplitude of the pulse at $t_p = 2.5$ ms is investigated. For an amplitude of 1 V (peak-to-peak) it is seen that even a small amplitude perturbation is capable of stimulating the natural resonance; however, the phase does begin to drift and gives the appearance that the oscillations decay in the 20 shot average. At 8 V the filament again experiences synchronization of the phase as in the 4 V perturbation but only for a limited time. This may indicate the filament can be perturbed too strongly and disrupt the dc evolution of the filament and the natural resonance. This is supported by the result at 16 V, where the large perturbation still excites the oscillations but the phase synchronization is almost non-existent.

The broadband pulse is much like striking a guitar string or blowing over a pipe where the non-resonant frequencies are rapidly damped and the resonator rings with a single frequency. The general result that the pulse can trigger the natural thermal oscillation of the filament before it spontaneously excites reveals that the resonance is marginally stable. It remains unclear what causes the natural excitation to occur in the dc shots. Further experiments with the broadband pulse may be useful in investigating the resonance as the phase can be synchronized shot-to-shot and the stability can be probed.

4.1.4 Discussion

In this section, we discuss the relationship between the experiment and theoretical model presented in Section 3.2 which has made some simplifying assumptions. The

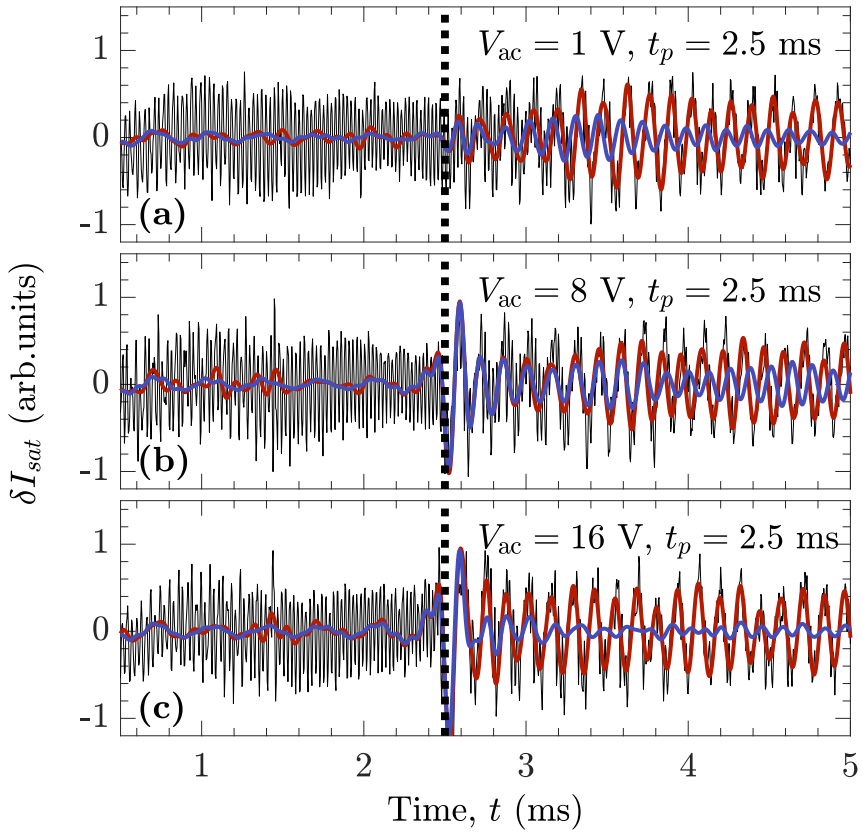

Figure 4.13: Filament response to broadband pulses applied at time $t_p = 2.5$ ms with different ac amplitudes. (a), (b) and (c) show broadband ac shots with peak-to-peak pulse voltages of 1,8, and 16 V, respectively. The black trace shows a raw single shot, red the same shot band-pass filtered between 3 and 12 kHz, and blue the average of 20 repeated shots. The corresponding dc shot can be seen in Fig. 4.12(a) and the pulse at 4 V amplitude in Fig. 4.12(d). Data collected at $z_2 = 256$ cm.

T_e and n profiles are inhomogeneous, both radially and axially, and lead to inhomogeneous conductivities; the model assumes homogeneity and the comparison shows this is a reasonable approximation for determining the average $\chi_{\|}$ between two locations over a wide frequency range (Fig. 4.9). However, over the frequency range investigated there are measured deviations from the homogeneous thermal wave field prediction (Figs. 4.7 and 4.8) and the model does not capture these observed thermal wave interference phenomena. The effects of inhomogeneities have been investigated previously

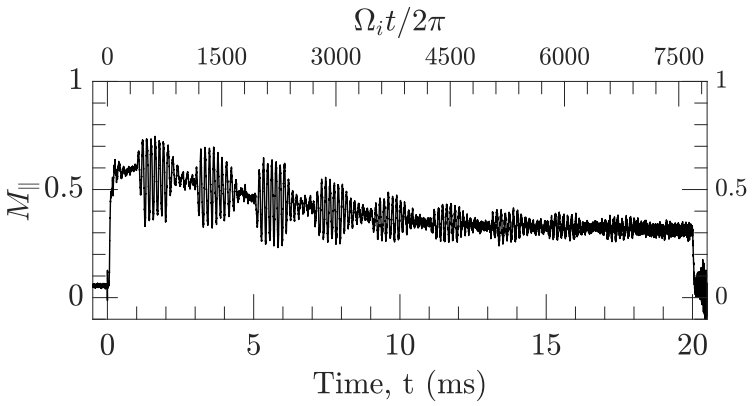

Figure 4.14: Mach number of the parallel flow in the center of the filament at $z =$ 450 cm with 7 kHz driven oscillations. The flow is modulated by the driver and follows a similar amplitude profile as the thermal waves as the frequency is varied (Fig. 4.4).

in thermal wave experiments and modelling for the depth profile reconstruction of inhomogeneous solid materials [48, 76]. We have already engaged in preliminary one-dimensional modelling using some of these techniques and they show great potential in describing our experiment results, suggesting that the structures in the phase and amplitude are a result of the inhomogeneous conductivities. These results will be presented in a forthcoming publication.

Furthermore, the electron temperature is coupled to the other transport equations of motion and continuity. While the density fluctuations are very small and can be ignored the same cannot be said of the plasma flow. There exist axial and azimuthal flows in the plasma but steady-state convection has been neglected entirely. The axial flow also experiences modulation from the driver, seen in Fig. 4.14 that displays the axial Mach number ($v_\parallel/c_s$) at $z = 450$ cm. This was accomplished using a two-sided Mach probe aligned along the axis of the device; the ratio of the saturation current collected by each face of the probe can be used to determine the Mach number using $M_\parallel = 0.45 \ln(I_{\text{sat1}}/I_{\text{sat2}})$ where the subscripts 1 and 2 refer to each face of the probe [93]. We feel it is important to mention the Mach probe is large relative to the

cross-sectional area of the filament and alters the discharge current significantly. It is reasonable to assume that the observed flow modulation is not induced by the presence of the probe; however, a comparison of the flow oscillations with the thermal waves cannot be made as the dc evolution of the filament is not the same. The modulation amplitude dependence on frequency is similar to the thermal oscillations (Fig. 4.4) with a resonance around the spontaneous thermal wave as expected by the equation of motion. The modulation of the flow by the spontaneous thermal wave has been previously observed [66] and this is consistent with the measurements made here using driven thermal waves. The model presented could be improved by including coupling to the axial plasma flows as they play a role in the behaviour of the driven oscillations; the zeroth-order $\mathbf{E} \times \mathbf{B}$ perpendicular flows can justifiably be neglected because of the $m = 0$ azimuthal symmetry of the thermal oscillations.

Last, in modelling the thermal flux source as a boundary condition we ignored possible volume sources and sinks in the plasma, such as Joule heating, ballistic heating, and energy exchange with the ions; sources that may also be dependent on the local temperature. The impact of these terms on the thermal wave field in the low-frequency limit is to produce a thermal wave field that becomes everywhere in phase with the oscillating source and otherwise independent of frequency, while at higher frequencies the field reduces to the source free thermal wave field; similar to carrier-density diffusion waves with carrier lifetimes [49]. As we do not observe these effects they are likely more relevant at lower frequencies than investigated here. Complicating any investigation of lower frequencies with the current setup is that for frequencies < 1 kHz the parameters of the filament would measurably change over the time of an oscillation.

4.2 Radial Experiments

Following the axial thermal wave experiments, it is natural to progress to a study of the cross-field structure of the thermal wave field. The experiment setup for this series of experiments is similar to that displayed in Fig. 2.2(a). In these experiments there is only a single filament source and a Langmuir probe is inserted at $z_1 = 192$ cm, as measured from the crystal cathode. There is a voltage sensor measuring the bias between the crystal cathode and mesh anode, and Rogowski coils measure the electron current to the crystal cathode and from the anode.

4.2.1 Improved Measurements

In our axial experiments, one of the unforeseen outcomes is that the floating potential of the Langmuir probe shows a surprisingly clear response to the thermal wave driver (see Fig. 4.3), while the space potential remains unchanged by the modulation. The driven oscillations are fluctuations in temperature and since $V_s - V_f$ is proportional to T_e we have [68],

$$\delta(V_f - V_s) = \delta V_f \propto \delta T_e \tag{4.5}$$

and fluctuations in V_f are directly proportional to the thermal wave field, which is a significant improvement on the ion saturation current relation in Eq. (4.1). It is important to stress that just like the relation in Eq. (4.1), the outcome of Eq. (4.5) only certainly holds for the driven temperature oscillations and not all fluctuations in V_f. That one of V_f or V_s should remain unchanged during the thermal oscillations was an oversight on our part, nevertheless, we can now take advantage of this.

To further investigate if V_f is a useful diagnostic for analyzing the pressure filaments two identical dc planes are collected, the first while collecting I_{sat} and the

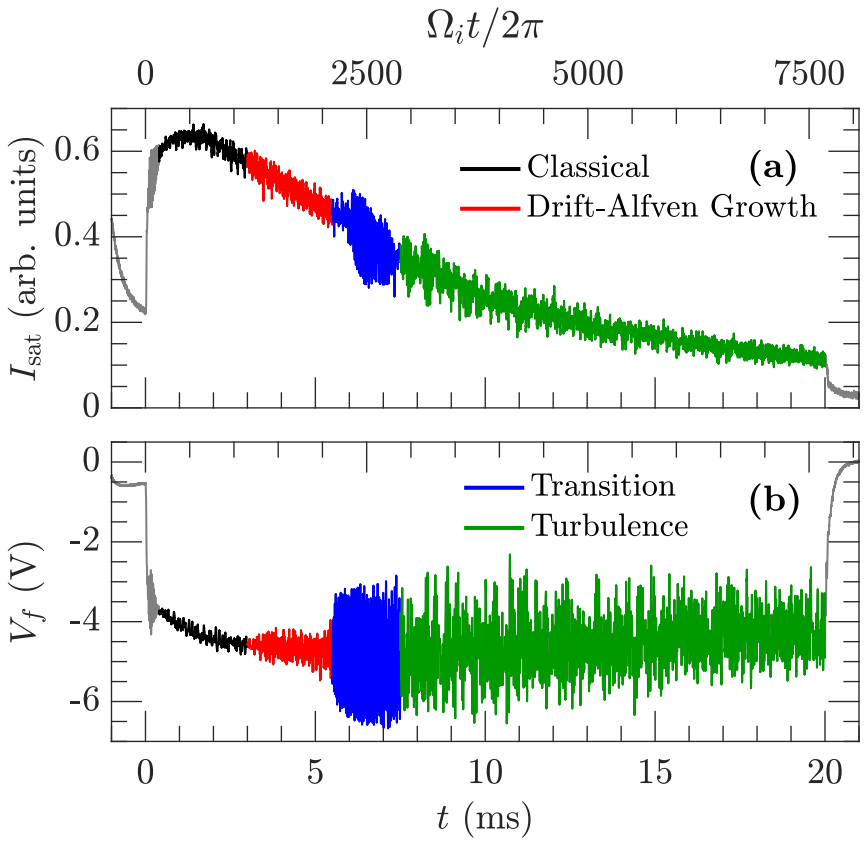

Figure 4.15: Comparison of (a) I_{sat} and (b) V_f temporal measurements showing the different phases of the filament evolution.

second while measuring V_f. I_{sat} is collected by biasing the probe very negative with respect to the machine wall and is discussed in Chapter 2. The floating potential is obtained by introducing an unbiased probe to the plasma and measuring the resulting potential from charging by the plasma. Fig. 4.15 shows single-shot measurements of I_{sat} and V_f on the gradient of the filament. The same features are identifiable in both measurements and indicate that V_f contains the same fluctuation information as I_{sat}; this is true across the entire data plane. The amplitude of the δV_f signal is significantly greater than δI_{sat}, this has a profound impact on the signal-to-noise ratio (SNR) of the signals. Moreover, the exponential decay of the density is not observed,

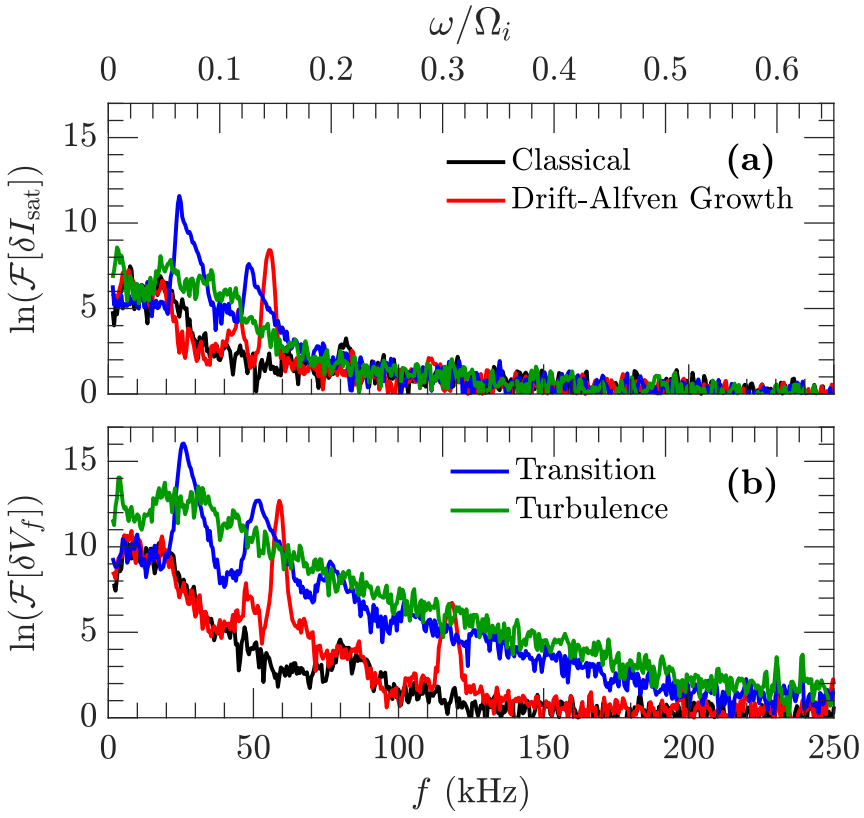

Figure 4.16: Comparison of (a) $I_{\rm sat}$ and (b) V_f spectral measurements showing the different phases of the filament evolution.

since V_f is not strongly related to the density [68], and no reduction in the SNR is observed throughout the shot, as it is in $I_{\rm sat}$. It is unfortunate this was not noticed in the decades before as the quality of much of the data in the past and current experiments would be significantly improved had V_f been used.

A low dc voltage of 10 V for the cathode bias results in the filament evolving through four distinct phases that are visible in Fig. 4.16: classical transport (black), drift-Alfvén growth (red), transition (blue), and turbulence (green). The Fourier spectra of the ensemble average of 5 shots are shown in Fig. 4.16 for each of the four highlighted regimes. The spectra are shown relative to plasma shots of the cold background plasma and indicate power above what is observed in the absence of the

pressure filament; the vertical scales are made identical to demonstrate the difference in SNR. The classical regime is characterized by only incoherent low-frequency fluctuations and it is already clear that V_f is a superior fluctuation measurement method. In the drift-Alfvén growth phase, a distinct peak is observed at around 60 kHz and in V_f a harmonic at 120 kHz is also visible; the drift-Alfvén wave frequency is slightly lower in I_{sat} at around 55 kHz and the peak of a harmonic can be seen at 110 kHz, though the noise level of the I_{sat} mostly obscures it. In the transition phase, growth and steepening of the drift-Alfvén wave shows the expected harmonic generation[15], with up to four visible in V_f while only two are seen in I_{sat}. The characteristic exponential frequency spectrum is visible in the transition and turbulent regimes due to the generation of Lorentzian-shaped pulses; the power of this broadband spectrum above the background level in V_f compared to I_{sat} is remarkable.

One of the barriers to thermal wave experiments in any media is the high spatial attenuation of the thermal wave field. Using I_{sat} the driven thermal wave signal is unobservable beyond a few mm from the center of the filament; even the 100 shot averaging does not extract a useful signal. Fig. 4.17 shows an average of 40 ac shots of δV_f at $r = 0$ mm and $r = 8$ mm. The amplitude of the driving signal is $\delta V/V \approx 0.25$ and two frequencies, $f_{\text{ac}} = 7$ kHz and $f_{\text{ac}} = 45$ kHz, are shown. The shots at $r = 8$ mm correspond to the red traces and use the right vertical scale that is a factor of 10 smaller than the left scale. The driven thermal waves are visible down to measurements on the order of 10 mV. Thus, using V_f to reduce the SNR gives access to high precision measurements of the cross-field thermal wave field well beyond the center of the filamentary structure.

The radial temperature profile for each of the regimes described above are shown in Fig. 4.18(a). These profiles were obtained using high-quality reconstructed Langmuir

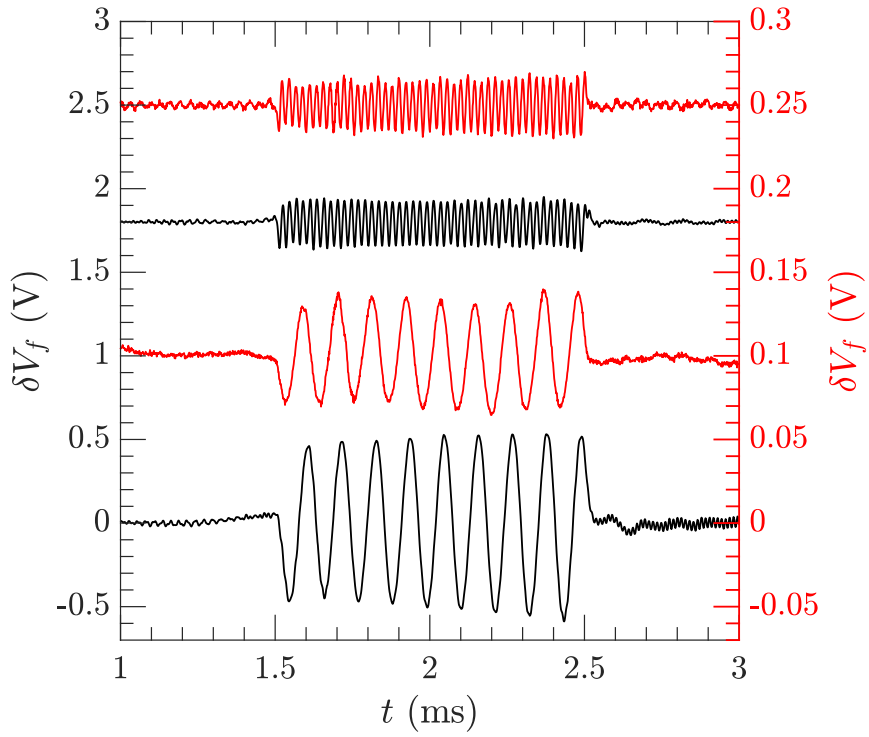

Figure 4.17: Example of V_f signals in the center of the filament (left axis, black) and at $r = 8$ mm (right axis, red). The low frequency measurements are at $f_{ac} = 7$ kHz and the high frequency at $f_{ac} = 45$ kHz. The right scale is a factor of 10 smaller than the left and the dc offset of the signals is arbitary.

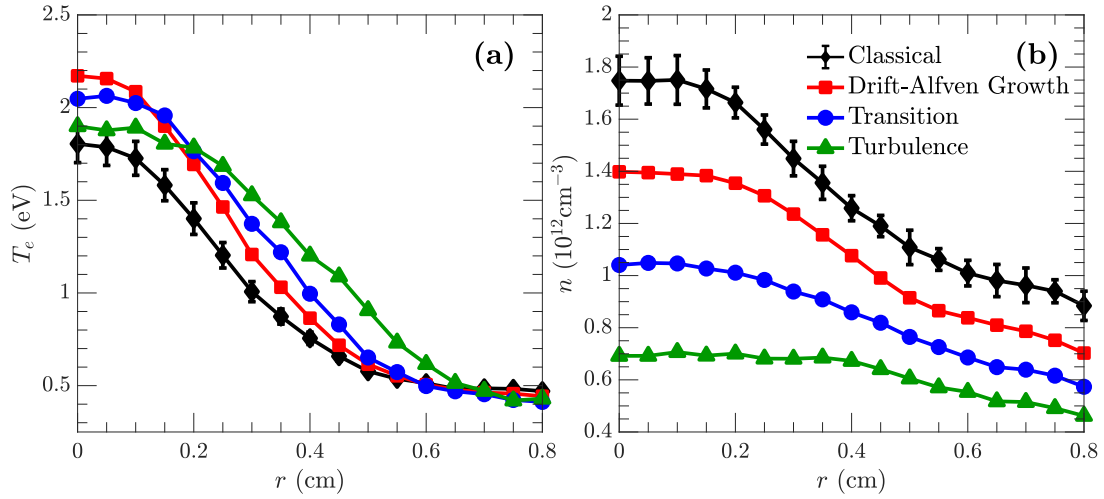

Figure 4.18: Comparison of (a) T_e and (b) n profiles in the different phases of the filament evolution. The profiles are obtained from reconstructed Langmuir sweeps and the error for all cases is similar to that seen on classical phase.

sweeps. The black profile corresponding to the early phase has the Gaussian-like profile expected of purely classical transport and the result agrees well with the observed lack of coherent wave modes [16]. The filament temperature continues to increase into the wave growth phase and maintains the profile from the classical phase; coupled with the lack of intermittent fluctuations it is likely the drift waves are not yet enhancing the cross-field transport. In the transition and turbulent phases, the filament is experiencing anomalous cross-field transport processes, evidenced by the decrease in the peak temperature of the profile and enhanced radial extent. It is well established [15] that the drift-Alfvén waves lead to an enhanced cross-field transport phase characterized by the exponential spectra seen in the transition and turbulent regimes. In Fig. 4.18(b) the corresponding density profiles are displayed. The density enhancement is mostly stable across the regimes and exhibits the characteristic decay of the afterglow plasma density. These cases represent an array of transport regimes in which to study the cross-field structure of the thermal wave field.

4.2.2 Thermal Wave Field

To measure the evolution of the thermal wave field through the different transport regimes the pulse train technique used in the axial experiments is repeated here. A frequency sweep is made over the range $f_{\mathrm{ac}} = 2$–$50\,\mathrm{kHz}$ in $1\,\mathrm{kHz}$ steps with an amplitude $\delta V/V_{\mathrm{dc}} \approx 0.25$. An ensemble of 40 shots is collected at each frequency and each position along a horizontal line with $y = 0$ cm and $x = 0$–0.8 cm in 0.05 cm steps. The resulting thermal wave field is shown in Figs. 4.19, 4.20 , 4.21, and 4.22 as the filament evolves through the classical, wave growth, transition, and turbulence regimes, respectively. The amplitude is displayed in log format, the phase is in radians, and the colour scale matches the vertical or z-axis.

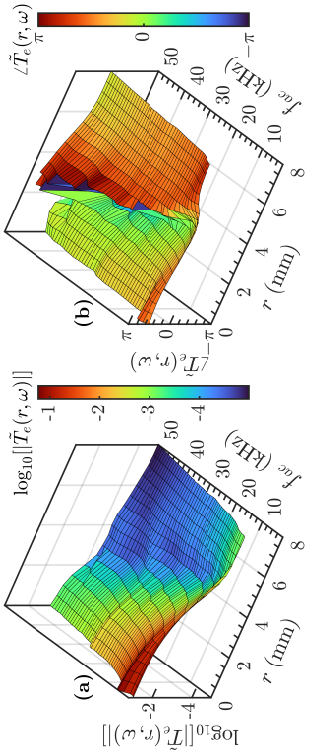

Figure 4.19: Thermal Wave Field during the classical transport phase. (a) Amplitude (b) Phase.

Figure 4.20: Thermal Wave Field in the drift-Alfvén growth regime with two thermal resonances. (a) Amplitude (b) Phase.

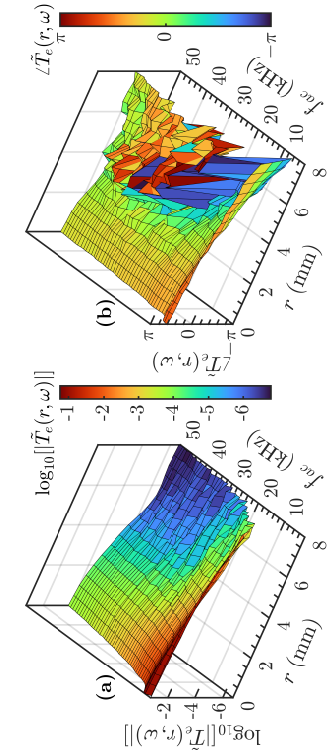

Figure 4.21: Thermal Wave Field in the transition regime with drift-wave coupling. (a) Amplitude (b) Phase.

Figure 4.22: Thermal Wave Field in the turbulent transport regime. (a) Amplitude (b) Phase.

The results show that the thermal wave field is accurately sampled by V_f over the radial range investigated and the cross-field structure is highly complex. The classical case in Fig. 4.19 is the simplest and already it is abundantly clear that the homogeneous model used in the axial experiments is not suitable for describing the wave field outside the center of the filament. To more easily visualize this thermal wave field the one-dimensional line cuts are shown in Fig 4.23. In general, the amplitude decreases with increasing frequency and decreases further from the center of the filament. However, the most obvious feature in the amplitude is the local minimum seen in the middle of the plane that varies in frequency at each radius from approximately 2 mm to 4.5 mm. The minimum has a corresponding feature in the phase where the wave field rapidly transitions in phase. There are rapid phase variations, when moving the probe by only 0.05 cm or increasing the frequency by 1 kHz, by up to $\pm\pi$ ($\pm$180 degrees); we note that there are also shifts by up to 2π but these transitions are closer in cyclical phase. The 7 kHz V_f fluctuations shown in Fig. 4.17 illustrate how the phase shift is manifested; the oscillation begins at nearly the same time at $r = 0$ mm and $r = 8$ mm but the instantaneous phase of the $r = 8$ mm oscillation leads the phase of the $r = 0$ mm pulse. This is a signature of thermal waves that sets them apart from conventional travelling waves. Interestingly, the sharp phase transitions are not removed by simply unwrapping the phase periodically along one dimension. Rather, there is a gradual shift in the phase on either side of the feature when sweeping in f or r that becomes larger closer to the amplitude minimum; unwrapping the phase along one dimension would only result in larger discontinuities in the other. These amplitude and phase interference phenomena are features indicative of an inhomogeneous thermal conductivity profile [49].

The wave field during the phase where the drift-Alfvén waves start to develop is shown in Fig. 4.20. This case is not much different than the first case and supports

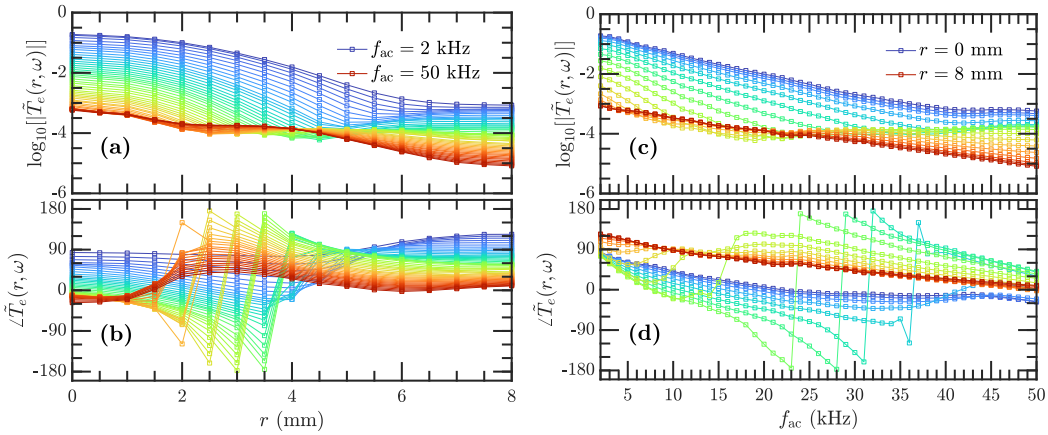

Figure 4.23: Thermal wave field in the classical regime. (a) and (b) are the amplitude and phase, respectively, with r on the horizontal. (c) and (d) are the amplitude and phase, respectively, with f on the horizontal. The data are the same as in Fig. 4.19 with the phase in degrees.

the earlier conclusion that the waves are not yet enhancing the cross-field transport significantly. There is evidence of both the thermal resonances observed earlier in the axial experiments with corresponding features in the phase. In Fig. 4.21 we observe that once the drift-Alfvén waves are within the frequency range investigated there is clear coupling to the drift wave and the thermal wave field can be used to image it. The earlier supposed coupling in the axial experiments is supported by this result. The turbulent case in Fig. 4.22 has nearly no evidence of the drift wave, similar to the Fourier spectrum, but the measurement shows more variation that is likely due to the large intermittent transport events disrupting the thermal wave oscillations.

The enhanced cross-field transport is manifest in the wave field by the shape of the amplitude decay and rate of the phase shift. Thermal wave theory predicts that higher frequency waves will experience a higher rate of spatial attenuation in the amplitude and spatial shift in the phase. However, in the turbulent and transition cases, the thermal wave field is observed to have nearly identical radial amplitude decay and phase shift rate for all frequencies above approximately $f_{ac} = 15\,\text{kHz}$.

This represents a deviation of the thermal wave field from the prediction of classical transport where it is known that the transport is anomalous. The results presented here suggest that thermal waves can be used to image the plasma and distinguish between different transport regimes.

4.2.3 Application of Inhomogeneous Model

In this section we apply the inhomogeneous model presented in Section 3.3 to the thermal wave field in the classical case. The model at this stage is only in one dimension and must be used in the axial direction by treating each of the radial positions as if the source is located at that radius but 190 cm away; this is a reasonable approximation given the dimensions of the filament. To treat it as a one-dimensional radial problem to measure the cross-field transport coefficients would require treating the source as if it were at ($r = 0$ cm, $z = 190$ cm), which is not an appropriate way to model the experiment. The results of fitting the model to the thermal wave field at $r = 0.1$ cm, $r = 0.2$ cm, $r = 0.3$ cm, and $r = 0.5$ cm are shown in Figs. 4.24, 4.25, 4.26, and 4.27, respectively. The experimental data is normalized to the measurement at $f = 2$ kHz and the phase is unwrapped along the frequency dimension.

The fits are performed by varying $\alpha_{\parallel_\infty}$, $\alpha_{\parallel_0}$, and λ in the exponential profile described in Eq. (3.55); the numerical values of the parameters are informed by the experiment range and are reasonable estimations. The objective here is not to extract the transport coefficients but to qualitatively assess the model. At each radius investigated there is a significant deviation of the fit from the experimental data. However, the ability of the model to reproduce the detailed features of the thermal wave field is undisputed. With a high degree of certainty, we can say that the amplitude minima and phase discontinuities are a result of the inhomogeneous plasma temperature and density profiles. The model can be applied to the other cases with varying degrees of

success and is particularly poor at describing the turbulent phase where the amplitude and phase do not behave as expected even along the frequency dimension. The thermal resonances in Fig. 4.20 are still not described by this model and the ability to accurately model these features remains elusive. The current formulation offers no mechanism for coupling to the drift-Alfvén wave observed in Fig. 4.21 and cannot reproduce this feature.

There are several issues with the current comparison of the model that we discuss here. First, cross-field transport is neglected and it should be obvious by now that this is inherently a multi-dimensional problem. The steps towards such a model are described in Section 3.3 and completion of this extension is outside the scope of this thesis. Second, the one-dimensional model additionally neglects the variation in $\kappa_\parallel$ along the radial direction. There is no reason to believe that the features of the thermal wave field are described solely by the axial variation in $\kappa_\parallel$. There is a two-dimensional inhomogeneous profile for both the parallel and transverse transport coefficients that need to be accounted for. Third, the inhomogeneous profile of the thermal diffusivity considered here is exponential; while this does a reasonable job of reproducing the main features of the experiment, the model could be improved by considering a profile that more closely matches the experiment. The profiles in the density and temperature each contribute to the perpendicular and parallel diffusivity profiles and experiment measurements and transport simulations can be used to estimate the two-dimensional profiles. Last, the model neglects advection by the plasma and there are both axial and radial flows in the experiment; it is presently unclear how these may impact the thermal wave field. It should be noted that the addition of an inhomogeneous vector velocity field to the Hamilton-Jacobi formulation is a formidable task.

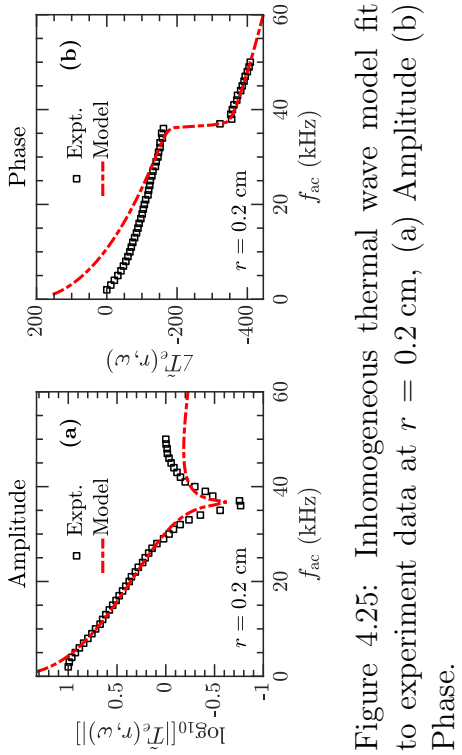

Figure 4.24: Inhomogeneous thermal wave model fit to experiment data at $r = 0.1$ cm, (a) Amplitude (b) Phase.

Figure 4.25: Inhomogeneous thermal wave model fit to experiment data at $r = 0.2$ cm, (a) Amplitude (b) Phase.

Figure 4.26: Inhomogeneous thermal wave model fit to experiment data at $r = 0.3$ cm, (a) Amplitude (b) Phase.

Figure 4.27: Inhomogeneous thermal wave model fit to experiment data at $r = 0.5$ cm, (a) Amplitude (b) Phase.

CHAPTER 5.

Multi-Filament Experiments

In this chapter, we present results from the experiments investigating the interactions between multiple magnetized pressure filaments. In Section 5.1 the scale length of interaction is established and the evolution of the filaments in a tight bundle is analyzed in detail; including a comparison of the space potential profile with that predicted by an emissive cathode model, and a comparison of the observed wave modes with a linear stability analysis for drift-Alfvén modes. The tight filamentary bundle exhibits highly turbulent and intermittent fluctuations and these are investigated further in Section 5.2 using several time series analysis techniques including the amplitude probability density function, conditional averaging, the complexity-entropy plane, and the Hurst exponent. Last, in Section 5.3 the preliminary results from modulating one of the sources in the tight filament bundle are presented; the main result is that the non-axisymmetric driving allows coupling to the non-zero azimuthal mode numbers of the drift-Alfvén waves. In these experiments the probes are set up according to the schematic in Fig. 2.6(a), unless otherwise specified. Here, $z_1 = 256$ cm, $z_2 = 544$ cm, and reference probes are placed at $z_R = 320$ cm. Rogowski coils and voltage sensors are measuring the current and voltage, respectively, on each of the cathode sources.

5.1 Filament Interactions and Wave Growth

Two different inter-crystal distances are presented here; a close separation where the distance of the cathodes from a central origin is adjusted to be ∼5 mm, and a far

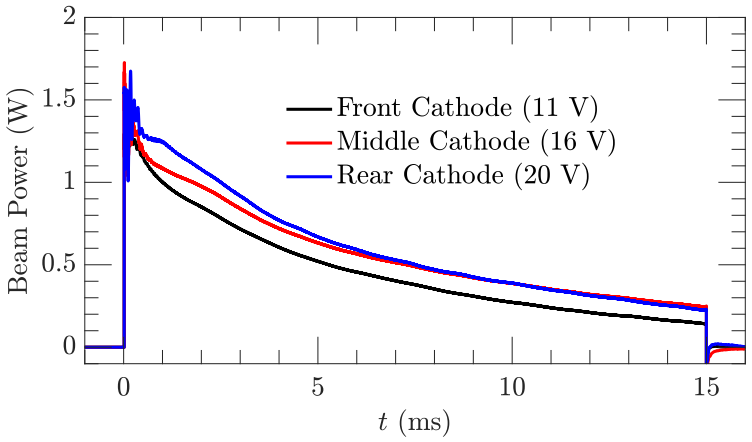

Figure 5.1: Beam power for each CeB_6 crystal cathode when in the close separation configuation.

separation where the distance from the origin is ∼15 mm. In this set of experiments, all measurements are taken at z_1 and no probe was placed at z_2. For the far separation, the discharge bias on each cathode is equal at 15 V, resulting in nearly identical plasma discharge currents for each crystal. In the close separation, equal biases on each cathode resulted in different discharge currents due to a shadowing effect by the forward cathodes on those staggered to the rear (Fig. 2.6(b)). To remedy the uneven beam power, voltages of 11, 16, and 20 V were used for the front, middle and rear crystals, respectively; Fig. 5.1 shows the beam power over time for the close separation configuration. It is clear that in adjusting the voltages a nearly uniform beam power was achieved across each of the cathodes. Performing this power matching step is necessary to ensure similar heating of the plasma from each cathode.

5.1.1 Evolution

Fig. 5.2 shows probe measurements in a transverse plane located at $z_1 = 256$ cm from the cathode sources, taken shortly after the cathode bias is applied (∼0.1 ms). Fig. 5.2(a) is a plane of ion saturation current for the far separation and shows the filaments each maintain a distinct structure but develop convective tails indicating an

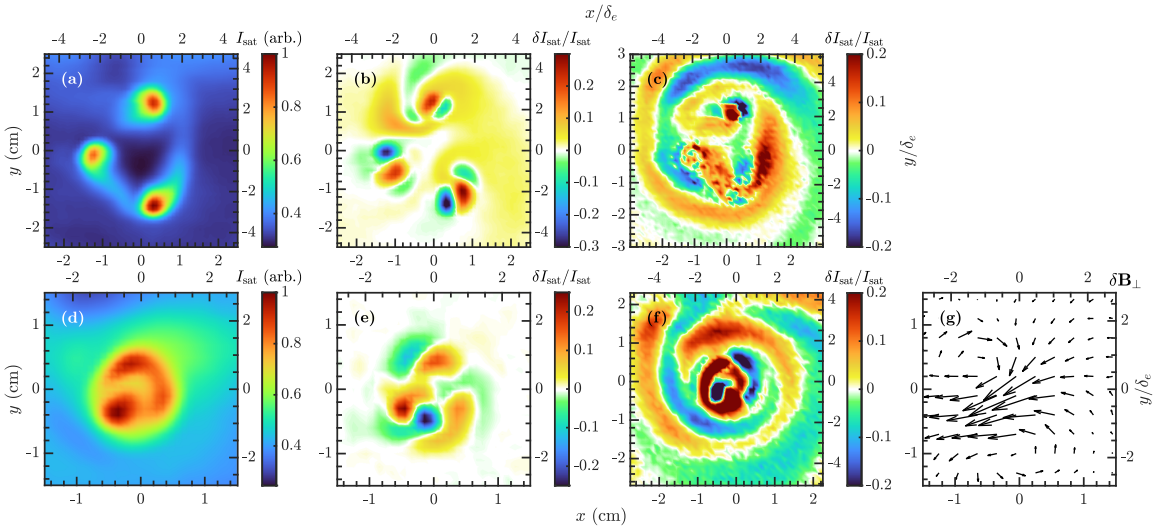

Figure 5.2: Probe measurements for different arrangements of the filaments just after turning on, $t = 0.1$ ms. (a) I_{sat} for the filaments in far proximity. (b) Filtered fluctuation levels in (a) at ∼25 kHz. (c) Filtered fluctuation levels in (a) below 5 kHz. (d) I_{sat} when the filaments are positioned close together. (e) Filtered fluctuation levels for (d) at ∼20 kHz. (f) Filtered fluctuation levels for (d) below 5 kHz. (g) Unfiltered magnetic fluctuations, $\delta\mathbf{B}_\perp$, showing a dipole rotating at ∼25 kHz.

interaction between the filaments. Fig. 5.2(b) shows the same plane of fluctuations in the ion saturation current, δI_{sat}, bandpass filtered around 25 kHz (5 kHz width). There is evidence of distinct mode structures on each of the filaments with fluctuation levels around $\delta I_{sat}/I_{sat} \approx 20\%$, with lower fluctuation levels between the filaments ($\delta I_{sat}/I_{sat} \approx$ 5-10%). The frequency of 25 kHz and similarity in structure to previous single filament experiments indicates each filament rapidly develops drift-Alfvén wave fluctuations [15, 19]. The formation of the tails may be due to transverse $\mathbf{E} \times \mathbf{B}$ flows generated by radial electric fields directed toward the center of each filament or through enhanced cross-field transport due to interaction between the drift-Alfvén modes.

In the close separation, all three filaments have appeared by 0.1 ms (Fig. 5.2(d)). The filaments are initially highly active spatially and distorted before settling into

stable positions in a triangular configuration with overlapping gradients by ∼0.5 ms. Before the appearance of all three filaments there is first only a single filamentary structure that eventually settles in the position of the front cathode (bottom left); fluctuations in ion saturation current show a strong ($\delta I_{\rm sat}/I_{\rm sat} \approx 30\%$) $m = 1$ fluctuation around this single filament at ∼25 kHz, indicating that before the setup of the other two filaments this single filament is behaving as a mostly independent filament like the separated filaments in Fig. 5.2(a) and previous single filament experiments. A plane of $\delta I_{\rm sat}$ at $t = 0.1$ ms and bandpass filtered around 20 kHz (5 kHz width) is shown in Fig. 5.2(e). The 20 kHz fluctuations show a pattern with an $m = 3$ azimuthal mode number rotating in the direction of the electron diamagnetic drift (counter-clockwise in Fig. 5.2(e)). The structure appears to be a global mode centered on all three filaments that persists throughout the discharge and will be analysed further in this manuscript.

Fig. 5.2(g) shows unfiltered magnetic fluctuations ($\delta \mathbf{B}_\perp < 0.5$ mG) that indicate a dipole structure that rotates at a frequency of 25 kHz. A similar magnetic structure was observed in the single filament case in conjunction with an $m = 1$ drift-Alfvén wave and physically represents two opposing current channels in the axial direction that rotate around the filament structure [15]. Of particular interest is that the dipole is centered on the bottom left filament, the front-most cathode, which initially shows the strongest heating and the frequency matches the frequency of the drift-Alfvén waves observed on the separated filaments (Fig. 5.2(b)) and the initial $m = 1$ structure before the two other filaments appear. Beyond ∼0.1 ms the magnetic dipole like structure develops a less dominant but more complex magnetic structure with evidence of several more alternating current channels with a rotation centered on the full tri-filament structure at a slightly lower frequency of ∼20 kHz, the same as the $m = 3$ pattern in Fig. 5.2(b). This situation during the initial turn-on can be

interpreted as the bottom left filament developing a drift-Alfvén wave independent of the other two filaments and then the heated region from all three filaments develops the $m = 3$ mode with magnetic fluctuations of a lower magnitude than the dipole structure from the $m = 1$ mode.

In addition to the drift-Alfvén fluctuations that appear shortly after the bias is applied, there are short-lived, low frequency (<5 kHz) fluctuations in a tornado-like spiral pattern with a radial extent of several centimetres – similar to that seen in a ring-shaped cathode experiment in the LAPD [94]. This is shown in Figs. 5.2(c) and 5.2(f) where δI_{sat} is low-pass filtered below 5 kHz; note that the size of the planes are larger than in Fig. 5.2(a,b) and (a,b), respectively, and that the spiral arms clearly extend beyond the full data collection plane indicating extensive cross-field transport well-beyond the heated region with fluctuation levels of ∼10%; in contrast, the ring-shaped cathode experiment observed fluctuations on the order of ∼30%. It has been suggested [94] that the tornado-like mode is due to vorticity in the plasma generated by the emissive-cathode boundaries. The tornado structure in the far separation case (5.2(c)) initially shows tornado-like development around each filament and progresses to a structure surrounding all three filaments; in contrast, the close separation case (5.2(f)) shows a single tornado structure developing around the bundle. The tornado structure has a significant radial extent and it is reasonable to wonder if it may be a characteristic of the afterglow plasma; however, it is not present in discharges until the bias is applied to the crystal cathodes. Furthermore, the individual tornado arms around the separated filaments in Figs. 5.2(c) indicate it clearly develops from the emissive-cathodes. In this manuscript, the main focus is on an analysis of the close separation configuration once the filaments reach a stable configuration, i.e. beyond ∼0.5 ms where the transient tornado-like mode is not present.

The electron temperature, T_e, density, n, and space (plasma) potential, V_s, can

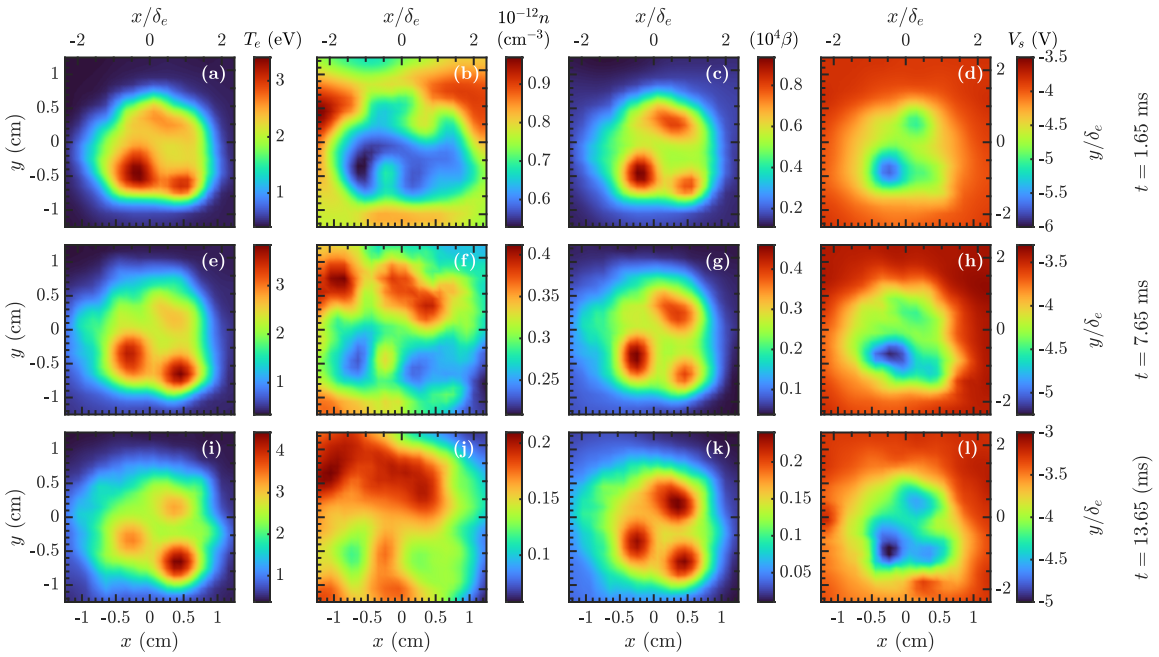

Figure 5.3: Temperature (a,e,i), density (b,f,j), electon plasma beta (c,g,k), and space (plasma) potential (d,h,l) for three different times during the evolution of the 3 filament structure. The data was acquired using rapidly swept Langmuir probes at a distance $z_1 = 256$ cm from the most foreward source.

be determined by rapidly sweeping (400 μs) the probe bias to collect characteristic Langmuir I-V curves. A standard analysis of the I-V curves yields the parameters of interest [68, 69]. While this method does not deliver high time resolution and has an element of uncertainty due to fluctuations in the parameters during the sweep, the long-term evolution of the parameters can be determined. Fig. 5.3 shows planes of, T_e, n, β, and V_s for $t = 1.65$, 7.65, and 13.65 ms, highlighting the start, middle, and end of a 15 ms discharge when the filaments are in the close separation. Here, the electron plasma β is determined using $\beta = 8\pi n T_e/B_o^2$ and is proportional to the electron plasma pressure. Initially, the density is slightly non-uniform with a decrease in the regions of highest temperature; this is in stark contrast to previously documented single filament behaviour that shows enhanced density in the center of

the filament [75]. By the middle of the discharge, any large spatial differences in density have disappeared and by the end of the experiment, the variations in density are minimal (note the range of the colour bar). Recall that the background density decays substantially during this time frame due to plasma outflows to the axial ends of the machine.

The locations of the temperature filaments remain stationary and the filaments become more uniform as the experiment progresses. The temperature of the filaments increases from around 3 eV to around 4 eV. The pressure profile remains largely unchanged qualitatively, with three distinct pressure filaments visible throughout the experiment; however, the absolute pressure is dropping due to the continued decrease of plasma density. The space potential forms a well where the cathodes are located, as expected from similar experiments [70, 92], but has a noticeable asymmetry in the magnitude with the bottom left filament having a significantly lower space potential in Fig. 5.3(d). Referring to Fig. 2.6(b), the bottom left cathode is the front-most cathode and it is likely the probe and crystal are shadowing the potential from the other cathodes. Towards the end of the experiment, the shadowing effect is reduced, perhaps due to the decreased plasma density and reduced plasma conductivities. In all of the temperature, pressure, and potential the individual filament gradients are overlapped and produce a global gradient structure around the tri-filament bundle.

Fig. 5.4(a) shows a time trace for single shot of fluctuations in ion saturation current collected on the outer gradient of the tri-filament bundle. The fluctuations are broadband with very little evidence of coherent wave activity and the shot has a high degree of temporal uniformity. This temporal consistency is in contrast to the single filament situation where the filament transitions through several different transport regimes with fluctuations exhibiting a coherent phase followed by steady broadband perturbations [15, 16, 19]. A frequency analysis of the 3 ms long shaded region in

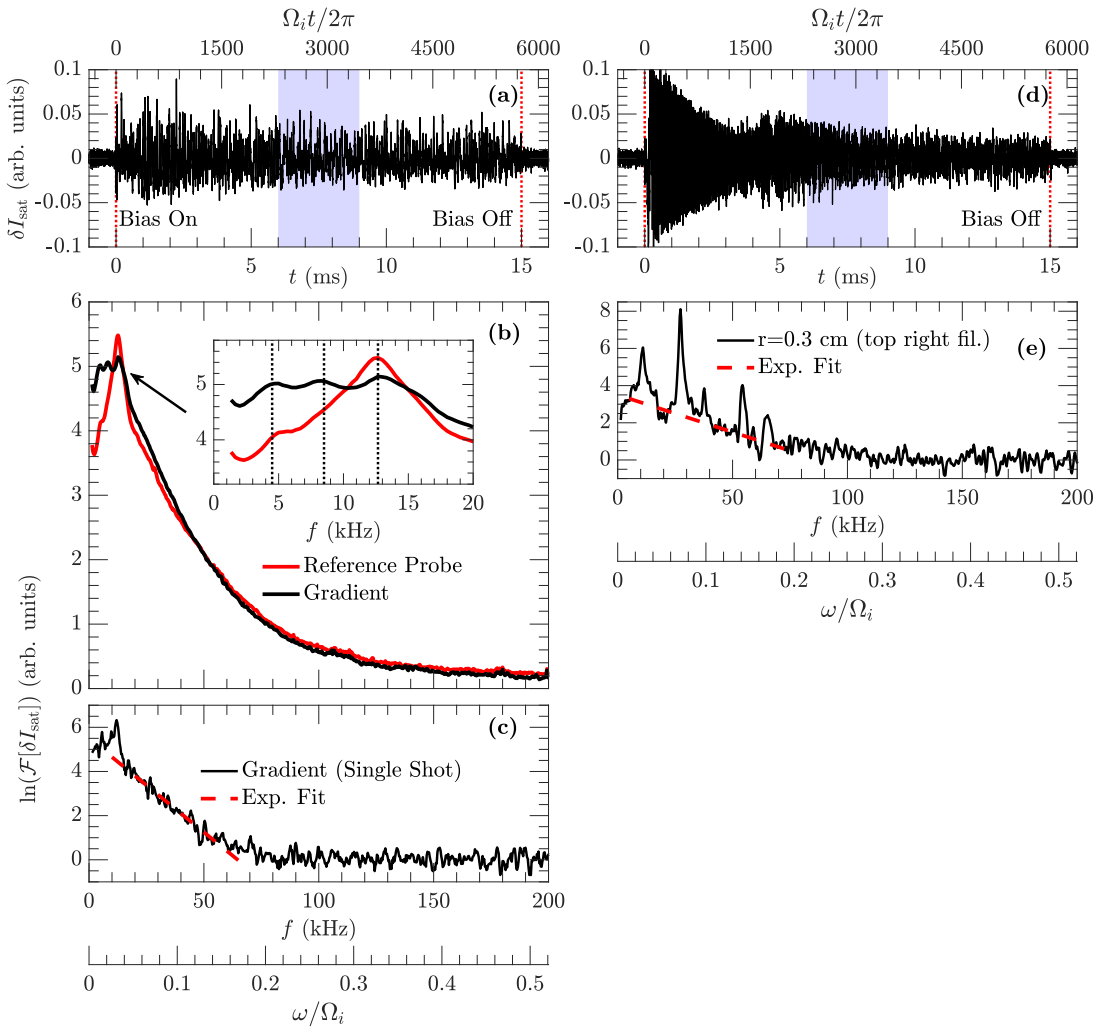

Figure 5.4: (a) Time series of δI_{sat} for a single shot at a radius of $r = 1$ cm from the approximate center of the close separation triangular filament configuration. (b) Ensemble average of the power spectra of the shaded region in (a) for all shots with a radius of $r = 1$ cm from the moving probe (black) and the reference probe at a stationary position on the outer gradient (red). (c) Power spectrum of a single shot (panel (a)) demonstrating the exponential decay of the power spectrum. (d) Time series of δI_{sat} for a single shot at a radius of $r = 0.3$ cm from the approximate center of the top right filament in the far separation configuration. (e) Power spectrum of a single shot (panel (d)) similar to previously reported single filament spectra, establishing the filaments behave mostly indepentently in the far separation.

Fig. 5.4(a) is shown in Fig. 5.4(b) for an ensemble of plasma shots all falling at a radius of $r = 1$ cm from the approximate center of the filament bundle; the power spectrum of the afterglow plasma in the absence of heating has been subtracted. The gradient region has sharply decaying broadband fluctuations for frequencies below $\sim$150 kHz. In addition, the spectrum of a reference probe placed further down the device is also shown in Fig. 5.4(b). The reference probe was manually placed without a probe drive, thus its exact location in the plane is unknown, to position it on the outer gradient of one of the filaments. The comparison of the frequency analysis of the reference probe signal and the gradient region supports the placement of the reference probe. Fig. 5.4(c) shows the power spectrum of a single shot on the gradient; this highlights the exponential nature of the broadband fluctuations that become obscured by the ensemble average due to slightly varying exponential time constants. A similar exponential frequency decay has been extensively studied during a portion of the single filament evolution [19, 20]; it was demonstrated that the exponential spectrum is caused by Lorentzian shaped pulses in the time series, and a complexity-entropy analysis [22] revealed the transport dynamics in this regime are chaotic. Additionally, there is some evidence of skewness in the amplitude distribution of the shot in Fig. 5.4(a); skewed distributions have been associated with anomalous cross-field transport in similar experiments involving drift waves and pressure gradients [51, 55]. An analysis of the time series for these tri-filament experiments is presented in Section 5.2 to determine if the exponential frequency decay is due to similar Lorentzian pulses, if the transport dynamics are also chaotic, and the nature of the skewed amplitude distribution.

In the inset of Fig. 5.4(b) there is a deviation from the exponentially decaying power spectrum below $\sim$20 kHz. Three distinct peaks occur in the power spectrum at 4.5 kHz, 8.5 kHz and 12.75 kHz. The mode structures for these frequencies can

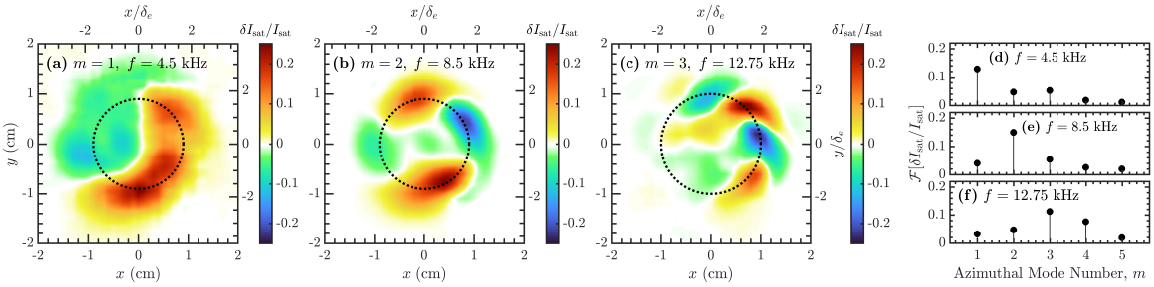

Figure 5.5: Mode structures for the three peaks observed in the power spectra on the outer gradient, indicated by dashed lines in the inset of Fig. 5.4(b). (a) $m = 1$ mode at 4.5 kHz. (b) $m = 2$ mode at 8.5 kHz. (c) $m = 3$ mode at 12.75 kHz. The black dashed lines indicate the radius where the mode structures are peaked. (d,e,f) Azimuthal mode decomposition for each of (a,b,c), respectively.

be obtained using cross-correlation techniques between signals from the moving and reference probe, shown in Figs. 5.5(a,b,c). This reveals that the modes have dominant azimuthal mode numbers of $m = 1$, 2, and 3. The amplitude is peaked on the outer gradient of the filaments and the modes have a striking azimuthal symmetry despite the asymmetric heating configuration. During the early stages of the plasma discharge (0-3 ms) these same global modes are present but with higher frequencies at around 7 kHz, 14 kHz, and 20 kHz – indicating the $m = 3$ mode from Fig. 5.2(d) maintains itself throughout the discharge while dropping in frequency. Towards the end of the discharge (12-15 ms) the same three modes are present and there is very little change in the frequencies from the middle of the discharge. Figs. 5.5(d,e,f) show the azimuthal mode decomposition using spatial Fourier analysis of Figs. 5.5(a,b,c), respectively, and confirm the visual conclusion of the dominant mode numbers at each frequency, but additionally show there is significant power contained in other mode numbers; the observation of mixed mode numbers is similar to other drift wave experiments in cylindrical geometries and may indicate non-linear coupling between the wave modes [55, 56].

To establish that there is no global mode present when the filaments are sufficiently

separated a time trace from the gradient of one of the filaments from the far separation is shown in Fig. 5.4(d). The time trace shows the rapid development of a drift wave at 25 kHz (as shown on each filament in Fig. 5.2(b)) that decreases in amplitude before the filament transitions to a more turbulent phase [19];. The single-shot spectrum displayed in Fig. 5.4(e) shows the highlighted 3 ms section of the time from Fig. 5.4(d). Evident is the thermal wave (10 kHz), drift-Alfvén wave and harmonic, sidebands from modulation of the drift-Alfvén waves by the thermal wave, and a baseline exponential frequency spectrum from Lorentzian shaped solitary pulses. This spectrum can be directly compared with previous work on single filaments [15, 16, 19] to conclude that the tri-filaments in the far separation are dominantly behaving as independent single filaments.

To better understand how the outer gradient is supporting these modes the temperature, density, and pressure are first interpolated to a polar grid with the origin selected to be the center of the filament configuration. To investigate the azimuthal symmetry of the outer temperature gradient an average of 15° azimuthal averages through each filament is compared with an average of 15° azimuthal averages between each filament and the the full azimuthal average of the configuration, shown in Fig. 5.6(a) for the $t = 7.65$ ms temperature profile (Fig. 5.3(e)). As expected, the asymmetric heating configuration causes a flattop-like profile between the filaments and a profile peaked at $\sim$5 mm where the filaments are located. However, the gradient region beyond $\sim$7 mm shows more consistency between the full azimuthal average, the filaments, and gaps between them. Fig. 5.6(b) shows the full azimuthal averages of the pressure, temperature, and density for the time $t = 1.65$ ms (top row, Fig. 5.3) where the density is most varied; the values are normalized to the edge of the data collection plane. In both Figs. 5.6(a) and (b) the shaded region indicates the the standard deviation in the azimuthal average. It is apparent that the gradient

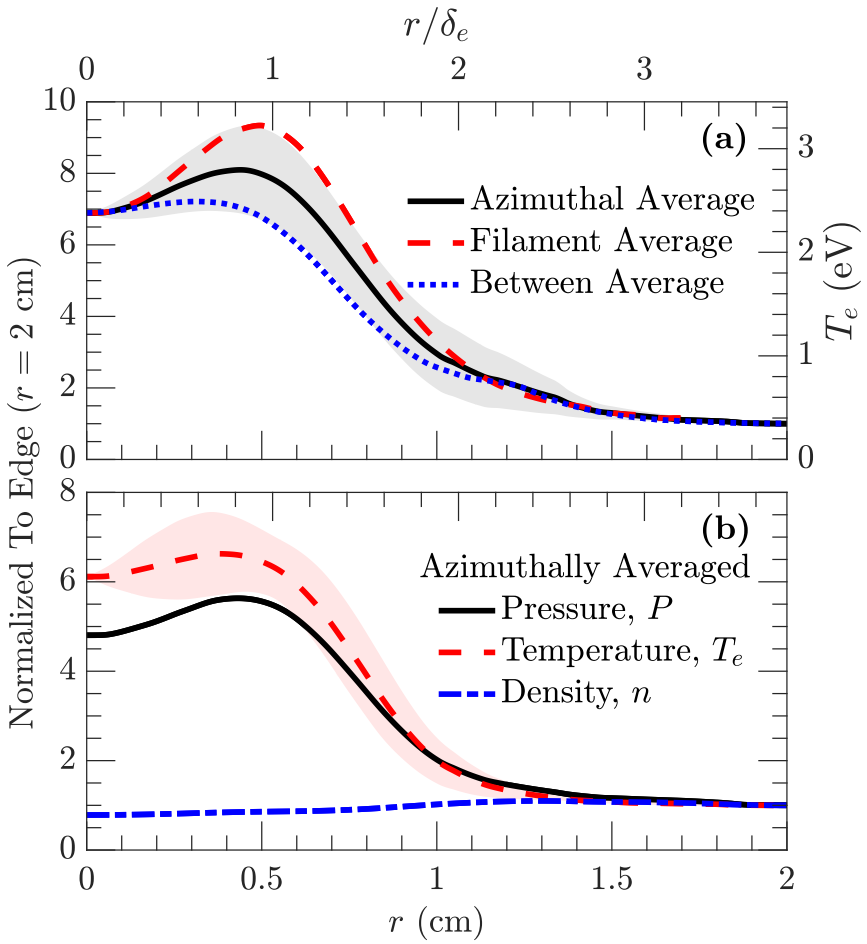

Figure 5.6: (a)Temperature profiles at $t = 7.65$ ms for radial cuts through the filaments (dashed red), between filaments (dotted blue), and the full azimuthal average (solid black). The standard deviation of the azimuthal average is given by the grey shaded region. (b) Azimuthal averages at $t = 1.65$ ms of the pressure, P (solid black), temperature, T_e (dashed red), and density, n (dash-dotted blue). The curves are normalized to their values at the edge of the three filament structure. The standard deviation in the temperature average is shown by the red shaded region, the pressure standard deviation is similar, while the standard deviation in density is comparatively negligible.

driving the modes is the temperature gradient and not the density gradient; and, the quasi-symmetry of the outer gradient suggests treating the problem of stability of the profile to wave growth in only one dimension, namely, the radial component.

The average radial temperature profile in Fig 5.6(a) is accurately described by the empirical equation,

$$T_e(r) = C_1 + C_2 e^{-C_3(r-C_4)^2} + C_5(r + 1.5\text{ cm})^{-4} \tag{5.1}$$

where, $C_1 = 0.353$ eV, $C_2 = 1.957$ eV, $C_3 = 3.680$ cm^{-2}, $C_4 = 0.469$ cm, $C_5 = 6.753$ eV $\cdot$ cm^4.

5.1.2 Azimuthal Flows and Cathode Model

The swept Langmuir probe measurements of the plasma potential allow a characterization of the transverse $\mathbf{E} \times \mathbf{B}$ flows generated by the well in the plasma potential at the center of the filaments. Fig. 5.7(a) shows the pressure at $t = 7.65$ ms with the $\mathbf{E} \times \mathbf{B}$ flow arrows superimposed on top. The largest flows are concentrated on the outer gradient with some convective mixing in the center region. Performing the same interpolation to a polar grid as was done for T_e, n, and P the azimuthal average can be calculated and is shown by the black circles in Fig. 5.7(b). The black dashed line shows an approximate fit to the data given by,

$$V_s(r) = C_1 + C_2 e^{-C_3(r-C_4)^2} + C_5(r + 3\text{ cm})^{-4} \tag{5.2}$$

where, $C_1 = -3.309$ V, $C_2 = -0.690$ V, $C_3 = 5.712$ cm^{-2}, $C_4 = 0.397$ cm, $C_5 = -75.410$ eV $\cdot$ cm^4. The azimuthal average of the $\mathbf{E} \times \mathbf{B}$ flows, u_θ, and a calculation from Eq. (5.2) is shown by the blue triangles and dashed blue line, respectively. The flow peaks at around 2×10^5 cm/s just outside the filament centers at $\sim$7 mm and is nearly zero beyond $\sim$1 cm. The flow shear is defined as [70],

$$\gamma_s = r\frac{\partial}{\partial r}\left(\frac{u_\theta(r)}{r}\right) \tag{5.3}$$

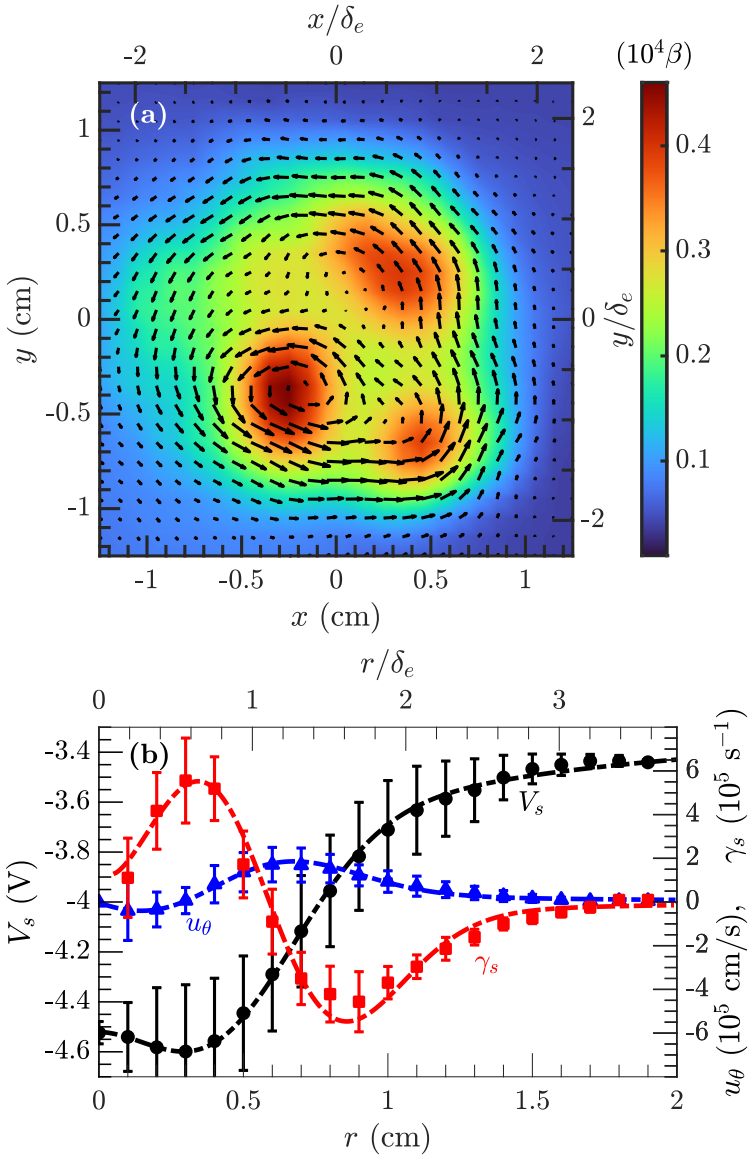

Figure 5.7: (a) Electron plasma beta plane at $t = 7.65$ ms with arrows indicating direction and magnitude of $\mathbf{E} \times \mathbf{B}$ flows. (b) Azimuthal average of the radial structure of the plasma potential (left axis), azimuthal $\mathbf{E} \times \mathbf{B}$ flow velocity (right axis), and azimuthal flow shear (right axis). The error bars indicate the standard deviation of the azimuthal averaging.

The azimuthal average of the flow shear is shown by the red squares in Fig. 5.7(b) and the calculation from (5.2) is shown by the dashed red line. The shear has opposite extrema on the inner (3 mm) and outer (9 mm) gradients of the filaments with magnitudes of 5×10^5 s^{-1}. Shear flow is known to aid in the suppression of instabilities and turbulence [95] and is a significant feature of the filamentary structure in both single and multi-filament configurations; despite this, the shear has not previously been considered in the stability of the filamentary gradient to drift-Alfvén modes.

The observed sheared flow observed in the $\mathbf{E} \times \mathbf{B}$ flow is generated by the plasma potential profile. In a previous set of publications [72, 92], a predictive analytical model for the operation of an emissive cathode in the LAPD afterglow was developed and tested. Here, an adaptation of that model is used to approximate the three-dimensional current system and associated plasma potential generated by the three-cathode arrangement. The derivation of this model was completed by Dr. Matt Poulos of our research group and is outside the scope of this thesis. In the model, the steady-state perpendicular and parallel currents are expressed in terms of a scalar plasma potential V_s. A good approximation for the plasma potential formed by the three-cathode arrangement is obtained by superimposing three copies of the analytical solution for the single filament case [72, Eq. (14)]. In general, if $V_{s1}(r, z)$ is the azimuthally symmetric plasma potential for the single filament case, the plasma potential for multiple filaments located at (x_k, y_k), can be approximated as

$$V_s(x, y, z) = \sum_k V_{s1}\left(\sqrt{(x - x_k)^2 + (y - y_k)^2}, z\right). \tag{5.4}$$

The results of this model are presented in Fig. 5.8(a), which shows the predicted potential profile and $\mathbf{E} \times \mathbf{B}$ flows. A comparison of the azimuthal average of the predicted and measured potential profiles is shown in Fig. 5.8(b); the model accurately

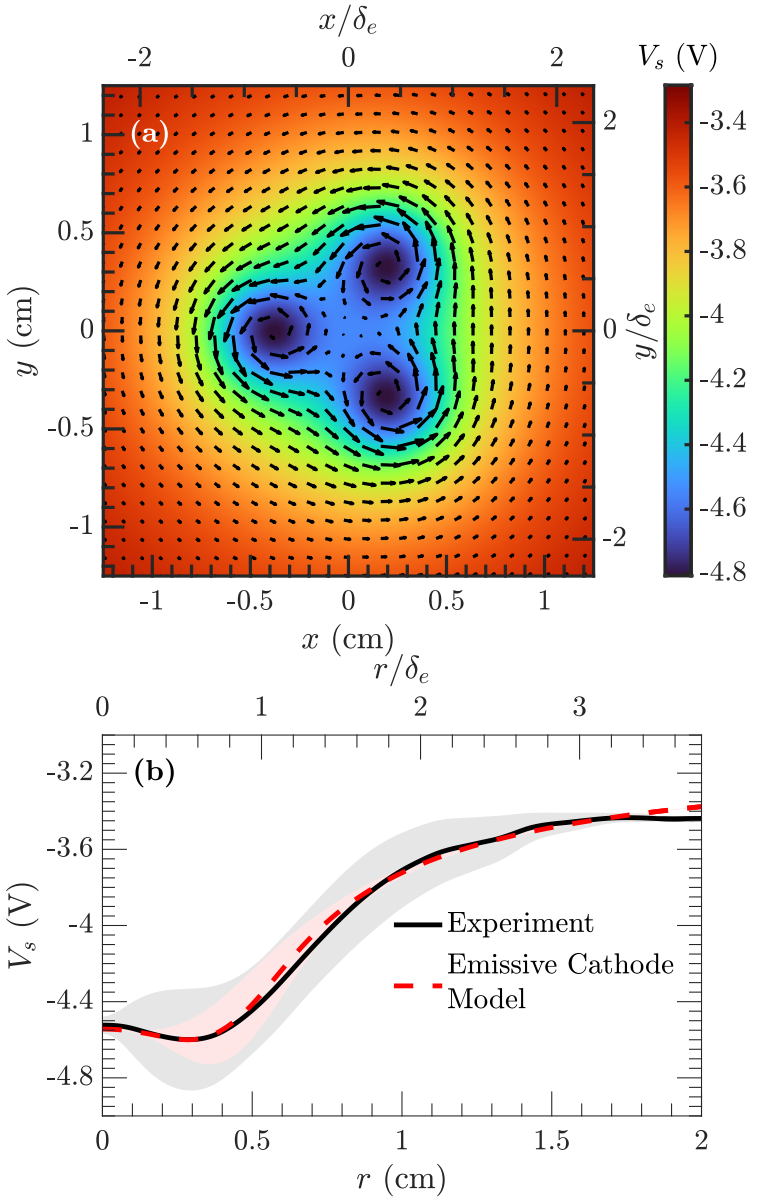

Figure 5.8: (a)Prediction of plasma potential and $\mathbf{E} \times \mathbf{B}$ flows using the emissive cathode model. (b) The azimuthally averaged potential profile for the model prediction (red dashed) and experiment (solid black). The standard azimuthal standard deviation is indicated by shaded regions in red and gray for the model and experiment, respectively.

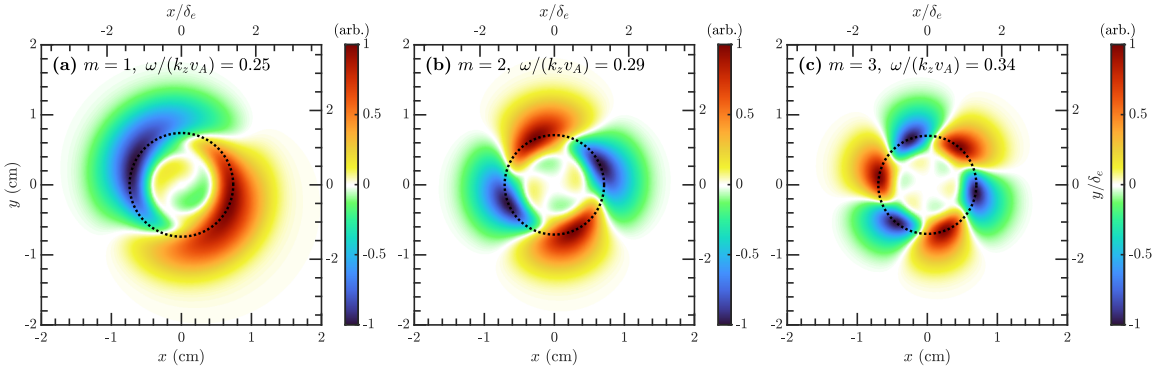

Figure 5.9: Predicted 2D mode structures for (a) $m = 1$, (b) $m = 2$, and (c) $m = 3$. The real part of the parallel electric field is displayed and black lines indicate where the mode structures are peaked radially. k_z and v_A refer to the axial wave number and Alfvén speed, respectively (see [73]).

predicts the experimental profile, and is strong evidence that the observed transverse flows and shear can be attributed to the emissive sheath boundary.

5.1.3 Linear Stability Analysis

In this section, a stability analysis of the one-dimensional radial profiles is used to describe the quasi-axisymmetric modes observed on the outer gradient of the tri-filament structure. The derivation of the linear stability of drift-Alfvén modes is available in our publication [73] and not provided herein detail; it is again largely the work of Dr. Matt Poulos and outside the scope of this thesis. The methodology followed is similar to that used to analyze the stability of the single filament gradients [21, 96] with the addition of azimuthally sheared flows accounted for by the radial potential. While the tri-filament configuration is not azimuthally symmetric the quasi-symmetry of the observed modes and outer gradient just described significantly reduces the complexity of the model to one dimension. In short, a system of eigenvalue equations is obtained that describes the stability of the electromagnetic fields to linear drift-Alfvén wave perturbations; the inputs to the model are the temperature, density, and space potential profiles. The eigenvalue solutions and

corresponding eigenmodes represent the complex frequencies and radial structure of the stable and unstable drift-Alfvén waves. Two solution regimes are investigated, a collisionless regime and an approximation to a collisional regime.

The analysis is conducted using the empirically derived one-dimensional radial profiles of the temperature and potential, given in Eq. (5.1) and Eq. (5.2), respectively. Fig. 5.9 shows collisional predictions of the two-dimensional mode structures that are obtained from the parallel electric field for $m = 1$, 2, and 3, which can be compared with Fig. 5.5. A more detailed comparison is shown in Fig. (5.10)(a-c) for each of modes $m = 1$, 2, and 3, respectively. The experimental temperature profile and Eq. (5.1) are shown in black, the experimental flow profile and Eq. (5.2) are shown in blue, and the experimental and predicted mode profiles of ion saturation current are shown in red. For each of the observed modes, both the peak location and shape are accurately predicted by the linear eigenmode analysis, however, there is some deviation possibly due to nonlinear effects discussed in the next section.

Figure 5.10(d) compares the frequencies and growth rates predicted by the linear analysis in the collisional and collisionless regimes with the observed frequencies in the experiment. The results demonstrate that there are severe limitations to the collisionless approximation. In the experiment, the observed frequency increases with azimuthal mode number; however, the collisionless linear analysis predicts a decreasing frequency with increasing m. Additionally, the $m = 1$ eigenmode is predicted to have a negative growth rate where the mode has a positive growth rate in the experiment. In contrast, the collisional approximation reproduces the observed trend in experimental frequencies and further yields positive growth rates for each of the modes. When the shear flow is neglected in the eigenmode solver the global eigenmode frequency is decreased by $\sim$20% while the growth rate is increased by approximately

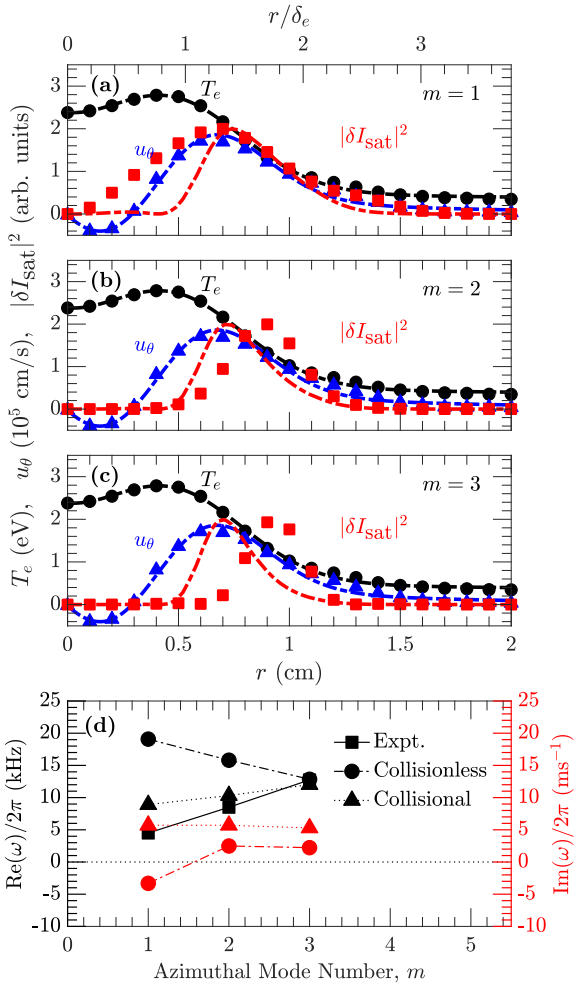

Figure 5.10: Comparison of experimental radial mode structures with predictions of the collisional linear stability analysis (LSA). (a-c) Temperature in black (eV), $\mathbf{E} \times \mathbf{B}$ flow in blue (10^5 cm/s), and radial mode structures in red (arb. units) for $m = 1, 2,$ and 3 in (a), (b), and (c), respectively. The markers indicate the experimental observations and the solid lines represent inputs (temperature and flow) and output (mode structure) of the LSA. (d) The experimentally observed frequencies are indicated by the black squares, the predicted frequency in the collisionless regime by black circles, the predicted frequency in the collisional case by black triangles, and the growth rates in the collisionless and collisional cases by red circles and triangles, respectively. To determine the predicted frequency $k_z L_z = \pi$ was used.

$\sim$50%. Artificially increasing the shear flow (by increasing the extrema in the azimuthal flow velocity) in the eigenmode solver produces a linearly decreasing growth rate until complete damping of the modes is obtained. However, the real part remains relatively constant (less than $\sim$30% change). This result suggests control of the shear flow could result in the ability to suppress the observed modes.

Qualitatively, the complex radial eigenfunctions in the regions with increased shear flow get phase-shifted by a radially-dependent complex phase, which physically corresponds to the eigenmode being dragged azimuthally in the direction of the imposed flow. The local stability is mainly determined by the plasma dispersion function; the global stability, however, is roughly determined by a summation of the local growth rates. As shear flow introduces a radially-dependent Doppler shift in the plasma dispersion function, the sign of the local growth rate can reverse in radius. Therefore, the solutions to the resulting global eigenmode problem depend sensitively on the specific zeroth-order profiles used as inputs. Accurate measurements of the experimental growth rates are not possible due to the fast-growing nature of the modes. We discuss some of the possible reasons for the discrepancy between the eigenmode solutions and experiment in the next section.

5.1.4 Discussion

There are several limitations to the linear stability analysis that are mentioned here. First, we have forgone a full kinetic description of electron-ion collisions, and have only approximated the collision terms; problems associated with analyticity arise when considering the combined contributions of pitch-angle Coulomb scattering and sheared flow. Based on previous studies of the stability of drift-Alfvén modes in the presence of thermal gradients and collisions without shear flows, the eigenmode stability is sensitive to finite electron-ion collisionality and form of the collision

model [21].

Second, we used the flow velocity and temperature profile measured at one axial location near the cathode as the input to the model. It is well established that the filamentary structures have axial inhomogeneity in the temperature, density, and potential profiles. A 2D radial-axial eigenmode analysis would be a necessary step to incorporate the inhomogeneous temperature and density and the simultaneous effects of axial and radial shear in the azimuthal flow.

A third possibility for the breakdown of linear theory is at early times when the finite amplitude of the modes leads to nonlinear interaction. The fastest-growing modes may transfer energy into linearly stable modes through mode-mode coupling leading to additional physics that is unaccounted for by the linear analysis.

5.2 Time Series Analysis and Intermittency

In this section, we focus further on the turbulent transport observed in the tight filament bundle with an emphasis on time series analysis undertaken at two axial locations, z_1 and z_2 which exhibit significant axial variation. In Section 5.2.1 we perform a short repeat analysis of the drift-Alfvén modes observed, they are similar to the past section but differ slightly in frequency and the level of mode mixing. In setting up the experiment an attempt was made to position the sources in nearly the same position as the first round of experiments presented in the last section, Section 5.1. This appears to have been successful but slight variations could account for the variation in mode frequencies, as well as slightly different background plasma density, cathode emissivity, and source power. In Section 5.2.2 the turbulent fluctuations are investigated by direct analysis of the time series and in Section 5.2.3 the complexity-entropy plane and Hurst exponent are used to explore the underlying deterministic dynamics.

5.2.1 Global Drift-Alfvén Eigenmodes

Fig. 5.11(a) presents the time traces of the ion saturation current, I_{sat}, shown at several locations within the filaments and these are marked in the I_{sat} planes taken at two different times and two axial locations in the lower panels. It is clear from the I_{sat} color maps Figs. 5.11(b) and (d) that at early time, $t = 3$ ms, the transverse profile of the heating is non-uniform axially with an apparent merging of the filaments at the further port, $z = z_2$, from the source. Starting at around $t = 12$ ms the merged bundle at z_2 begins to separate and by $t = 14$ ms three distinct filaments are evident at both ports, shown in Figs. 5.11(c) and (e).

Using the time window of $t = 3 - 6$ ms, the power spectra of the fluctuations δI_{sat} are displayed in Fig. 5.12(a) and Fig. 5.12(b) for the two different axial planes

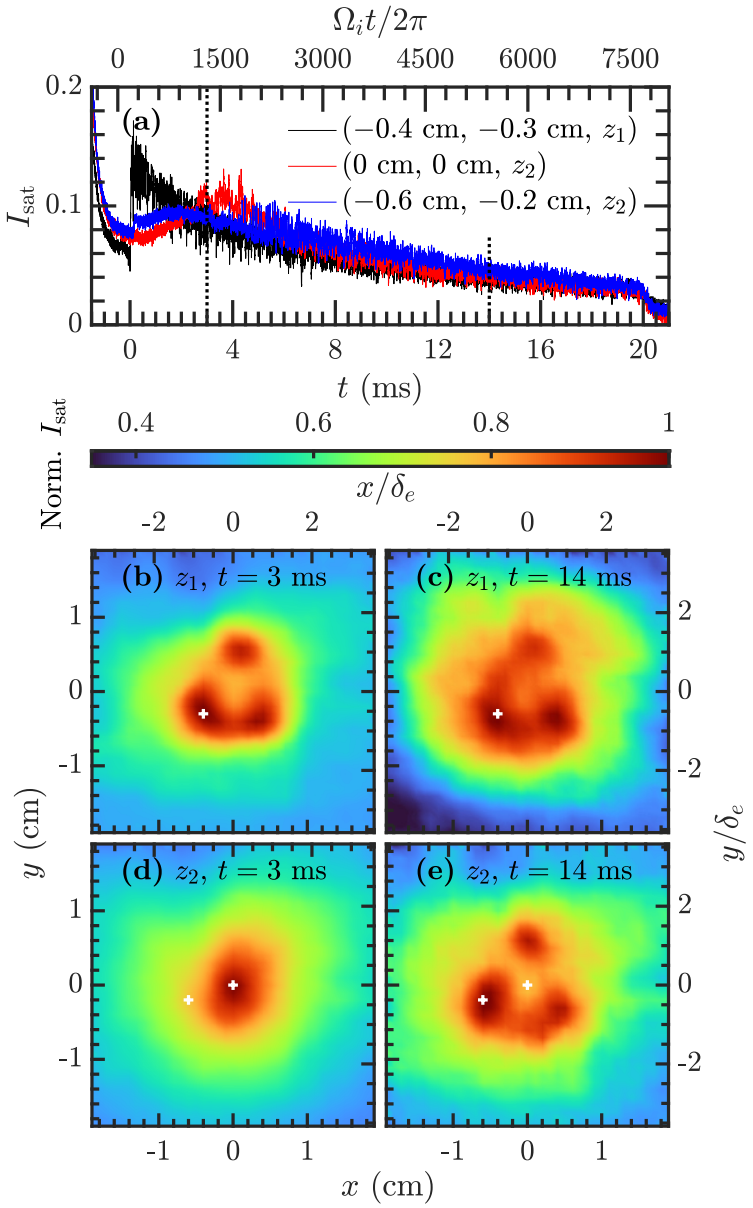

Figure 5.11: (a) Ion saturation current, I_{sat}, time traces at z_1 and z_2; locations are indicated in the legend. (b) and (c) Transverse planes at z_1 of normalized I_{sat} at the times indicated by the dashed black lines in (a), $t = 3$ ms and $t = 14$ ms, respectively. (d) and (e) The same transverse planes at z_2. The white crosses indicate the spatial location of the time traces in (a). I_{sat} is normalized to the maximum at each time.

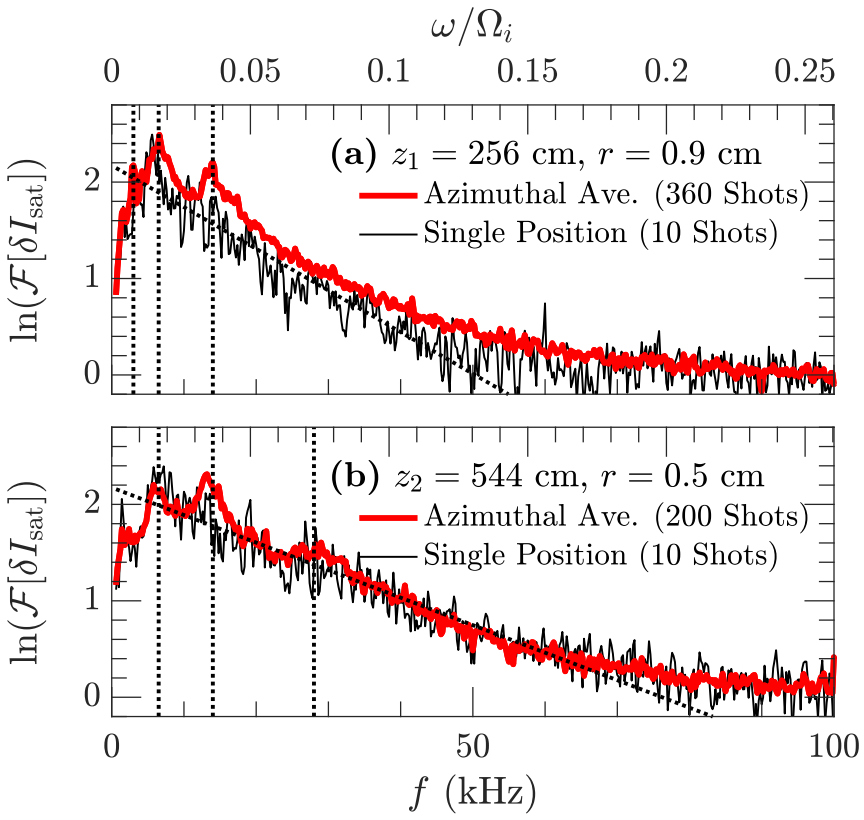

Figure 5.12: Power spectra $\delta I_{\rm sat}$ over the time window $t = 3$ ms to 6 ms relative to the spectrum of the afterglow plasma. (a) At z_1 and $r = 0.9$ cm and (b) at z_2 and $r = 0.5$ cm. The black line is the spectrum averaged over 10 shots at a single position, the thick red line shows the azimuthal average. The dotted black lines indicate the slope of the exponential frequency spectrum and the location of coherent modes.

at $z_1 = 256$ cm and $z_2 = 544$ cm, respectively. The radial locations for the single position measurements and azimuthal averages are in the vicinity of the maximum thermal gradient at each axial location. Several dominant frequency peaks are evident along with a background exponential frequency spectrum. The origin of the broad exponential spectrum is discussed in the next section. The spectral peaks, indicated by the dotted black lines, are used to make cross-correlations between the moving probe at a particular plane and a nearby reference probe at z_R, thus illuminating the mode structures at each frequency in the transverse plane.

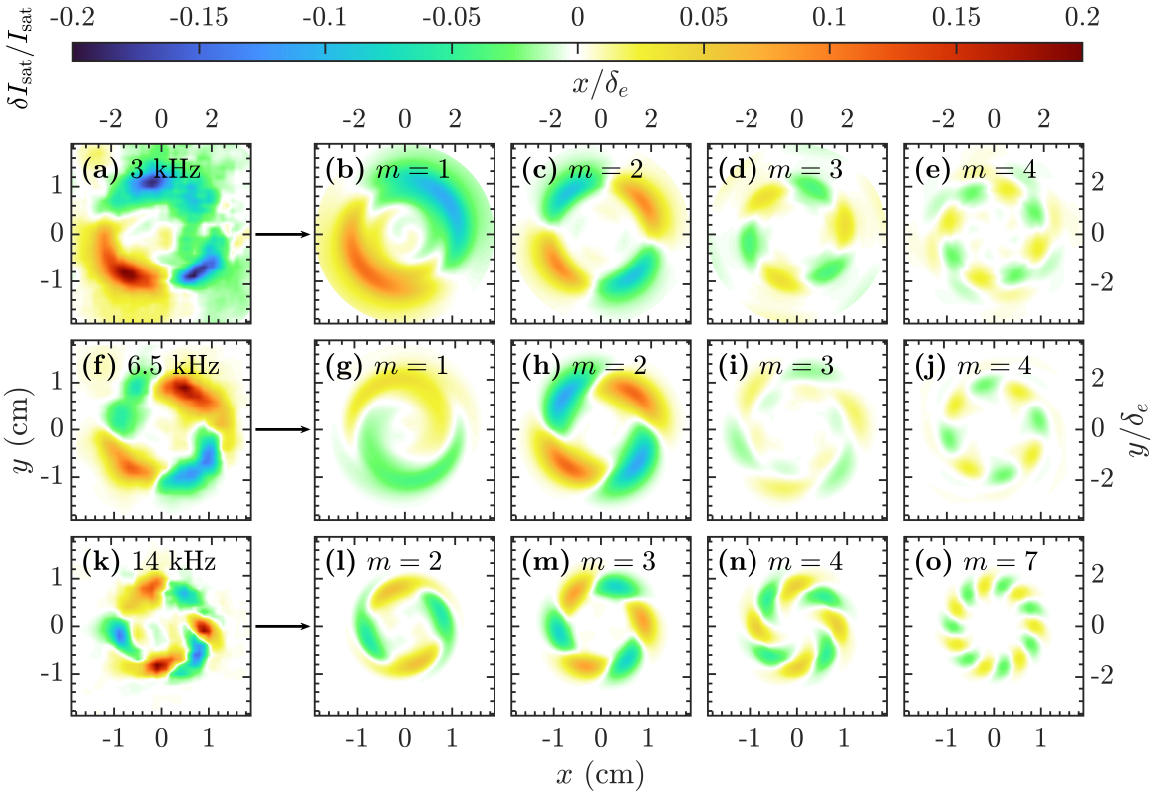

Figure 5.13: (a), (f), and (k) Transverse planes of the cross-correlation between the moving probe at z_1 and a reference probe at z_R for the frequencies of the modes in Fig. 5.12(a), i.e. 3 kHz, 6.5 kHz, and 14 kHz, respectively. For each of panels (a), (f) and (k) the the Fourier decomposition into the four largest azimuthally symmetric mode numbers is shown to the right; panels (b)-(d) for (a), (g)-(j) for (f), and (l)-(o) for (k).

The results of this analysis are shown in Figs. 5.13(a,f,k) for the axial location z_1 and Fig. 5.14(a,f,k) for z_2. It was shown in the previous section that these modes correspond to drift-Alfvén waves driven by the outer gradient of the filament bundle. Here we perform a Fourier decomposition of the quasi-symmetric mode patterns into azimuthal mode numbers at each frequency; the four most dominant modes are shown in the panels to the right of each cross-correlation. In Fig. 5.13 the decomposition of the three dominant spectral peaks at 3 kHz, 6.5 kHz, and 14 kHz reveals the dominance of mode numbers $m = 1$, $m = 2$, and $m = 3$, respectively. However, the

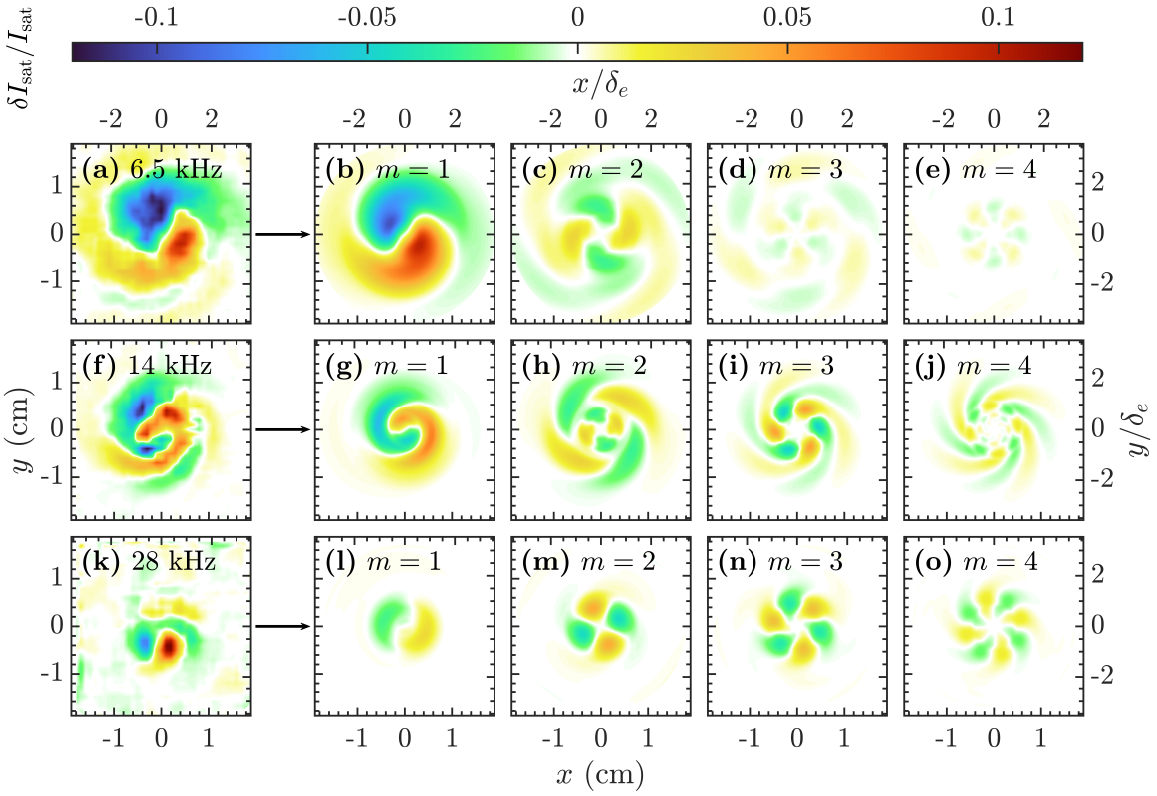

Figure 5.14: (a), (f), and (k) Transverse planes of the cross-correlation between the moving probe at z_2 and a reference probe at z_R for the frequencies of the modes in Fig. 5.12(a), i.e. 6.5 kHz, 14 kHz, and 28 kHz, respectively. For each of panels (a), (f) and (k) the the Fourier decomposition into the four largest azimuthally symmetric mode numbers is shown to the right; panels (b)-(d) for (a), (g)-(j) for (f), and (l)-(o) for (k).

observed modes are in fact superpositions of several coherent modes; for example, the $m = 2$ mode is nearly as prevalent as the $m = 1$ at 3 kHz and the pattern at 14 kHz is a superposition of comparable modes at $m = 2$, 3, and 4. This is evidence of some form of nonlinear interaction between the drift-Alfvén modes and is a common route to turbulence in magnetized plasmas [55, 56]. Fig. 5.14 shows that from the source at z_2 the dominant power resides in the $m = 1$, $m = 3$, and $m = 2$ eigenmodes for each of the dominant frequencies 6.5 kHz, 14 kHz, and 28 kHz, respectively. This shift in azimuthal mode dominance and frequency is correlated with the axial inhomogeneity.

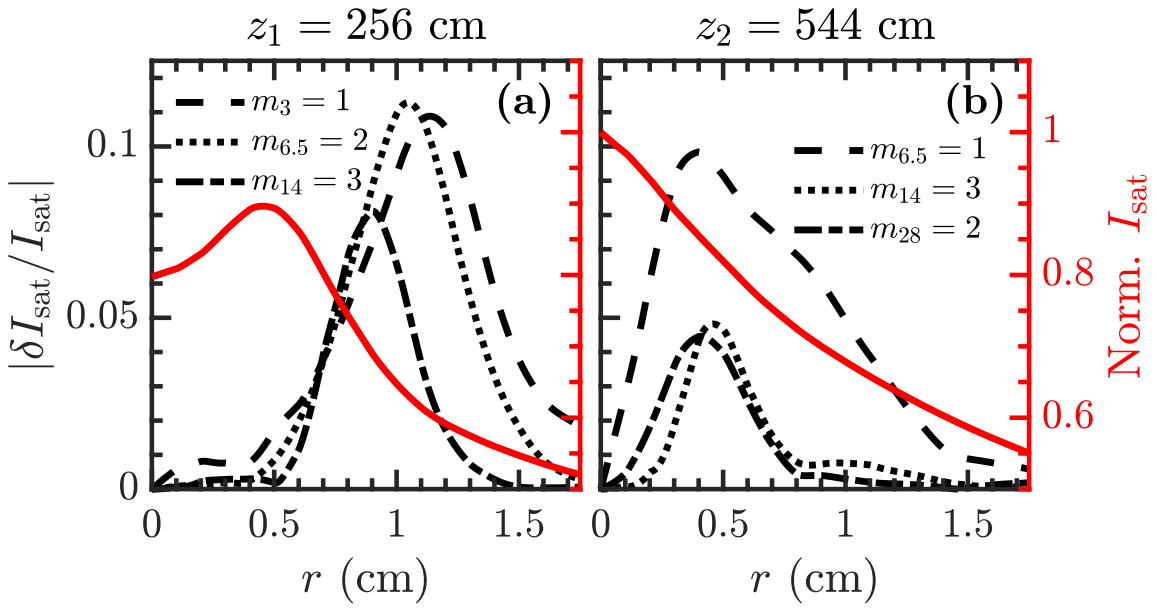

Figure 5.15: Radial structure of the largest decomposed modes at each frequency at (a) z_1 and (b) z_2. Left axis is $\delta I_{sat}/I_{sat}$ for the modes corresponding to the black dashed, dotted, and dash-dotted lines. Right axis is normalized I_{sat} corresponding to the red line showing the azimuthally averaged profile at 3 ms; the profile in each is normalized to maximum I_{sat} observed at that time.

Again, while there is a dominant mode at each frequency there is comparable power in other mode numbers that together form the observed mode patterns.

In Fig. 5.15 the radial structures of the largest decomposed modes at each frequency are shown along with the azimuthally averaged and normalized I_{sat} profiles at z_1 and z_2. As the off-axis peak in the profile at z_1 shifts to the center at z_2, the peaks in the mode amplitude also move inwards and track the steepest region of the outer gradient of the bundle. The nonlinear mode coupling observed at z_1 and z_2 provide a mechanism for the turbulent fluctuations in I_{sat}, observed in Fig. 5.11(a) and discussed in the next section, that are characterized by intermittent events localized to the outer gradient of the filamentary structures.

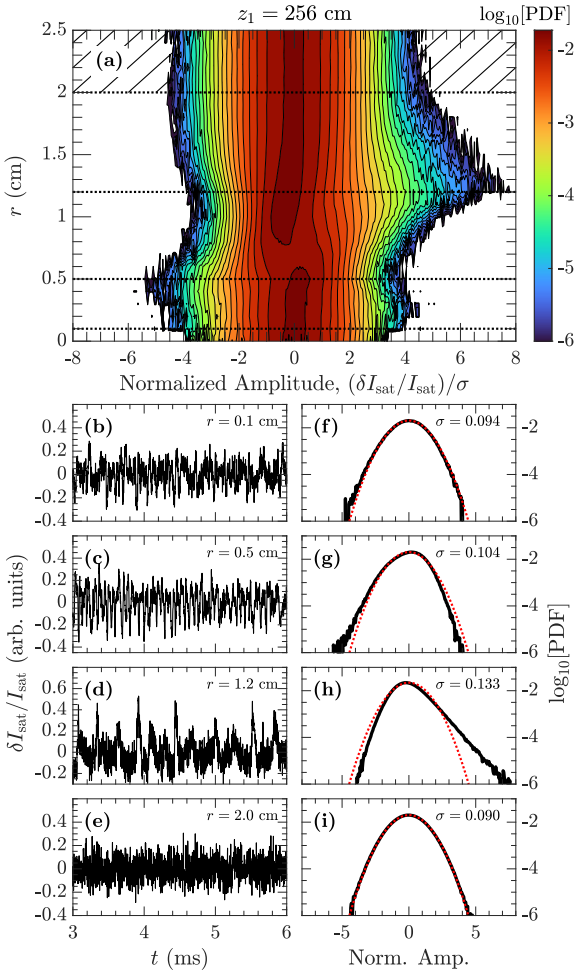

Figure 5.16: (a) Contour plot of the azimuthally averaged PDF of $\delta I_{\rm sat}/I_{\rm sat}$ fluctuation amplitude between $t = 3$ ms and $t = 6$ ms at z_1. The horizontal axis is the fluctuation amplitude normlized to the standard deviation, vertical axis the radius, and the contours are base 10 logarithm of the PDF. (b)-(e) raw $\delta I_{\rm sat}/I_{\rm sat}$ signals at select locations indicated by the dotted black lines in (a). (f)-(i) corresponding amplitude PDF of the raw signals in black, a Gaussian distribution is shown by the dotted red lines. The PDF in (i) corresponds to the combined PDF of the hatched region in (a).

5.2.2 Intermittent Transport Events

In this section, we present a statistical analysis of these transport events and use conditional averaging to perform a spatiotemporal reconstruction. Intermittency can

be identified by non-Gaussian amplitude probability distribution functions (PDFs) of the measured signals. An increase in the frequency of large intermittent events within a signal will significantly impact the tails of the distribution. A larger negative tail in the distribution indicates depletion or “hole", events and a larger positive tail indicates enhancement events[51]; the depletions or enhancements in $I_{\rm sat}$ could be density or energy. The colour plot in Fig. 5.16(a) shows the azimuthally averaged amplitude PDF on a logarithmic scale at each radius of the filamentary bundle at z_1 between $t = 3$ ms and $t = 6$ ms with 10 shots at each position in the (x, y) plane. The fluctuation amplitudes $\delta I_{\rm sat}/I_{\rm sat}$ are normalized to the standard deviation of the distribution, σ. Shown in the left panels, Figs. 5.16(b)-(e), are temporal traces of the fluctuations in single shots at radii $r = 0.1$, 0.5, 1.2, and 2.0 cm and indicated by dotted lines in Figs. 5.16(a). The right panels, Figs. 5.16(f)-(i), display the PDF of the normalized amplitude for the same radii; the PDF in Fig. 5.16(i) corresponds to a cumulative PDF of the hatched region ($r \geq 2.0$) in Fig. 5.16(a) where the fluctuation amplitude PDFs are all similar. It is important to note that while the filament bundle at z_1 has some azimuthal asymmetry in the $I_{\rm sat}$ profile, the azimuthal variation of the PDF was found to be minimal.

Near the center of the multi-filament structure, Figs. 5.16(b) and (f), the signal is characterized by nearly Gaussian fluctuation amplitudes with a small enhancement of the negative tail, indicating some tendency for depletion events. The 2D PDF shows that the frequency and size of these depletion events grows further from the center and peaks at around $r = 0.5$ cm; this is also where the radial $I_{\rm sat}$ profile peaks in Fig. 5.15(a). The PDF at $r = 0.05$ cm is more clearly seen in Fig. 5.16(g); in the corresponding time trace in Fig. 5.16(c) it is observed the events are short lived in time only lasting on the order of several μs.

Beyond $r \approx 0.8$ cm the PDF switches to an asymmetry skewed towards positive

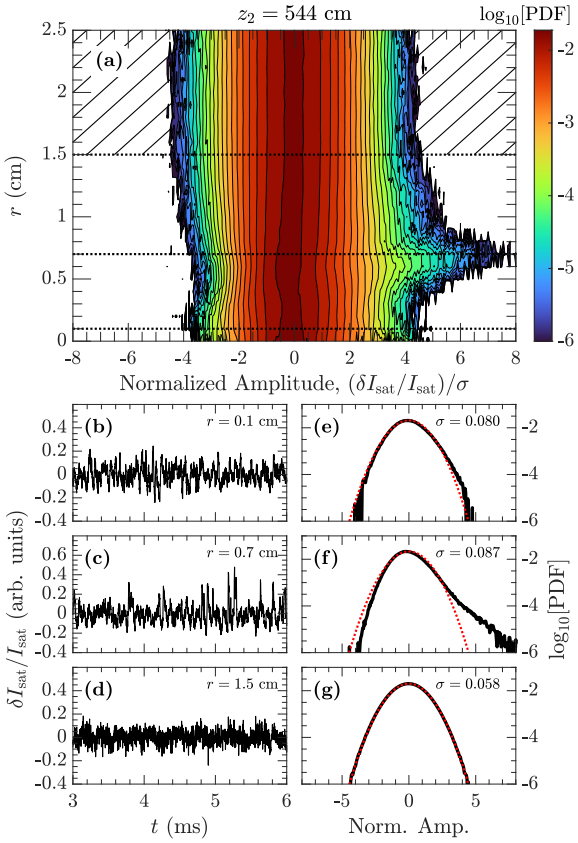

Figure 5.17: (a) Contour plot of the azimuthally averaged PDF of $\delta I_{sat}/I_{sat}$ fluctuation amplitude between $t = 3$ ms and $t = 6$ ms at z_2. The horizontal axis is the fluctuation amplitude normlized to the standard deviation, vertical axis the radius, and the contours are base 10 logarithm of the PDF. (b)-(d) raw $\delta I_{sat}/I_{sat}$ signals at select locations indicated by the dotted black lines in (a). (e)-(g) corresponding amplitude PDF of the raw signals in black, a Gaussian distribution is shown by the dotted red lines. The PDF in (g) corresponds to the combined PDF of the hatched region in (a).

events on the outer gradient. At $r = 2.0$ cm; and beyond the PDF is well described as Gaussian as evidenced by the fluctuations at 2.0 cm in Fig. 5.16(e) and the spatial cumulative PDF in Fig. 5.16(i). The extreme of the positive skewness to the PDF occurs at $r = 1.2$ cm and corresponds to the amplitdue peak of the drift-Alfvén modes in Fig. 5.15(a). The single shot at $r = 1.2$ cm in Fig. 5.16(d) and associated PDF in (g) shows the positive events are large pulses with widths on the order of tens of ns.

A similar PDF analysis is carried out at z_2 and is shown in Fig. 5.17; the format is the same as Fig. 5.16. Here the fluctuations are nearly Gaussian at the center of the combined filament structure. A sharp transition to positive intermittent transport events occurs on the gradient between $r = 0.4$ cm and $r = 1.0$ cm, with the extreme of the skewness again coinciding with the peak in the drift-Alfvén amplitudes. The fluctuations become low amplitude and nearly Gaussian beyond $r = 1.5$ cm, similar to beyond $r = 2.0$ cm at z_1.

At both axial locations, z_1 and z_2, large positive intermittent events are located on the outer gradient of the filament bundle where there are drift-Alfvén modes and the existence of a broadband exponential frequency spectra, as seen in Fig. 5.12. Previous work has highlighted the observation of Lorentzian-shaped pulses in the turbulent regime created by only a single filament [19, 20]. These pulses were observed on the gradient of the single filament and are linked to the observation of anomalous cross-field energy transport rates, exponential frequency spectra, and deterministic chaos [22, 61, 62, 97]. Thus, a closer inspection of the positive events on the outer gradients at z_1 and z_2 is warranted.

Identification of the positive intermittent pulses embedded in the present data is straightforward due to the large amplitudes above the statistical variation. A search algorithm is used to identify pulses in time series of length 8192 points across the time range $t = 3$ to ~ 10 ms; the time is restricted to the range where the filaments remain merged at z_2. The time signals are first low pass filtered to remove frequency content above 35 kHz. A dynamic threshold amplitude is used to isolate maxima corresponding to the large intermittent events; a threshold of twice the mean of the absolute signal amplitude over a moving 1 ms window was found to be suitable. There is no doubt that some pulses are not identified – some may be small and embedded within the statistical variation and others obscured or distorted by wave fluctuations

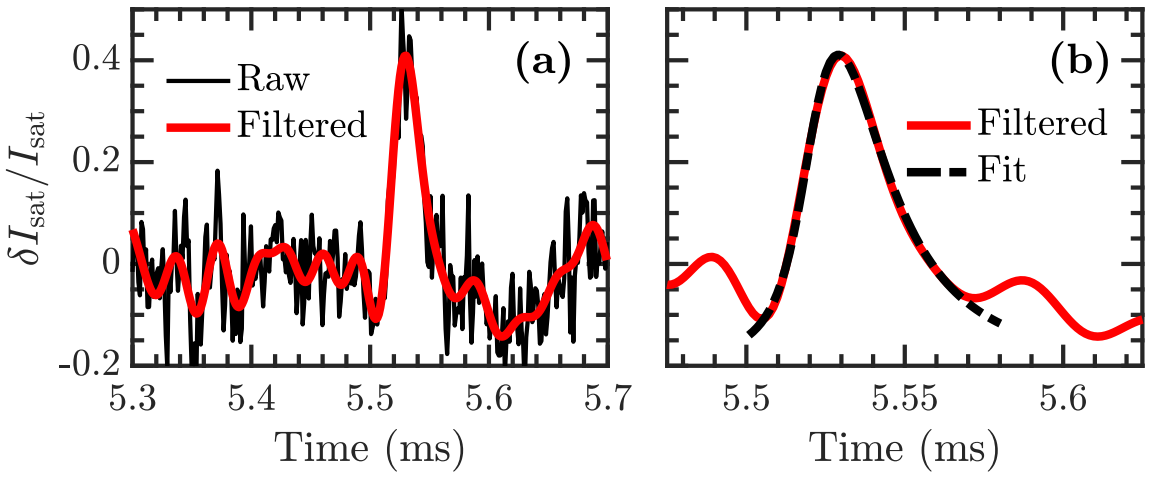

Figure 5.18: (a) Raw and filtered signals observed at $r = 1.5$ cm showing a single intermittent event. (b) Same filtered event with a fit to Eq. (5.5) with $\alpha = 1$.

in their temporal vicinity – this is an unavoidable outcome and many thousands of pulses are still identified within all of the shots.

Lorentzian shaped pulses can be distinguished from Gaussian or other similarly shaped events by the presence of an exponential frequency spectrum associated with the pulses. A general form for pulsed events is described by the stable distribution given by the following function in the Fourier domain [98],

$$\ln[\tilde{\mathcal{L}}] = i\omega t_0 - (\tau|\omega|)^\alpha(1 + i\beta\Phi(\omega, \alpha, \tau)) \tag{5.5}$$

where,

$$\Phi(\omega, \alpha, \tau) = \begin{cases} \operatorname{sgn}(\omega)\tan(\frac{\pi\alpha}{2})(|\tau\omega|^{1-\alpha} - 1) & \alpha \neq 1 \\ \frac{2}{\pi}\operatorname{sgn}(\omega)\log(\tau|\omega|) & \alpha = 1 \end{cases}$$

In Eq. (5.5) t_0 is a location parameter, τ is a scale parameter ($\tau > 0$), β is

a skewness parameter ($-1 \leq \beta \leq 1$), and α is known as the shape or stability parameter ($0 < \alpha \leq 2$). For zero skewness (i.e. $\beta = 0$) the distribution is symmetric. The distribution is equivalent to a Levi distribution if $\alpha = 0.5$, a Gaussian distribution if $\alpha = 2$, and a Lorentz (or Cauchy) distribution if $\alpha = 1$. The shape parameter, α, is important for a discussion of the form of the function in the Fourier domain; only when $\alpha = 1$ is the function exponential in frequency and this remains so for any value of β. The exponential decay rate, or the slope on a log-linear spectrum, is proportional to the parameter τ. Thus, an exponential frequency spectrum can be evidence of Lorentzian-shaped signals in the time domain, and vice-versa. Maggs and Morales have argued that the log-log formats of power spectra have obscured the exponential frequency spectrum of intermittent turbulence observed in several magnetic confinement plasma devices [61]; additionally, the intermittent pulses in these devices, including similar filamentary experiments in the LAPD, are Lorentzian shaped [97] and the source of the exponential frequency spectra [22].

The broadband exponential spectra in Fig. 5.12 are strong evidence that the pulses identified herein are also of Lorentzian form. In Fig. 5.18(a) an example of a probe signal with a single intermittent event at z_1 and $r = 1.5$ cm is displayed along with the filtered time trace used for identifying the pulses systematically. Fig. 5.18(b) shows the same filtered pulse with a fit to Eq. (2) using $\alpha = 1$ and additional amplitude and offset parameters. The pulse is accurately described by a Lorentzian function with $\tau = 15.3 \pm 0.4$ ms and a positive skewness of $\beta = 0.53 \pm 0.03$; the error is described by 95% confidence intervals. The choice of fixing $\alpha = 1$ is justified by the presence of the exponential spectra, however, we note that performing the fit with a variable α results in similar τ and β with $\alpha = 1.01 \pm 0.04$ and further confirms the Lorentzian shape of the pulses.

Verifying an accurate fitting of each pulse to Eq. (5.5) is not practical and each

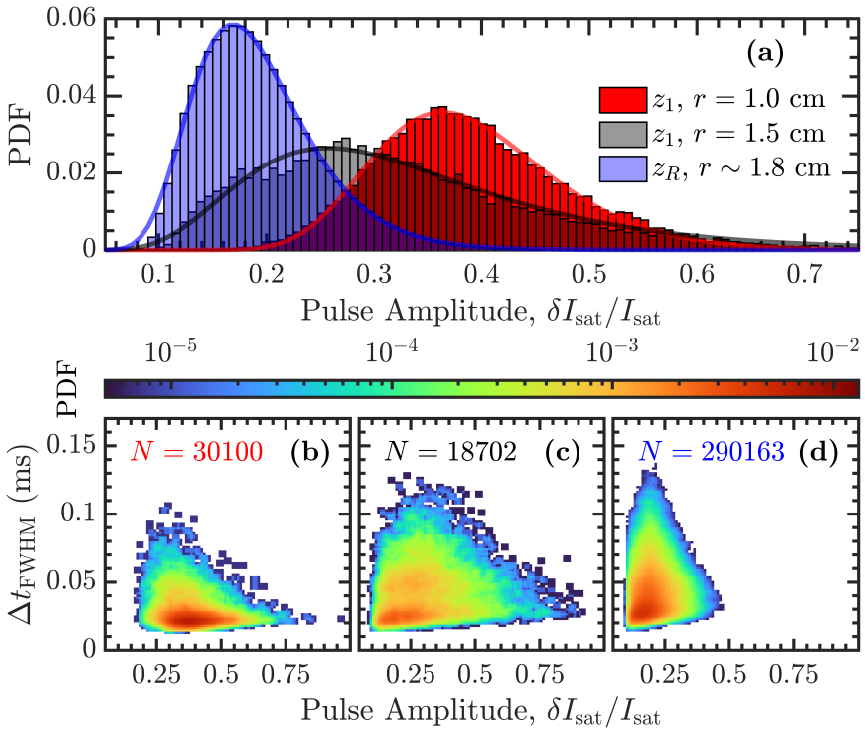

Figure 5.19: (a) PDF of the amplitude of the intermittent pulses at z_1 for $r = 1.0$ cm (red boxes) and $r = 1.5$ cm (grey boxes), and z_R for $r = 1.8$ cm (blue boxes); the colored lines are a log-normal distribution corresponding to each PDF. (b)-(d) Bivariate distribution of pulse width, Δt_{FWHM}, and amplitude for each of the PDFs in (a) in order of increasing radius. N corresponds to the number of pulses identified in each case.

pulse can be quickly characterized by a normalized amplitude ($\delta I_{sat}/I_{sat}$) and a full width at half maximum (FWHM), Δt_{FWHM}. The Lorentzian scale parameter τ is related to Δt_{FWHM} by the approximation $\Delta t_{FWHM} \approx 2\tau$, where the approximation becomes an equivalence for a symmetric pulse with $\beta = 0$. Figs. 5.19 and 5.20 show the pulse amplitude PDFs and bivariate PDFs of pulse width and amplitude at different axial locations and radii.

In Fig. 5.19(a) we can see that the normalized amplitude PDFs are well described by log-normal distributions with decreasing mean amplitudes further from the outer gradient. For $r \approx 1.8$ cm the pulses identified on the reference probe at z_R are used

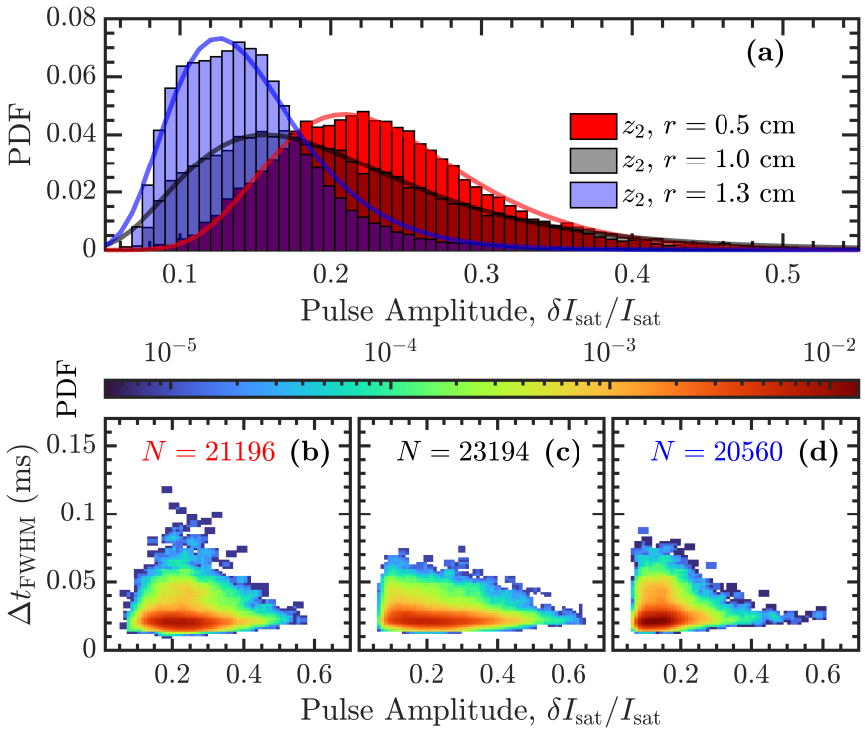

Figure 5.20: (a) PDF of the amplitude of the intermittent pulses at z_2 for $r = 0.5$ cm (red boxes), $r = 1.0$ cm (grey boxes), and $r = 1.3$ cm (blue boxes); the colored lines are a log-normal distribution corresponding to each PDF. (b)-(d) Bivariate distribution of pulse width, $\Delta t_{\rm FWHM}$, and amplitude for each of the PDFs in (a) in order of increasing radius. N corresponds to the number of pulses identified in each case.

instead of those on the moving probe at z_1 since the larger number of pulses identified provides a better indication that the log-normal fit is appropriate; the slight discrepancy for $\delta I_{\rm sat}/I_{\rm sat} \lesssim 0.1$ is likely due to the pulses being too small to easily identify. In the bivariate distribution of Fig. 5.19(b) the pulse width is narrowly distributed at $r = 1.0$ cm (note the logarithmic PDF scale) and the distribution spreads out further down the gradient Figs. 5.19(c) and (d). At z_2 in Fig. 5.20(a) similar log-normal distributions in the amplitude are observed; the amplitude distributions again shift to lower mean amplitudes further from the center and become more narrow on the edge of the filamentary structure. The bivariate distributions in Figs. 5.19(b-d) show less

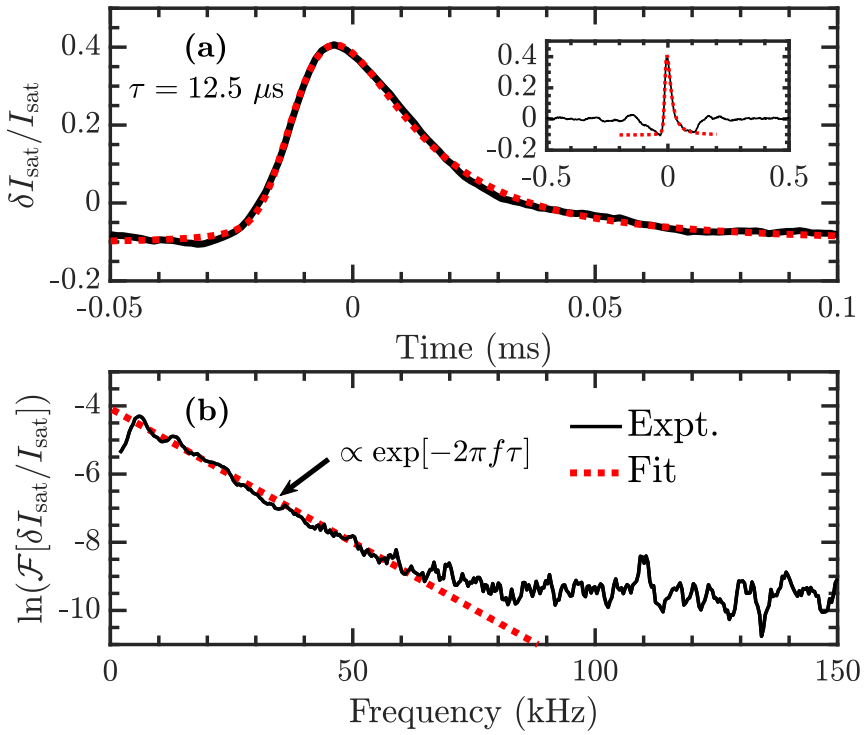

Figure 5.21: Conditionally averaged pulse event at z_1 and $r = 1$ cm. (a) Temporal trace of the event with the experiment data in black, and the fit to Eq. (5.5) with $\alpha = 1$ given by the dashed red line; inset, larger temporal scale of the conditional averaging. (b) Fourier transform of the signals in (a) showing the exponential frequency spectrum corresponding to a Lorentzian shaped pulse.

evidence of the pulse width distribution spreading out further from the center; the filaments remain merged at this axial location and the tighter configuration may be the cause of the spatial homogeneity of the event widths.

The pulses identified can be used to construct the average pulse shape; Fig. 5.21 and Fig. 5.22 show this result for a radial location on the gradient at z_1 and z_2. In both figures the top panels ((a)) show the time trace of the average pulse fit to Eq. (5.5) and the bottom panels ((b)) show the pulse and fit in the Fourier domain. The inset figures in the top panels show a larger temporal extent where outside the main pulse the averaging of the shots results in a nearly flat trace. However, on average, in both

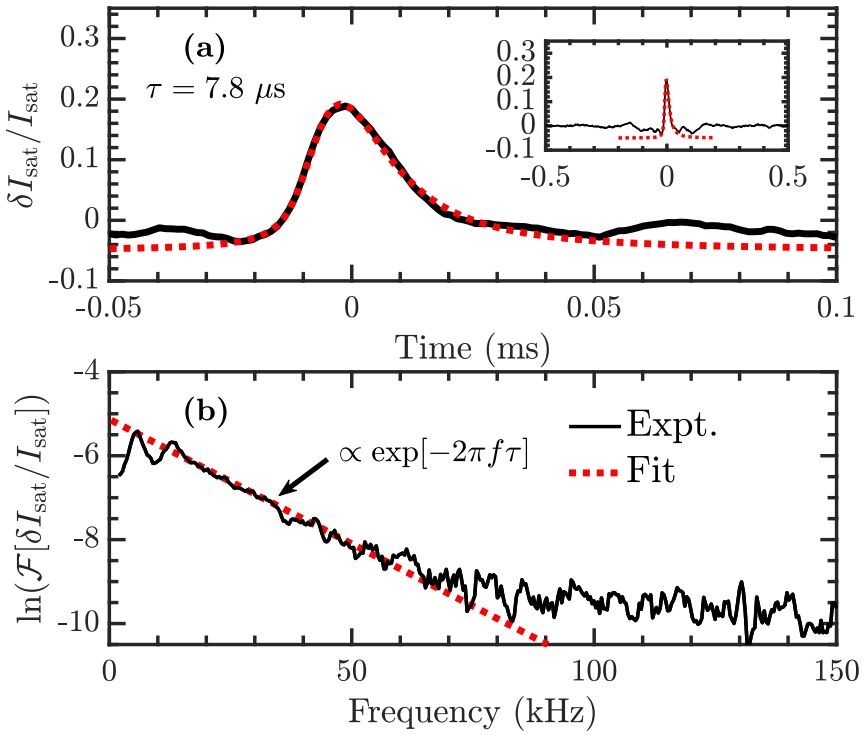

Figure 5.22: Conditionally averaged pulse event at z_2 and $r = 0.7$ cm. (a) Temporal trace of the event with the experiment data in black, and the fit to Eq. (5.5) with $\alpha = 1$ given by the dashed red line; inset, larger temporal scale of the conditional averaging. (b) Fourier transform of the signals in (a) showing the exponential frequency spectrum corresponding to a Lorentzian shaped pulse.

cases the pulses appear within a noticeable depression in $I_{\rm sat}$. In the power spectra, the exponential character is clear and the fits are an obvious match to the slope. Also present in the spectra is evidence of the peaks at 6 kHz and 14 kHz, corresponding to the drift-Alfvén modes at both axial locations, and suggests the wave modes may be correlated with the pulse generation.

The placement of the reference probes on the gradient allows for conditional averaging of the temporal signals on the moving probe at z_1 when a pulse occurs on one of the reference probes. This results in a spatiotemporal reconstruction of the average pulse event at z_1 and is shown in Fig. 5.23. It is important to note that

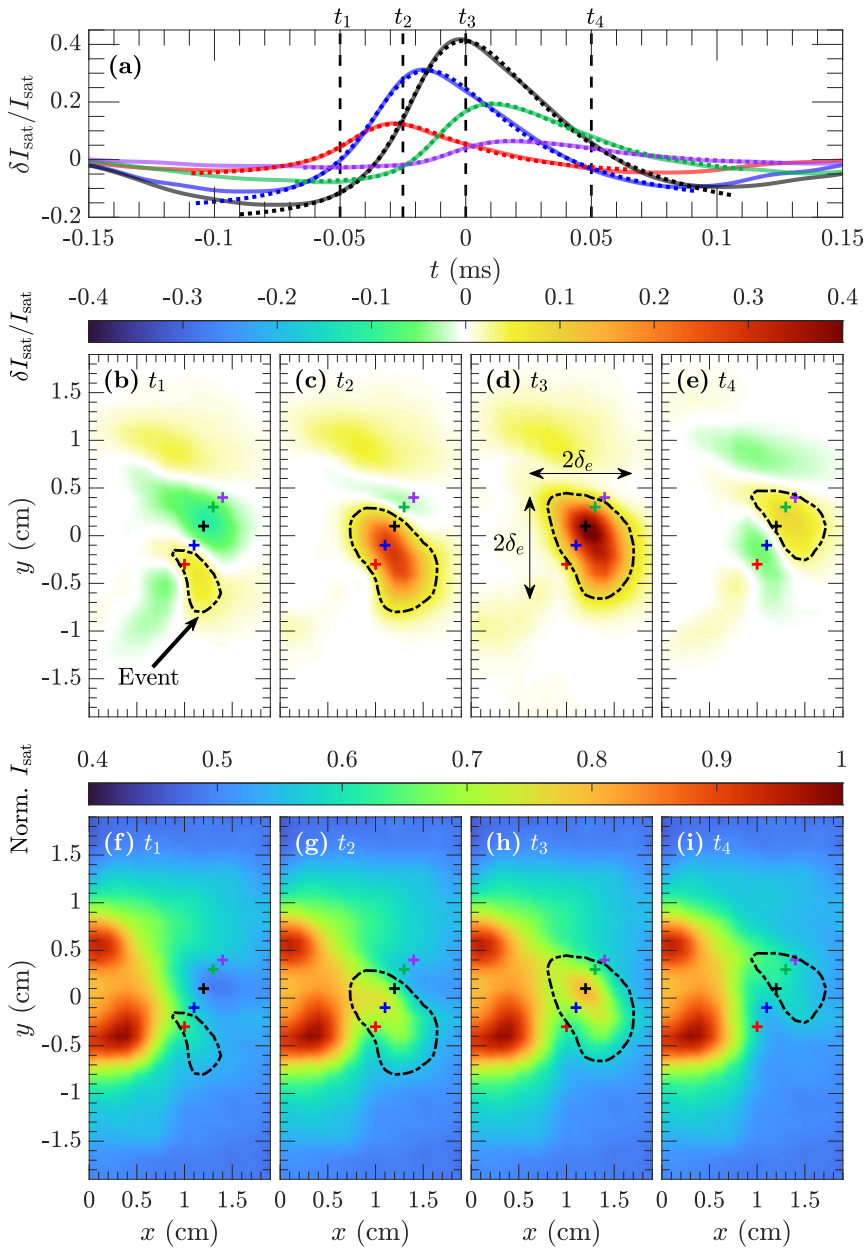

Figure 5.23: Cross conditional average of pulse event at z_1 using events triggered on the stationary reference probe at z_R. (a) Experimental time traces (solid lines) with fits to Eq. (5.5) with $\alpha = 1$ (dashed lines). The locations of the time traces are indicated by the corresponding colored crosses in (b) to (i). Panels (b)-(e) show transverse planes of $\delta I_{sat}/I_{sat}$ at times t_1, t_2, t_3, and t_4, respectively, indicated by the vertical dashed black lines in (a). The contours (black dash dotted) highlight the intermittent event. Panels (f)-(i) are the same format as panels (b)-(e) but show normalized I_{sat}.

in this analysis, the observed spatial structure of the pulse is a reconstruction from many pulse events detected at the reference probe that do not necessarily represent identical spatially situated events, either in the transverse (x, y) plane or axially in z. Some of the observed events on the reference probe could be the end or beginning of a pulse, near the edge of a pulse in the transverse plane or axially, and some pulses may not even extend to z_1 and may wash out or distort the reconstruction. To help mitigate this issue, only the largest 50% of pulses detected at z_R were used as these pulses are more likely to represent events with maxima localized to the vicinity of the reference probe; using all of the pulses does result in a similar reconstruction, albeit one that is diminished in amplitude and more spread out in the transverse plane, as expected. Additionally, given that a spatial reconstruction at z_1 is possible when the events occurred at z_R, it can be concluded that the axial extent of the events is at least $\Delta z_{1,R} = z_R - z_1 = 64$ cm. Performing the same conditional averaging at z_2 results in no coherent reconstruction of the pulse event, indicating the pulses at z_R are not correlated with pulses at z_2, and an upper bound on the axial extent of the structures can be set at $\Delta z_{R,2} = z_2 - z_R = 224$ cm.

In Fig. 5.23(a) the time traces track the path of the reconstructed event and each has been fit to Eq. (5.5) showing the persistence of the Lorentzian pulse shape throughout the evolution. The panels of Figs. 5.23(b-e) show frames of the normalized fluctuation level with the event indicated by the dashed contour line and panels (f-i) show the normalized ion saturation current with the same contouring around the event structure; the coloured crosses in each frame indicate the location of the time traces in (a) and the dashed lines in (a) show the time of each frame. A clear feature of the fluctuation panels is that the phase of the drift-Alfvén waves is also correlated with pulses occurring at z_R. At the time t_1 there is an obvious mixed mode structure between a lower mode number of $m = 2$ and a higher mode number of perhaps $m = 3$

or 4. The pulse event itself evolves out of an arm of the drift wave and grows to a large amplitude before dissipating. At its largest extent in the transverse plane (Fig. 5.23(d)) the event is on the order of $2\delta_e$ across. In fluctuation panels for t_2 and t_3 the pulse appears to be situated where a depression in an $m = 2$ mode should be, much like the averaged pulses in Fig. 5.21 and Fig. 5.22 sit within a depression. The frames (b-e) offer clear evidence that the intermittent Lorentzian pulses are generated by a nonlinear interaction between drift-Alfvén modes.

In the lower I_{sat} panels the event appears as an eruption on the gradient of the filamentary bundle that travels a short distance around the structure in the direction of the drift waves before dissipating. As mentioned this event is a reconstruction of an ensemble of events that occur at a similar location in the (x, y) plane as the reference probe; a reconstruction using the reference probe on the other side of the filaments produces a similar event. Thus, the occurrence of pulses of varying amplitude and width all around the filaments and also on the gradient at z_2 gives the impression that these eruption events occur sporadically all around the bundle and along the full axial length of the filaments. Given that the I_{sat} signal is dominated by temperature (see Fig. 2.14(b)) it is likely that the observed events correspond to anomalous energy transport. However, this cannot be said with certainty and in the future conditionally averaged reconstructed sweeps could be used to confirm if these events correspond to density or temperature depletions [70, 99]; additionally, while the reference probes in this experiment were placed on the gradients to obtain information on the drift-Alfén modes, placing a reference probe in the middle of the bundle may allow a spatiotemporal reconstruction of the negative events observed in the PDF at z_1 (Fig. 5.16(a)).

5.2.3 Chaotic Fluctuations and Signal Persistence

In this section, we relate the transport dynamics to deterministic chaos and investigate the time-series memory using the Hurst exponent. Lorentzian shaped pulses and exponential frequency spectra are a signature of chaotic dynamics; a technique gaining usage in the plasma community for analyzing chaotic signals is that of the complexity-entropy plane or "CH-plane" that can be used to distinguish between periodic, stochastic, and chaotic signals [100]. Maggs and Morales made the first application of the CH-plane to a plasma experiment and demonstrated the chaotic nature of turbulent fluctuations on the gradient of past single filament experiments in the LAPD [22]. The technique has since been applied to experiments involving magnetic flux ropes [101, 102] and comparisons of laboratory turbulence and the solar wind [103]. Here we apply this technique to the full plane of data in the multi-filament and single filament cases.

The CH-plane is constructed from two measures of the signal, the permutation entropy and statistical complexity. Both measures may be calculated using a probability distribution introduced by Bandt and Pompe [104]. The distribution is calculated from the amplitudes of a signal of length N_t divided into $N_t - D + 1$ sequential sets of length D, where D is referred to as the embedding dimension. The distribution represents the probabilities of the $N = D!$ permutations, ρ, of the ordering of the amplitudes of each set. For example, given the sequence $x = [1, 4, 5, 1, 3, 2]$ and embedding dimension $D = 3$, there are $N = 6$ permutations and $N_t - D + 1 = 4$ sets of length D: $[1, 4, 5]$, $[4, 5, 1]$, $[5, 1, 3]$, and $[1, 3, 2]$. These sets have the permutations ρ: (012), (120), (201), and (021), which each have probability $p(\rho) = 1/4$; the remaining two permutations, (210) and (102) have no occurrences and zero probability. For a

general time series $\{x_t\}_{t=1...N_t}$ the probability for each ρ can be written [104],

$$p(\rho) = \frac{\#[\{x_t, ..., x_{t+(D-1)}\} \text{ has type } \rho,\ (t|t \leq N_t - D)]}{N_t - D + 1} \tag{5.6}$$

where # represents a count or "number of occurrences". Once the set of N probabilities, $p(\rho)$, is known the entropy and complexity are calculated to find the position of the signal in CH-plane. The entropy is calculated using the Shannon entropy definition [105],

$$S(p) = -\sum_{\rho} p(\rho) \ln(p(\rho)) \tag{5.7}$$

$$H_S(p) = S(p)/S_{max} = S(p)/\ln(N) \tag{5.8}$$

where S is the Shannon entropy, H_S is the normalized Shannon entropy, the sum is over all ρ, and $S_{max} = S(p_e)$ where p_e refers to a uniform distribution across all ρ, i.e. $p_e(\rho) = [1/N, ..., 1/N]$. The statistical complexity is calculated using the Jensen-Shannon complexity defined as [105],

$$C_{JS} = -2\frac{S\left(\frac{p+p_e}{2}\right) - \frac{1}{2}S(p) - \frac{1}{2}S(p_e)}{\frac{N}{N+1}\ln(N+1) - 2\ln(2N) + ln(N)} \tag{5.9}$$

Central to applying the CH-plane technique to experimental data is the concept of sub-sampling or embedding delay [22, 103]. The time series has a time step Δt determined by the sampling frequency, f_s. The CH-plane will resolve dynamical processes, be they stochastic, periodic, or deterministic, that occur on time scales greater than $2\Delta t$, i.e. with a frequency below the Nyquist frequency, $f_N = f_s/2$. Real-world signals from dynamical systems are often characterized by noise beyond the frequencies of interest, such noise will dominate the probability distribution and suppress

the ability of the CH-plane to extract evidence of chaotic dynamics. To handle the issue of noise the signal is sub-sampled by an integer factor m to increase the time step between points in the permutation series $\{x_t\}$ to $m\Delta t$, effectively reducing the Nyquist frequency. Sub-sampling by taking every m sample will reduce the length of the time series to $N_t' = N_t/m$ and exclude the rest of the data; instead, here we use the length preserving technique [103] where the sub-sampling is accomplished by constructing sets of length D as $\{x_t, x_{t+m}, ...x_{t+m(D-1)}\}$ with $t = 1, ..N_t - m(D-1)$, which preserves all of the original data set for the calculation of $p(\rho)$ and increases the sampling time. Continuing our example from above, if the set were sub-sampled with $m = 2$ the length preserving technique gives two sets of length D: $[1, 5, 3]$ and $[4, 1, 2]$, instead of just the former.

In Fig. 5.24 is the CH-plane for three data sets: the 2D (x, y) planes at z_1 and z_2 investigated throughout this article in (a) and (b), respectively; and a 2D (x, y) plane of the single filament during the transport regime where it exhibits turbulent intermittent pulses [19, 20, 22]. Each data set has 10 shots at each position with $N_t = 8192$, $\Delta t = 1.28$ μs, length preserving sub-sampling with $m = 4$, and embedding dimension $D = 5$. First, a description of the different regions of the CH-plane is necessary. The range of the entropy of the signal is $0 \leq H_S \leq 1$ but the complexity C_{JS} at a given entropy is bounded by a minimum and maximum (the black curves in Fig. 5.24); a description of the minimum and maximum conditions is given by Martin *et al*[105]. The left side of the plane is populated by periodic signals with low entropy. For a pure sine wave of frequency f with f_s approaching infinity $p(\rho)$ would tend towards only two non-zero permutations, monotonically increasing and decreasing, and the entropy would approach $H_S = \ln(1/2)/\ln(N)$ (≈ 0.145 for $D = 5$, as in the figure). This is indicated by the blue curve that starts in the bottom left with signal to sampling ratio $f/f_s = 1 \times 10^{-4}$ and goes up to $f/f_s = 0.49$. The lower

right side of the plain is populated by stochastic signals with high entropy and low complexity. The dashed red line indicates fractional Brownian motion (fBm) with Hurst exponent H ranging from $(0 \leq H \leq 1)$, beginning in the bottom right. Signals below the fBm line are stochastic, and those lying above the fBm line in the upper part of the plane are characterized as chaotic signals. The locations of three chaotic maps, the Lorenz Attractor [106], Schuster Map [107], and Logistic Map [108], are shown across the upper half of the plane; short descriptions of each chaotic signal and the parameters used to generate them are located in the Appendix. Last, experiment shots of the afterglow plasma with no filament present and sampled the same as the experiment signals are shown in the bottom right corner; this demonstrates the stochastic nature of the probe signal in the absence of the filamentary structures.

In all three cases investigated in Fig. 5.24 there is clear evidence of chaotic dynamics; in the case of (c) this is expected from past results [22]. In Fig. 5.24(a) it is observed that the highest complexities occur at a radius between 0.9 cm and 1.3 cm, which corresponds to the peak of the drift-Alfvén wave modes and region of the largest intermittent events. Beyond $r = 1.5$ the signals begin to approach the fBm line and stochastic processes are dominating. A similar outcome is seen at z_2 in Fig. 5.24(b) where the most complex signals are found between $r = 0.2$ cm and 0.7 cm. For the single filament (data collected at z_1) in Fig. 5.24(c), the chaotic dynamics are restricted to $r \leq 0.5$ cm; for larger radii, the location in the CH-plane intersects the fBm line and indicates a strong stochastic nature. The radial extent of the chaotic dynamics in the tri-filament bundle is larger than for the single filament, even when taking into consideration the off-axis filament peaks. In the tri-filament case, the chaotic dynamics dominate up to $2\delta_e$ from the profile peak while in the single filament case the dynamics are stochastically dominated beyond $\sim 1\delta_e$ from the filament centre. This result is in agreement with the enhanced extent of anomalous

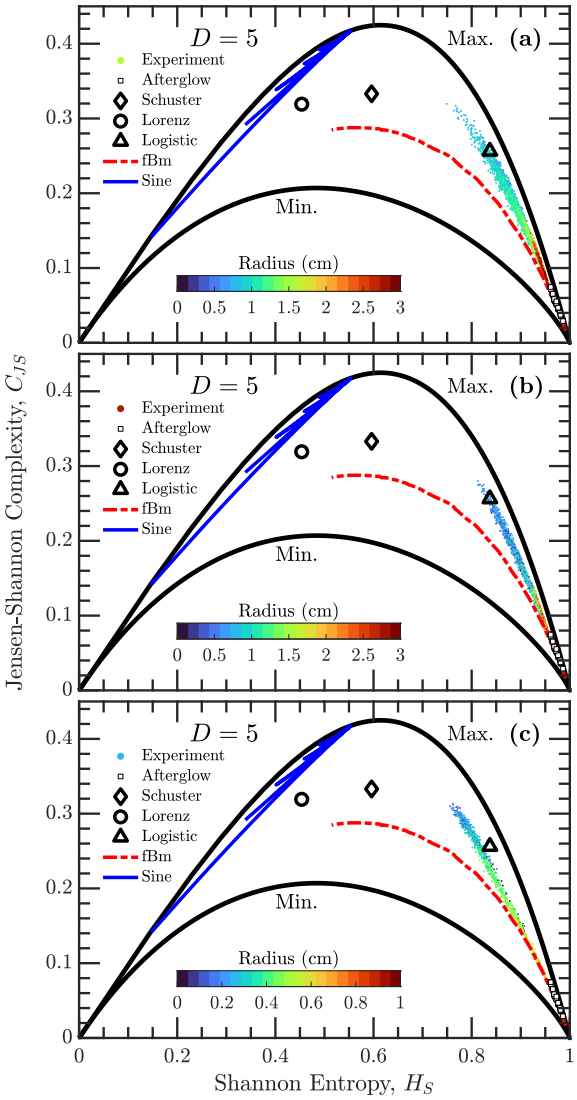

Figure 5.24: Complexity-Entropy plane for (a) z_1, (b) z_2, and (c) single filament data at z_1 with embedding dimentsion $D = 5$. The individual shots of the experiment data are represented by the filled circles, coloured according to radius given in the colorbar. Plasma afterglow shots are denoted by the hollow squares. The location of common chaotic systems are included for reference: the Schuster map (hollow diamond), Lorenz system (hollow circle), and the logistic map (hollow triangle). The dashed red line indicates the location of fractional browning motion with Hurst exponents ranging from 0 to 1. The solid blue line indicates the location of a sine wave with frequency ranging from $f/fs \approx 0.01$ to 0.5.

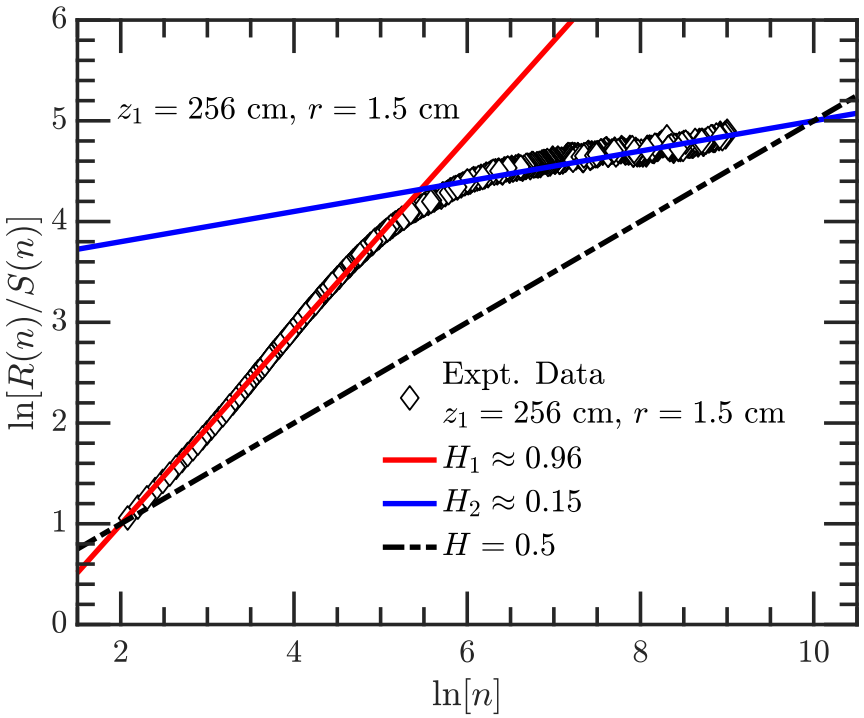

Figure 5.25: Rescaled range estimation of the Hurst exponent at $z_1 = 256$ cm and $r = 1.5$ cm. The two distinct linear regions correspond to two separate Hurst exponents $H_1 \approx 0.96$ and $H_2 \approx 0.15$ given by the red and blue lines, respectively; the dashed line indicates a Hurst exponent of H=0.5 for reference.

transport events in the interacting tri-filament bundle.

A complimentary analysis to the CH-plane is that of the Hurst exponent, which reveals the memory of a time series [101, 109]. Hurst exponents range between 0 and 1 and a Hurst exponent of 0.5 corresponds to a random walk with no predictability of the next occurrence in the series based on previous values, i.e. the series is uncorrelated. When the Hurst exponent is above 0.5 the signal is said to be persistent: an increase will more likely be followed by another increase in the short term, and a decrease is more likely to be followed by another decrease in the short term; the cumulative sum of the series has a tendency to drift far from the initial position. For Hurst exponents less than 0.5 the signal is said to be anti-persistent: increases are more

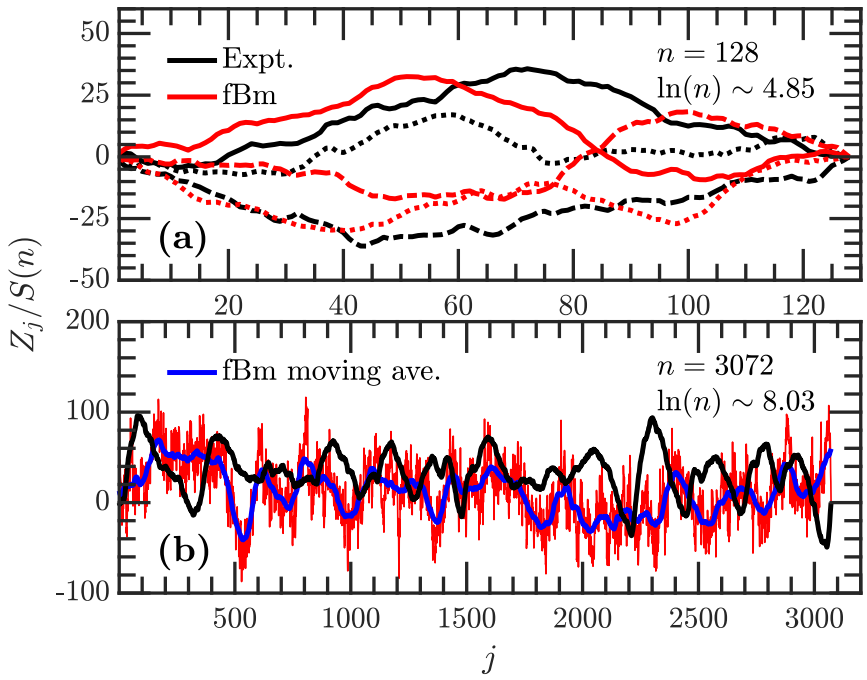

Figure 5.26: Cumulative deviate sum normalized to the standard deviation, $Z_j/S(n)$, of the experiment data (black) compared to fractional Brownian motion (red) with similar Hurst exponents; (a) n = 128 and $H = 0.96$ for the fBm with 3 cases for each in solid, dashed, and dotted lines; (b) n = 3072 and $H = 0.15$ for the fBm, the blue curve indicates the moving average of the fBm over a window of 64 points. The fBm sum in (b) is scaled such that the averaged fBm has the same rescaled range as the experiment.

likely to be succeeded by decreases, and vice versa; the cumulative sum of the series tends to revert to the initial position. The Hurst exponent can be estimated using the rescaled range analysis of a time series $x = \{x_1, ..., x_N\}$ of length N. The time series is first divided into time arrays $y = \{y_1, ..., y_n\}$ of length n with $8 \leq n \leq N$; for example, if $N = 8192$ and $n = 8$ there will be 1024 arrays y of length n, and this is repeated for all n. The cumulative deviate series $\{Z_j\}$ is computed for each subarray,

$$Z_j = \sum_{i=1}^{j} y_i - \bar{y}, \quad j = 1, ..., n \tag{5.10}$$

where $\bar{y}$ is the mean of the array y and we note that by construction the deviate series always ends at zero. The range $R(n)$ follows from the extrema of the cumulative deviate series,

$$R(n) = \max(Z_1, ..., Z_n) - \min(Z_1, ..., Z_n) \tag{5.11}$$

and the rescaled range is $R(n)/S(n)$, where $S(n)$ is the standard deviation of the subarray y. The final rescaled range is then the ensemble average of the estimates for each array of length n from all the shots at one position. The rescaled range follows a power law of the form $R(n)/S(n) \propto n^H$, and once the spectrum of $R(n)/S(n)$ is known the Hurst exponent can be calculated from a linear fit to $\ln[R(n)/S(n)]$ as a function of $\ln[n]$.

Fig. 5.25 shows the estimation of the Hurst exponent for a time series at $r = 1.5$ cm and z_1. The $\delta I_{\text{sat}}/I_{\text{sat}}$ time series used in the Hurst analysis are the same as those used for the CH-plane and pulse reconstruction, i.e. $N = 8192$ points beginning at $t = 3$ ms and ending around 10 ms, with 10 shots at each position. In the rescaled range analysis it is obvious that there are two distinct linear regions thereby indicating the presence of multiple Hurst exponents, defined as H_1 and H_2, corresponding to variable persistent or anti-persistent tendencies over different time scales. The observation of multiple Hurst exponents has also been documented in sunspot data and standard chaotic systems [110]. The Hurst exponent for short time scales indicates the signal is highly persistent ($H_1 \approx 0.96$) while on longer time scales it is the opposite and strongly anti-persistent ($H_2 \approx 0.15$). All locations within the 2D planes at z_1 and z_2 are observed to have two Hurst exponents with the transition from one Hurst exponent to the other typically occurring at $\ln[n] \sim 5$. Taking the time-step into consideration this separates the two scales at ~ 0.3 ms, with H_1 dominating the

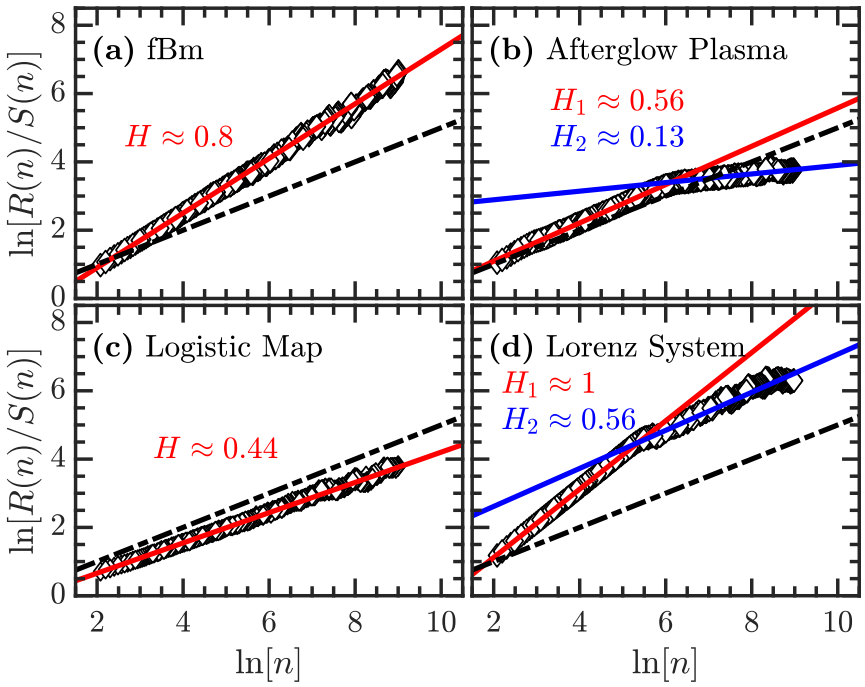

Figure 5.27: Hurst exponents calculated using rescaled range analysis for different signals; (a) fractional Brownian motion, (b) afterglow plasma shots, (c) Logistic map, (d) z component of Lorenz system. Both chaotic and stochastic systems are shown to have either one or two Hurst exponents.

time-series correlation on shorter time scales and H_2 dominating dynamics on longer; this transition scale is on the same order as the longest drift-Alfvén wave periods.

To make clear the nature of multiple Hurst exponents in a time series the cumulative deviate sum for $n = 128$ and $n = 3072$ are shown in Fig. 5.26(a) and (b), corresponding to the H_1 and H_2 time scales, respectively. In (a) Z_j for several of the $n = 128$ arrays is shown along with the same measure for fBm signals having $H = 0.96$; it is clear that on this short time scale the experimental signal persistence is indistinguishable from a signal with only a single Hurst exponent. In (b) a single array with $n = 3072$ is shown along with a (scaled) fBm signal having $H = 0.15$. The difference over the long time scale is evident; the deviate sum of the fBm shows anti-persistent behaviour at both short and long time scales, while the experimental

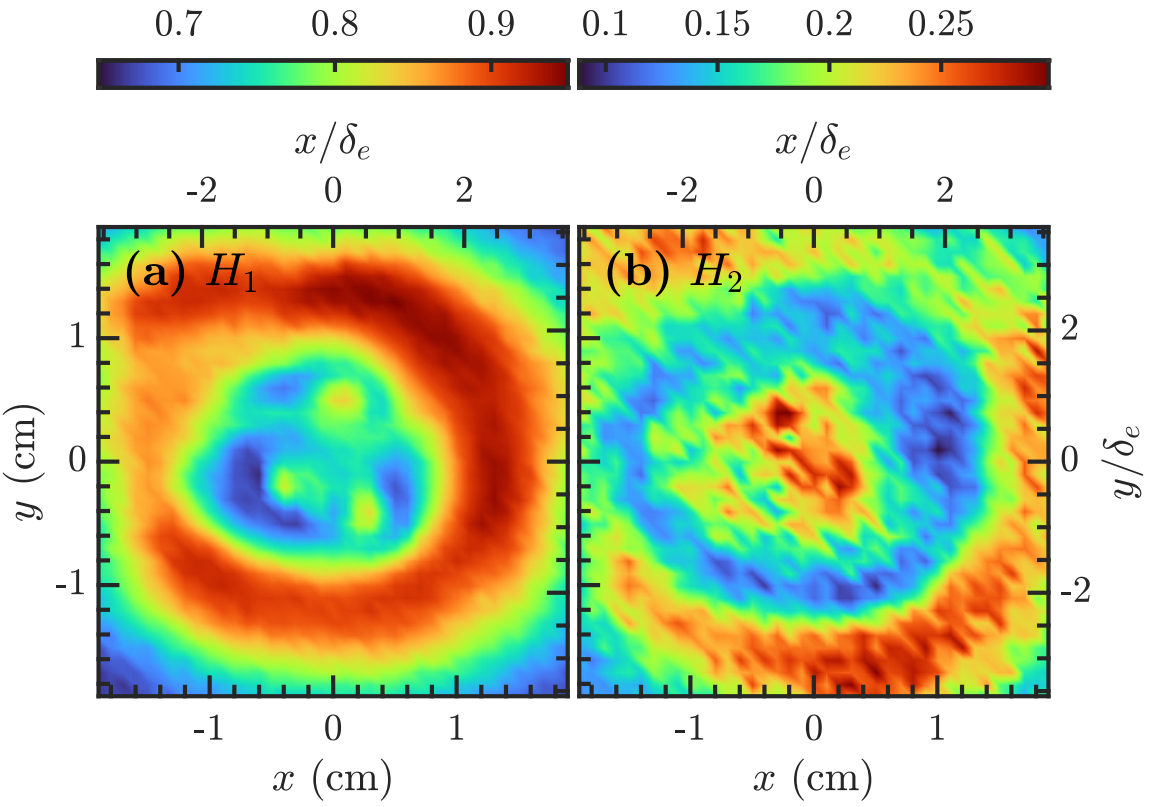

Figure 5.28: Hurst exponents, (a) H_1 and (b) H_2, for transverse planes at z_1 estimated using rescaled range analysis.

signal is only mean reverting on a long time scale and has short periods of persistence. Applying a moving average window of 64 points to the fBm deviate series (blue line) results in a signal that closely resembles the experiment and shows the similar long-term behaviour of both the single and double Hurst exponent series.

In Fig. 5.27 the rescaled range analysis of different dynamical systems are investigated. The stochastic fBm series with $H = 0.8$ used in Fig. 5.27(a) is defined by a single Hurst exponent as expected and the resulting Hurst exponent is nearly identical to that used to synthesize the data. An experimental stochastic signal, that of the afterglow plasma, is investigated in Fig. 5.27(b). Here we observe a stochastic signal

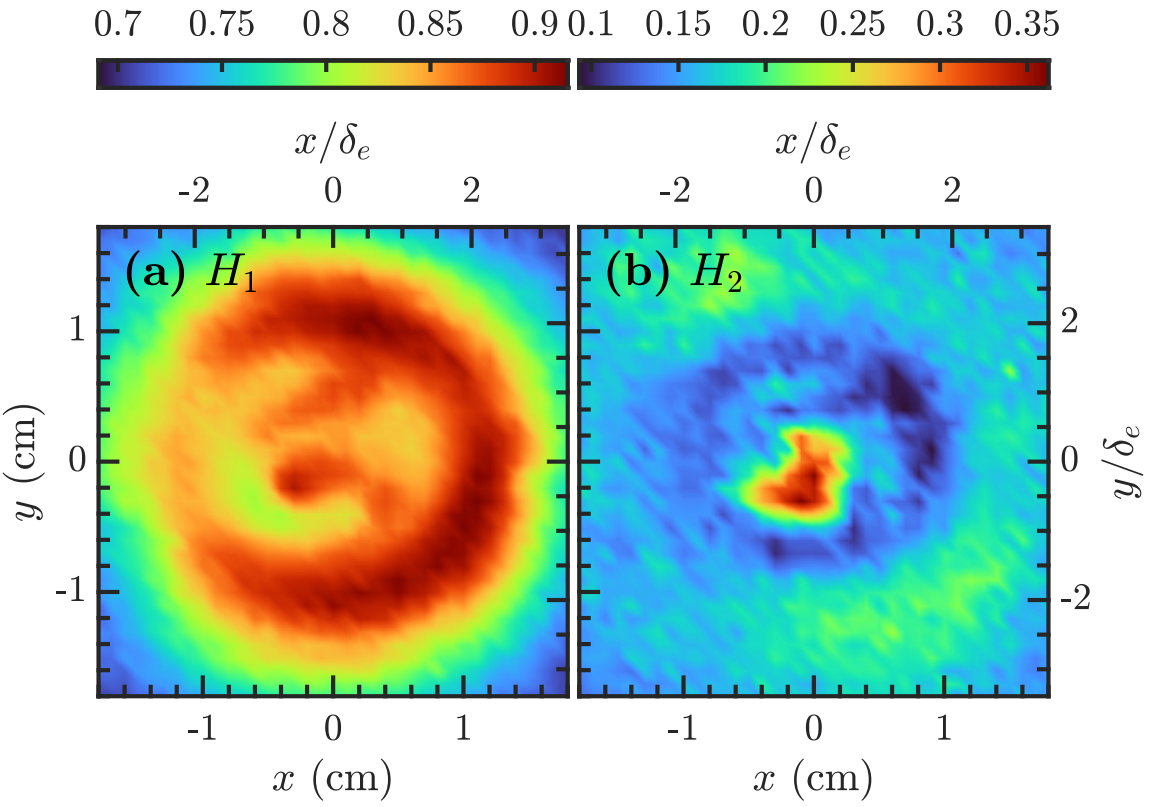

Figure 5.29: Hurst exponents, (a) H_1 and (b) H_2, for transverse planes at z_2 estimated using rescaled range analysis.

with two Hurst exponents; it is a nearly uncorrelated series tending to some persistence on a short time scale and a highly anti-persistent series on a long-term scale; the sharp transition occurs at a time scale on the order of 0.6 ms. The chaotic Logistic map series used in the CH-Plane analysis is shown in Fig. 5.27(c) and is observed to have a single Hurst exponent with slight anti-persistence; we note that varying the r parameter of the logistic map (see Appendix) can produce a wide range of Hurst exponents and both single and double cases. Last in Fig. 5.27(d) is the rescaled range analysis of the z-component of the Lorenz attractor and is characterized by a sharp transition between very high persistence on a short term scale and being nearly uncorrelated on a long term scale; a periodic signal has Hurst exponent of 1, the well

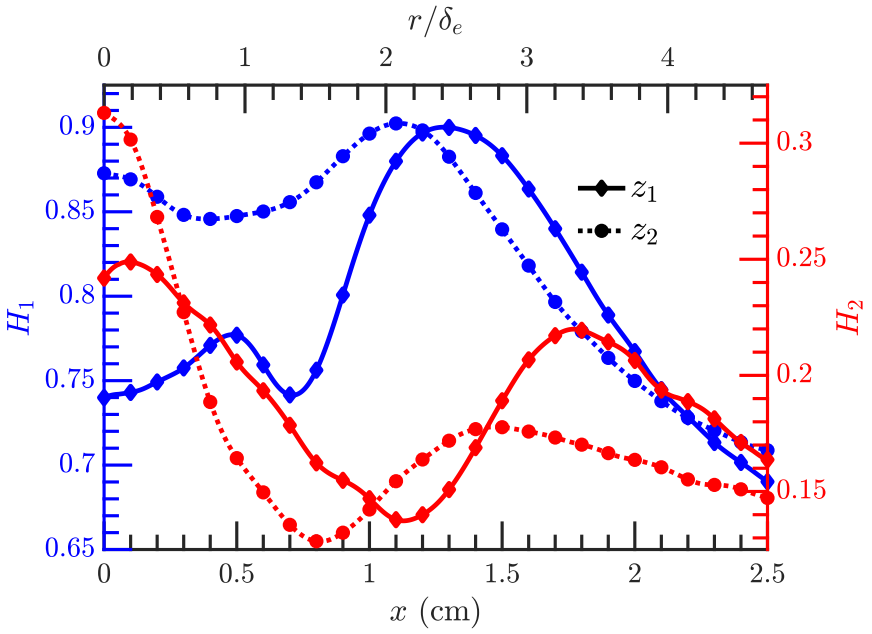

Figure 5.30: Radial profile of azimuthally averaged Hurst exponents from the planes in Fig. 5.28 and Fig. 5.29. The blue axis on the left is H_1 and the red axis on the right is H_2; the Hurst exponents at z_1 and z_2 are the solid diamond lines and the dotted circle lines, respectively. Note that for $r < 0.8$ the 2D plane has only quasi-symmetry for H_1 at z_1 (Fig. 5.28(a)).

known Lorenz attractor system has oscillatory orbits about the two attractive points and this periodic nature is observed in the H_1 Hurst exponent. Overall it is clear that both stochastic and chaotic dynamical systems can have a range of Hurst exponent values and be characterized by one or more Hurst exponents.

The results of the rescaled range analysis applied to the 2D planes at z_1 and z_2 are presented in Fig. 5.28 and Fig. 5.29, respectively; azimuthally averaged radial profiles are also shown in Fig. 5.30. At both z_1 and z_2 the short time scale Hurst exponent, H_1, indicates the system has persistent behaviour across the 2D plane. Similarly, the Hurst exponent, H_2, characterizes the long-timescale nature of the filament dynamics as anti-persistent.

For H_1 at z_1, Fig. 5.28(a) shows there is a clear signature of the three filaments

making up the bundle with Hurst exponents approaching $H_1 \approx 0.85$ on the filament maxima. The filaments are surrounded by a region with Hurst exponents on the order of $H_1 = 0.7$ to 0.8 up to $r \lesssim 0.8$ cm. On the gradient region $r = 0.8$ cm to 1.9 cm the Hurst exponent is symmetric about the bundle and reaches a maximum at $r \approx 1.2$ cm with $H_1 \approx 0.9$, indicating highly persistent series memory that is correlated with the location of the Lorentzian pulses, maximum PDF skewness, drift-Alfvén waves, and the highest complexity in the CH-plane. Beyond $r \sim 1.9$ cm the Hurst exponent rapidly decreases to $H_1 \sim 0.7$ and it can be presumed that far from the center of the filament bundle the Hurst exponent approaches the short time scale Hurst exponent of the afterglow plasma, $H_1 \approx 0.56$.

For H_2 at z_1, Fig. 5.28(b) has little evidence of distinct filaments and the result is nearly azimuthally symmetric at all radii. The Hurst exponent initially decreases from the center region and reaches a local minimum at $r \approx 1.1$ cm, before increasing again to a local maximum at $r \approx 1.8$ cm. The exponent then decreases far from the bundle and again likely approaches the long-term Hurst exponent of the afterglow, $H_2 \approx 0.13$ (Fig. 5.27(b)). The local minima in H_2, a maximum in anti-persistence, is in the same vicinity as the local maxima in persistence for H_1 and the rest of the features of the time series.

The results at z_2 in Fig. 5.29 have centrally peaked Hurst exponents followed by local extrema on the gradient. The radius of local maxima in H_1 at $r = 1.1$ cm is larger than other features at z_2, namely, the amplitude PDF has maximum skewness at $r = 0.7$ cm, the drift waves peak at $r \approx 0.5$; however, there is evidence of Lorentzian shaped pulses up to $r = 1.5$ cm, and the CH-plane indicates stochastically dominated signals only beyond $r \approx 1.5$ cm. For H_2 the local minimum occurs at $r = 0.8$ cm and is in agreement with the maxima in the drift-Alf'vén waves and PDF. In both H_1 and H_2 the profiles again appear to approach the afterglow plasma values for large radii,

as was seen at z_1.

Evident in Fig. 5.30 is that a feature of the double Hurst exponent analysis is a radial asymmetry between the H_1 and H_2 profiles at each axial location. This is seen in the offset locations of local extrema and qualitative structure of the profiles that are quite different; in particular, we again note the clear filament signatures at z_1 in H_1 that are non-existent in H_2. The radial asymmetry of the Hurst exponents is further evidence that there are two distinct time scales of the underlying dynamics that lead to the persistence and anti-persistence of the time series. Our interpretation of these time scales is the bursty nature of intermittent turbulence is driving the persistence on a short time scale, but the stability of the profiles necessitates an anti-persistence on a long time scale. An investigation of Hurst exponents in other LAPD experiments involving merging flux ropes [101, 102] and collapses (avalanches) of ring-shaped pressure profiles [70], as well as experiments of turbulence and chaos in other plasma devices and in space, could yield similar double Hurst exponents and division of time scales that could help interpret results.

5.3 Driven Multi-Filament Experiments

In this section we discuss some results of preliminary experiments involving source modulation with three filaments in the same configuration discussed in Section 5.2. The introduction of source modulation to one of the filaments in the bundle creates a situation where the driving signal can easily couple to the gradient. In the single filament driving seen in Chapter 4 the symmetric $m = 0$ driving equally perturbs the gradient and does not drive drift-Alfvén waves. However, in the tri-filament bundle, the driving of one of the filaments creates an asymmetric azimuthal perturbation that can couple to higher m numbers. In these exploratory experiments the driving signal is at $f = 16$ kHz on the bottom left filament at ($x \sim -0.4$ cm,$y \sim -0.3$ cm) in Fig.5.11(b) and is turned on continuously 1 ms after the filaments are generated.

In Fig. 5.31(a) the evolution of ensemble-averaged plasma shots at z_2 and a radius of $r = 0.6$ cm are depicted with time on the vertical axis and azimuthal angle on the horizontal. What can be instantly noticed is the shot-to-shot coherency of the 16 kHz signal, it is important to note that without a driver the ensemble-averaged shots would show nearly no activity due to the variable phase of fluctuations. Beginning at $t = 1$ ms, when the driver is activated, there is a transient and slowly rotating $m = 1$

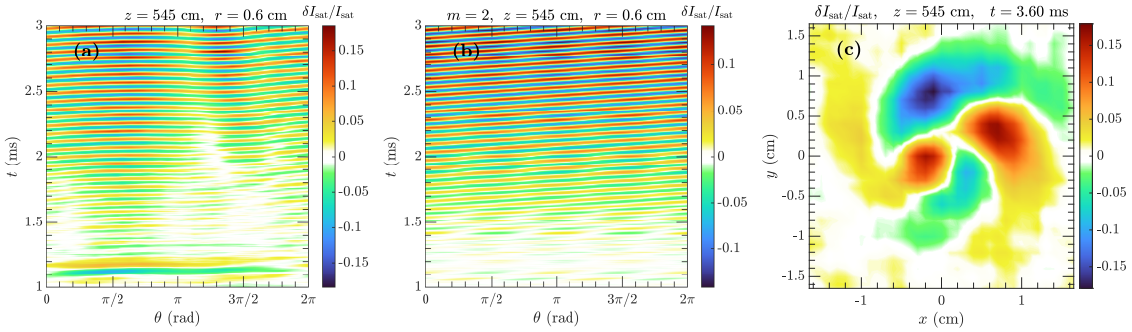

Figure 5.31: (a) Space-time plot of the fluctuation amplitude at a radius of $r = 0.6$ cm. (b) Same format as (a) with each temporal slice decomposed into the $m = 2$ mode. (c) Observed wave pattern at $t = 3.60$ ms.

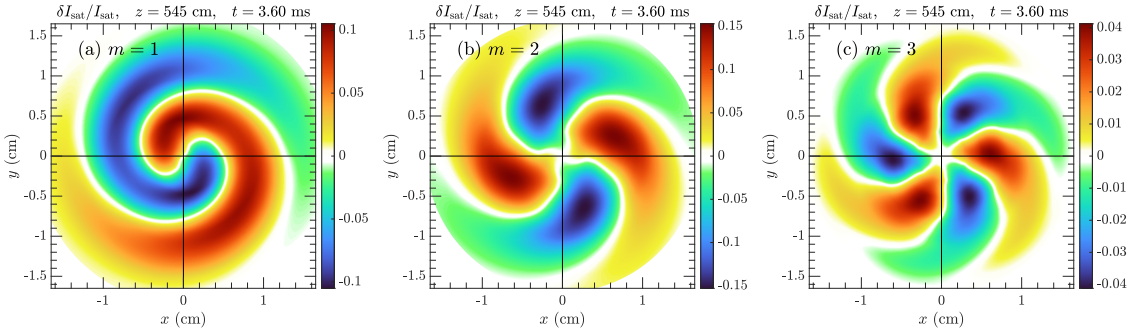

Figure 5.32: Azimuthal mode decompositions of a time slice of the average planes at $t = 3.6$ ms (a) m=1, (b) m=2, (c) $m = 3$.

mode that has a period double that of the driver. This mode quickly dissipates after less than two oscillations and a low amplitude 16 kHz modulation sets in. These driven modes ramp up slowly over the next 1.5 ms to become coherent travelling wave modes. In Fig. 5.31(b) the $m = 2$ mode has been isolated and the continual growth of the mode is obvious. The mode pattern at $t = 3.60$ ms is shown in Fig. 5.31(c). An $m = 0$ like mode is observed to be located near the position of the driven filament, this off-axis perturbation of the whole bundle at θ between π and $3\pi/2$ then grows into the observed wave pattern. A similar outcome is observed at z_1 but the excited pattern is more complex; this is likely due to the filament bundle being merged at z_2 and the radial profile having high azimuthal symmetry when compared to z_1.

The mode pattern at $t = 3.60$ ms can be decomposed into symmetric modes in the same way the cross-correlations in the previous sections were decomposed; however, we again note this is a time slice of the ensemble-averaged plane and no reference probe or transform to the frequency domain is necessary. Without a driver, each dc shot quickly experiences phase slippage and the ensemble averaging removes the wave pattern. Figs. 5.32(a), (b), and (c) show the decomposition into modes $m = 1$, 2, and 3, respectively. Each of these is most likely a drift-Alfvén wave mode and each has a frequency equivalent to the driver at $f = 16$ kHz. The wave modes can be compared

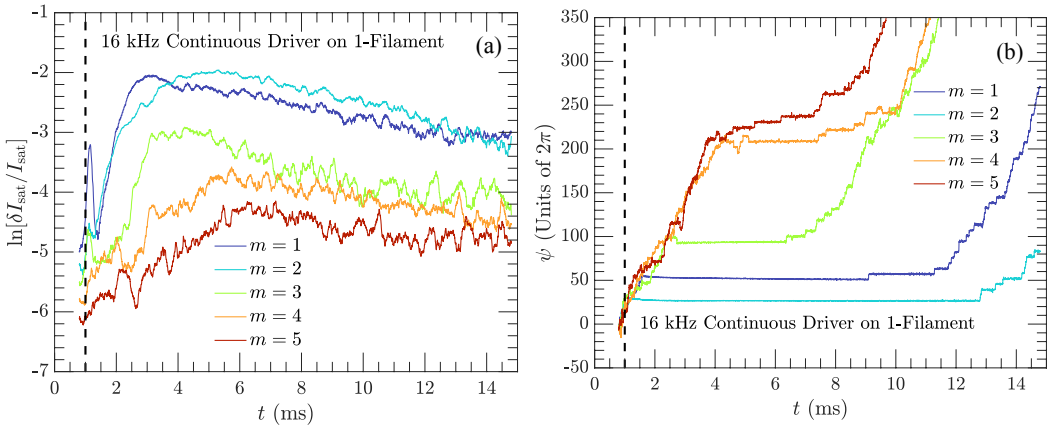

Figure 5.33: (a) Amplitude growth of first 5 modes. (b) Phase synchronization of modes with driver signal.

with the 14 kHz decomposition of the naturally excited modes in Fig. 5.14(g–i). The natural $m = 1$ and $m = 3$ modes have a similar structure to the driven modes but have a smaller radial extent; this indicates a coupling to these natural modes that are driven further unstable by the applied perturbation.

In Fig. 5.33 shows the temporal evolution of the amplitude of the decomposed modes and the phase difference, ψ, of each mode with the driver signal in (a) and (b), respectively. When the phase difference is constant it indicates synchronization of the modes with the driver. At the application of the driver, the transient $m = 1$ excitation is observed along with a smaller transient in the $m = 3$. The $m = 1$ and $m = 2$ modes show the strongest growth and synchronization, but there is intermittent synchronization up to the $m = 5$ mode. Beyond $m = 5$ the modes show some growth but are not coherent and do not synchronize. The exponential growth rates of the $m = 1$ and $m = 2$ modes are nearly identical up to $t = 2$ ms when the growth slows and the $m = 2$ grows at a lower rate than $m = 1$. The $m = 3$ growth rate is initially low and the same as the $m = 3$ and $m = 4$ growth rates, but at $t = 2.5$ ms the growth rate increases to nearly the initial growth rates of the $m = 1$ and $m = 2$ modes. The

synchronization is closely correlated with the amplitude of the modes. This interplay of the growth rates and synchronization is a signature of nonlinear coupling between drift waves [56]. The modes all eventually saturate and then decay slowly throughout the rest of the shot as they desynchronize, even though the driver remains active. The desynchronization of the modes initially occurs as an oscillatory phase slippage known as periodic pulling; the Kuramoto model of nonlinearly coupled oscillators has been shown to accurately depict the coupling among drift wave modes exhibiting this phenomenon [56]. The frequencies of the natural modes decrease slowly throughout the plasma shot and it could be that the driving frequency is too far from the natural frequency to effectively drive the modes.

We now discuss the relation of these results to the rest of the experiments. First, we note that the ac shots for the tri-filament configuration still exhibit exponential frequency spectra and intermittent PDFs nearly identical to those in Figs. 5.16 and 5.17. This indicates that while the driver can synchronize to these wave modes the experiment remains largely unchanged. Second, the appearance of mode patterns in the spatial reconstruction of the intermittent event already indicates a level of synchronization among the drift waves. The driven regime may provide a convenient method for synchronizing the modes shot-to-shot to more easily probe the turbulence if the coupling can be optimized. Introduction of modulation to all three sources may enable extreme growth or damping of the modes by varying the phase on each. Last, the modulated sources are already known to drive thermal waves. We can observe that the driver can couple to the tri-filament gradient because of the asymmetry, however, it is not clear what role thermal waves play in coupling beyond perturbing the gradient. The phase shift between z_1 and z_2 on the driven filament should be investigated over a frequency and amplitude range to determine where it matches the dispersion for thermal waves or drift waves and study the coupling between them.

CHAPTER 6.

Summary and Future Work

In this thesis we reported on the progress towards two plasma science goals, repeated here for clarity: (i) development of diagnostic methods capable of making direct measurements of thermal transport coefficients in magnetized plasma; (ii) improved understanding of the dynamics of enhanced thermal transport associated with filamentary structures occurring in natural and laboratory plasmas. The experiments presented were conducted at the Large Plasma Device using small electron beam heat sources to generate plasma pressure filaments in a cold, quiescent, magnetized plasma. Modulation of a single heat source was used to investigate driven thermal waves in axial and cross-field configurations. Two models for the thermal wave field in a magnetized plasma were developed in support of these experiments. The interaction among multiple filaments was characterized using three filamentary structures in a tight bundle. A statistical analysis of the transport fluctuations identified intermittent transport events and underlying deterministic chaotic dynamics.

In Chapter 2 we described the operation of the Large Plasma Device and the associated diagnostics. An operational amplifier and waveform generator were used to apply an oscillatory bias to the crystal cathodes and generate a modulated heat source. The biasing circuitry was designed to allow up to three crystals to be operated simultaneously and controlled independently. To establish continuity of these experiments with previous renditions we presented results that replicated the past conclusions and summarized the basic evolution of a single filamentary structure. We

have observed peaked temperature and density profiles along with an electric potential well. The latter two quantities were not understood in detail in previous filament experiments. The filament was observed to undergo a period of classical transport and then the development of a low-frequency thermal mode and high-frequency drift-Alfvén modes driven by the temperature gradient. The growth of the drift-Alfvén waves caused a transition to an anomalous cross-field transport regime characterized by an exponential frequency spectrum. We have presented evidence that the thermal wave and drift-Alfvén wave are coupled.

6.1 Thermal Wave Modelling

Chapter 3 presented two models used to describe the thermal wave field in a magnetized plasma. The first model used a Green function approach to solve the two-dimensional heat equation with azimuthal symmetry and homogeneous thermal conductivities. Boundary conditions for semi-infinite and laterally-infinite cases were compared. The axial boundary in the laterally-infinite model demonstrated thermal wave interference effects as a result of confined thermal wave power. The homogeneous model has several limitations in the ability to describe the experiment, namely, it does not account for the inhomogeneous temperature profile of the pressure profile and can only be used to model the phase shift over a short axial distance. The second model used a Hamilton-Jacobi approach to solving the heat equation in the form of a thermal harmonic oscillator. A method for transforming the space-dependent heat equation in one dimension to the form of a space-independent harmonic oscillator was presented using a canonical transformation in extended phase space. The solution for an exponential profile in the thermal diffusivity was shown to describe the interference features observed in the cross-field thermal wave field. The extension of the model to two dimensions for anisotropic conductivities was described using the de Donder and

Weyl Hamiltonian.

6.2 Thermal Wave Experiments

The experiments presented in Chapter 4 use the modulated electron beam heat source to drive thermal waves and were divided into axial and radial experiments. In the axial experiments, a series of sinusoidal perturbations were added to the discharge bias on the crystal cathode. Measurements of the fluctuations in plasma density and electron temperature demonstrated the modulated heat source drives oscillations in the temperature and not the density. The amplitude and phase of the driven temperature oscillations were sampled at three axial locations across a range of frequencies. The axial phase shift was used to verify the waves are thermal diffusion waves through a comparison with the homogeneous model. Thus, the ability to stimulate the excitation of thermal waves in a magnetized plasma using a modulated electron beam heat source has been demonstrated. The diagnostic potential of thermal waves was illustrated by comparing the thermal diffusivity measured using thermal waves with classical transport predictions. A resonance was observed in the thermal wave field at a frequency matching the natural thermal mode and a second, smaller resonance was observed at a higher frequency. Measurement of the filament length confirmed the resonances correspond to quarter-wave and half-wave conditions. A broadband pulse applied during the cathode discharge excited a ringing of the natural resonance of the filament. The resonator feature of the filament allows for an alternate way to obtain the thermal diffusivity.

In the cross-field experiments, an improvement to the measurement technique was made by comparing probe measurements of floating potential and ion saturation current. The same fluctuation features observed in ion saturation current were shown to exist in floating potential but with a significantly enhanced signal-to-noise ratio. The

increased sensitivity to the driven fluctuations facilitated the high-precision measurement of the cross-field structure of the thermal wave field. The pulse train technique was used to extract the thermal wave field in four transport regimes of the filament: classical, drift-Alfvén wave growth, transition, and turbulent phases. The results demonstrated the cross-field thermal wave field can distinguish between anomalous and classical radial thermal transport regimes. The inhomogeneous model was applied to the classical thermal wave field and confirmed the observed thermal wave interference features are a result of the inhomogeneous temperature and density of the pressure filament.

6.3 Multi-Filament Experiments

In Chapter 5 we presented results using three localized heat sources mounted on probes for ease of variable separation and positioned in a triangular pattern. When the sources were separated by a distance greater than a few electron skin depths they act as independent filaments, with drift-Alfvén modes growing on each of their respective gradients. When arranged more tightly enhanced $\mathbf{E} \times \mathbf{B}$ mixing relaxed the inner gradient of the bundle and depleted the density. The fluctuations of the structure were shown to be highly turbulent; identified within the turbulence were coherent drift-Alfvén modes driven by the outer gradient that was shown to exhibit quasi-symmetry azimuthally. Linear stability analysis of the profiles predicted frequencies and mode structures that agreed well with the observed drift modes. Fourier decomposition was used to identify coupling between the drift-Alfv en modes that are the source of the turbulence.

A statistical analysis of the turbulent time series was conducted to investigate the nature of the underlying dynamics. The probability distribution function showed the

turbulence is characterized by intermittent transport events. These events were identified as Lorentzian-shaped pulses that generate a broadband exponential frequency spectrum and are a characteristic of chaotic systems. Conditional averaging of the data collection plane using a reference probe facilitated a spatiotemporal reconstruction of an intermittent event. The resulting pulse was observed to be generated by an interaction betwixt the drift-Alfvén modes. The time series were analyzed using the complexity-entropy plane and revealed the signals are generated by inherently deterministic and chaotic processes. The Hurst exponent of the fluctuations was estimated using rescaled range analysis and a short time-scale persistent memory and long time-scale anti-persistent memory were identified. Last, modulation of a single filament in the multi-filament configuration demonstrated asymmetric perturbation of the outer gradient and the ability to synchronize with and drive the growth of several drift-Alfvén modes.

6.4 Future Work

The work presented herein offers many avenues for future investigation. First, the structure of the thermal wave field in the plasma filament is highly complex and advanced models are needed to progress towards accurate thermal wave diagnostic techniques. The development of a two-dimensional, inhomogeneous model of thermal waves in a magnetized plasma using the de Donder and Weyl Hamilton-Jacobi is a natural extension of the modelling presented in Chapter 3. In time, thermal wave field inversion techniques, or tomography, may be developed where the conductivity profile of the plasma filament could be reconstructed using only measurements from the edge of the filament [32]. This would, in theory, also apply to large plasma columns such as the LAPD main plasma or a toroidal plasma device. An area to explore is the theoretical applications of thermal waves in the fusion regime; the

increased anisotropy created by extreme temperatures and high magnetic fields may yield interesting thermal wave interference phenomena that could be exploited in diagnostics.

Second, LAPD experiments involving modulated heat sources offer a controlled environment in which to continue studying thermal wave phenomena in the plasma regime. The coupling of the thermal wave and drift-Alfvén wave should be investigated as it is obvious this occurs for both the natural and driven thermal waves. A likely mechanism for the coupling is the modulation of the gradient by the thermal wave. The origin of the free energy source for the natural thermal resonance remains elusive and the driven thermal waves could be used to probe this mechanism. Additionally, the LAPD is equipped with a larger disk-shaped lanthanum hexaboride (LaB_6, similar to cerium hexaboride) cathode measuring 8.25 cm in diameter. Driving thermal waves with this source could offer an opportunity to validate thermal wave models at higher temperatures. The larger column is less susceptible to probe perturbations and the impact of plasma advection on the thermal wave field could be studied in detail using control of the azimuthal shear flow [92]. Last, the thermal wave interference structures observed in the cross-field experiments also likely have axial variation. A large, two-dimensional (r, z) data set could be acquired using probes to collect radial lines at each port along the length of the filament. This would offer an opportunity to validate thermal wave models across the entire inhomogeneous structure.

Third, the multi-filament configurations are highly complex and offer nearly endless variations for further study of filament interactions and turbulence. A controlled study of two filaments has already been collected and analysis of this data set should be carried out by future students and/or researchers. Some of the analysis has already been completed. Perhaps the most intriguing result of the multi-filament experiments

is the ability to couple to the drift-Alfvén waves. The experiments conducted to date have only been exploratory and a systematic study of the driving represents a logical next step. Studies involving modulation of only one of the filaments of the bundle can be conducted to better understand the coupling mechanism and limitations. Properly phased modulation of all three sources at once could be used to drive large perturbations resonantly or damp the natural drift-Alfvén modes. Additionally, the introduction of a single crystal source to the edge of the large LaB_6 source could provide the ability to asymmetrically perturb the gradient and synchronize to the large drift-Alfvén modes observed there[111].

Finally, we note that diffusion wave fields offer a rich area of study in plasma physics and should not be restricted to the basic plasma experiments of the LAPD. The materials science community has successfully developed experimental techniques and models that can readily be adapted to the plasma regime. Experimental and theoretical efforts should be made to better understand these transport phenomena and the role they can play in both space and laboratory plasmas.

References

[1] H. Alfvén, "On the filamentary structure of the solar corona," in *The Solar Corona*, edited by JOHN W. EVANS (Academic Press, 1963) pp. 35 – 38.

[2] S. Parenti, "Solar prominences: Observations," Living Rev. Sol. Phys. **11**, 1 (2014).

[3] J. R. Wygant, A. Keiling, C. A. Cattell, M. Johnson, R. L. Lysak, M. Temerin, F. S. Mozer, C. A. Kletzing, J. D. Scudder, W. Peterson, C. T. Russell, G. Parks, M. Brittnacher, G. Germany, and J. Spann, "Polar spacecraft based comparisons of intense electric fields and poynting flux near and within the plasma sheet-tail lobe boundary to uvi images: An energy source for the aurora," J. Geophysical Res. **105**, 18675 (2000).

[4] Y.I. Galperin, "Multiple scales in auroral plasmas," J. Atmos. Sol.-Terr. Phys. **64**, 211 – 229 (2002).

[5] J. D. Nichols, J. T. Clarke, J. C. Gérard, and D. Grodent, "Observations of jovian polar auroral filaments," Geophysical Research Letters **36** (2009).

[6] N. J. Lopes Cardozo, F. C. Schüller, C. J. Barth, C. C. Chu, F. J. Pijper, J. Lok, and A. A. M. Oomens, "Plasma filamentation in the rijnhuizen tokamak rtp," Phys. Rev. Lett. **73**, 256 (1994).

[7] H Wobig, "On radiative density limits and anomalous transport in stellarators," Plasma Phys. Control. Fusion **42**, 931–948 (2000).

[8] M. N. A. Beurskens, N. J. Lopes Cardozo, E. R. Arends, C. J. Barth, and H. J. van der Meiden, "Filamentation in the rtp tokamak plasma," Plasma Phys. Control. Fusion **43**, 13 (2001).

[9] W Horton, B Hu, J Q Dong, and P Zhu, "Turbulent electron thermal transport in tokamaks," New J. Phys. **5**, 14–14 (2003).

[10] G. Serianni, M. Agostini, V. Antoni, R. Cavazzana, E. Martines, F. Sattin, p. Scarin, E. Spada, M. Spolaore, N. Vianello, and M. Zuin, "Coherent structures and transport properties in magnetized plasmas," Plasma Phys. Control. Fusion **49**, B267 (2007).

[11] S. I. Braginskii, "Reviews of plasma physics," in *Reviews of Plasma Physics*, Vol. 1, edited by M. A. Leontovich (Consultants Bureau, New York, 1965) p. 205.

[12] W. Gekelman, P. Pribyl, Z. Lucky, M. Drandell, D. Leneman, J. Maggs, S. Vincena, B. Van Compernolle, S. K. P. Tripathi, G. Morales, T. A. Carter, Y. Wang, and T. DeHaas, "The upgraded large plasma device, a machine for studying frontier basic plasma physics," Rev. Sci. Instrum. **87**, 025105 (2016).

[13] G. J. Morales, J. E. Maggs, A. T. Burke, and J. R. Peñano, "Alfvénic turbulence associated with density and temperature filaments," Plasma Phys. Control. Fusion **41**, A519 (1999).

[14] A. T. Burke, J. E. Maggs, and G. J. Morales, "Observation of simultaneous axial and transverse classical heat transport in a magnetized plasma," Phys. Rev. Lett. **81**, 3659 (1998).

[15] A. T. Burke, J. E. Maggs, and G. J. Morales, "Experimental study of fluctuations excited by a narrow temperature filament in a magnetized plasma," Phys. Plasmas **7**, 1397 (2000).

[16] A. T. Burke, J. E. Maggs, and G. J. Morales, "Experimental study of classical heat transport in a magnetized plasma," Phys. Plasmas **7**, 544 (2000).

[17] A. T. Burke, J. E. Maggs, and G. J. Morales, "Spontaneous fluctuations of a temperature filament in a magnetized plasma," Phys. Rev. Lett. **84**, 1451 (2000).

[18] D. C. Pace, M. Shi, J. E. Maggs, G. J. Morales, and T. A. Carter, "Spontaneous thermal waves in a magnetized plasma," Phys. Rev. Lett. **101**, 035003 (2008).

[19] D. C. Pace, M. Shi, J. E. Maggs, G. J. Morales, and T. A. Carter, "Exponential frequency spectrum and lorentzian pulses in magnetized plasmas," Phys. Plasmas **15**, 122304 (2008).

[20] D. C. Pace, M. Shi, J. E. Maggs, G. J. Morales, and T. A. Carter, "Exponential frequency spectrum in magnetized plasmas," Phys. Rev. Lett. **101**, 085001 (2008).

[21] J. R. Peñano, G. J. Morales, and J. E. Maggs, "Drift-alfvén fluctuations associated with a narrow pressure striation," Phys. Plasmas **7**, 144 (2000).

[22] J. E. Maggs and G. J. Morales, "Permutation entropy analysis of temperature fluctuations from a basic electron heat transport experiment," Plasma Phys. Control. Fusion **55**, 085015 (2013).

[23] A. Mandelis, *Diffusion-Wave Fields: Mathematical Methods and Green Functions* (Springer, New York, 2001) p. 2.

[24] A. J. Ångström, "Neue methode, das wärmeleitungsvermögen der körper zu bestimmen," Annalen der Physik **190**, 513 (1862).

[25] A. Mandelis, "Diffusion waves and their uses," Physics Today **53**, 29 (2000).

[26] "Center for advanced diffusion-wave and photoacoustic technologies," (2021).

[27] J. Shen and A. Mandelis, "Thermal wave resonator cavity," Rev. Sci. Instrum. **66**, 49999 (1995).

[28] J. Shen, A. Mandelis, and B. D. Aloysius, "Thermal-wave resonant-cavity measurements of the thermal diffusivity of air: A comparison between cavity-length and modulation-frequency scans," Int. J. Thermophys. **17**, 1241 (1996).

[29] D. Dadarlat, M. Streza, O. Onija, C. Prejmerean, L. Silaghi-Dumitrescu, N. Cobirzan, and K. Strzałkowski, "Complementary photothermal techniques for complete thermal characterization of porous and semi-transparent solids," J. Therm. Anal. Calorim. **119**, 301 (2015).

[30] J. A. Balderas-López and A. Mandelis, "Simple, accurate, and precise measurements of thermal diffusivity in liquids using a thermal-wave cavity," Rev. Sci. Instrum. **72**, 2649 (2001).

[31] J. A. P. Lima, E. Marín, M. G. da Silva, M. S. Sthel, S. L. Cardoso, H. Vargas, and L. C. M. Miranda, "Application of the thermal wave resonator to the measurement of the thermal diffusivity of gas mixtures," Rev. Sci. Instrum. **72**, 1580 (2001).

[32] Andreas Mandelis, Frank Funak, and Mahendra Munidasa, "Generalized methodology for thermal diffusivity depth profile reconstruction in semi-infinite and finitely thick inhomogeneous solids," J. Applied Phys. **80**, 5570–5578 (1996).

[33] O Pade and A Mandelis, "Thermal-wave slice tomography using wave-field reconstruction," Inverse Problems **10**, 185–197 (1994).

[34] Ricardo Celorrio, Arantza Mendioroz, Estibaliz Apiñaniz, Agustín Salazar, Chinhua Wang, and Andreas Mandelis, "Reconstruction of radial thermal conductivity depth profile in case hardened steel rods," J. Applied Phys. **105**, 083517 (2009).

[35] R. Tai, C. Wang, J. Hu, and A. Mandelis, "Depth profiling of electronic transport properties in $$\mathrm{h}^{+}$$h+-implanted n-type silicon," Int. J. Thermophys. **36**, 967 (2015).

[36] Sreekumar Kaiplavil, Andreas Mandelis, Xueding Wang, and Ting Feng, "Photothermal tomography for the functional and structural evaluation, and early mineral loss monitoring in bones," Biomedical Optics Express **5**, 2488–2502 (2014).

[37] Xinxin Guo, Andreas Mandelis, and Bernard Zinman, "Applications of ultrasensitive wavelength-modulated differential photothermal radiometry to noninvasive glucose detection in blood serum," J. Biophotonics **6**, 911–919 (2013).

[38] J. Kim, A. Mandelis, A. Matvienko, S. Abrams, and B. T. Amaechi, "Detection of dental secondary caries using frequency-domain infrared photothermal radiometry (ptr) and modulated luminescence (lum)," Int. J. Thermophys. **33**, 1778–1786 (2012).

[39] W. Horton, *Turbulent Transport in Magnetized Plasmas* (World Scientific Publishing Company, Singapore, 2012) p. 338.

[40] M Cox, N Deliyanakis, J Hugill, D.C Robinson, M Ashraf, S.J Fielding, H.W Lean, P Mantica, W Millar, M.R O'Brien, B.J Parham, R.A Pitts, A Simonetto, and G Vayakis, "Thermal wave studies of electron transport using modulated ECRH," Nucl. Fusion **33**, 1657–1676 (1993).

[41] E.D. Fredrickson, J.D. Callen, K. McGuire, J.D. Bell, R.J. Colchin, P.C. Efthimion, K.W. Hill, R. Izzo, D.R. Mikkelsen, D.A. Monticello, V. Paré, G. Taylor, and M. Zarnstorff, "Heat pulse propagation studies in TFTR," Nucl. Fusion **26**, 849–862 (1986).

[42] D.J. Gambier, M.P. Evrard, J. Adam, A. Becoulet, S. Corti, P. Hennequin, J. Jacquinot, D.F.H. Start, K. Thomsen, B.J.D. Tubbing, and V. Zanza, "ICRF power deposition profile and determination of the electron thermal diffusivity by modulation experiments in JET," Nucl. Fusion **30**, 23–34 (1990).

[43] L Giannone, V Erckmann, U Gasparino, H.J Hartfuss, G Kuhner, H Maassberg, U Stroth, and M Tutter, "Electron thermal conductivity from heat wave propagation in wendelstein 7-AS," Nucl. Fusion **32**, 1985–2000 (1992).

[44] G. Gorini, P. Mantica, G. M. D. Hogeweij, F. De Luca, A. Jacchia, J. A. Konings, N. J. Lopes Cardozo, and M. Peters, "Simultaneous propagation of heat waves induced by sawteeth and electron cyclotron heating power modulation in the rtp tokamak," Phys. Rev. Lett. **71**, 2038–2041 (1993).

[45] H.J. Hartfuss, H. Maassberg, M. Tutter, and and, "Evaluation of the local heat conductivity coefficient by power-modulated electron cyclotron heating in the wendelstein VII-a stellarator," Nucl. Fusion **26**, 678–684 (1986).

[46] P. Mantica and F Ryter, "Perturbative studies of turbulent transport in fusion plasmas," Comptes Rendus Physique **7**, 634–649 (2006), turbulent transport in fusion magnetised plasmas.

[47] S.D. Song, X.L. Zou, G. Giruzzi, W.W. Xiao, X.T. Ding, B.J. Ding, J.L. Ségui, D. Elbèze, F. Clairet, C. Fenzi, T. Aniel, J.F. Artaud, V. Basiuk, F. Bouquey, R. Magne, and E. Corbel and, "Analysis of electron heat transport with off-axis modulated ECRH in tore supra," Nucl. Fusion **52**, 033006 (2012).

[48] A. Mandelis, "Hamilton–jacobi formulation and quantum theory of thermal wave propagation in the solid state," J. Math. Phys. **26**, 2676–2683 (1985).

[49] A. Salnick and A. Mandelis, "Hamiltonian plasma-harmonic oscillator theory: Generalized depth profilometry of electronically continuously inhomogeneous semiconductors and the inverse problem," J. Applied Phys. **80**, 5278–5288 (1996).

[50] K. Stasiewciz, G. Gustafsson, G. Marklund, P. A. Lindqvist, J. Clemmons, and L. Zanetti, "Cavity resonators and alfvén resonance cones observed on freja," J. Geophysical Res. **102**, 2565 (1997).

[51] T. A. Carter, "Intermittent turbulence and turbulent structures in a linear magnetized plasma," Phys. Plasmas **13**, 010701 (2006).

[52] D. A. D'Ippolito, J. R. Myra, and S. J. Zweben, "Convective transport by intermittent blob-filaments: Comparison of theory and experiment," Phys. Plasmas **18** (2011), 10.1063/1.3594609.

[53] G. S. Xu, V. Naulin, W. Fundamenski, J. Juul Rasmussen, A. H. Nielsen, and B. N. Wan, "Intermittent convective transport carried by propagating electromagnetic filamentary structures in nonuniformly magnetized plasma," Phys. Plasmas **17** (2010), 10.1063/1.3302535.

[54] T. M. Abdalla, B. N. Kuvshinov, T. J. Schep, and E. Westerhof, "Electron vortex generation by strong, localized plasma heating," Phys. Plasmas **8**, 3957 (2001).

[55] S C Thakur, C Brandt, L Cui, J J Gosselin, A D Light, and G R Tynan, "Multi-instability plasma dynamics during the route to fully developed turbulence in a helicon plasma," Plasma Sources Sci. Technol. **23**, 044006 (2014).

[56] Christian Brandt, Olaf Grulke, Thomas Klinger, José Negrete, Guillaume Bousselin, Frédéric Brochard, Gérard Bonhomme, and Stella Oldenbürger, "Spatiotemporal mode structure of nonlinearly coupled drift wave modes," Phys. Rev. E **84**, 056405 (2011).

[57] F. Brochard, T. Windisch, O. Grulke, and T. Klinger, "Experimental evidence of mode coupling in drift wave intermittent turbulence using a wave number bicoherence analysis," Phys. Plasmas **13**, 122305 (2006).

[58] P.H. Diamond, A. Hasegawa, and K. Mima, "Vorticity dynamics, drift wave turbulence, and zonal flows: a look back and a look ahead," Plasma Phys. Control. Fusion **53**, 124001 (2011).

[59] M. Wakatani and A. Hasegawa, "A collisional drift wave description of plasma edge turbulence," Phys. Fluids **27**, 611–618 (1984).

[60] R. E. Waltz, "Numerical study of drift wave turbulence with simple models for wave–wave nonlinear coupling," Phys. Fluids **26**, 169–179 (1983).

[61] J. E. Maggs and G. J. Morales, "Generality of deterministic chaos, exponential spectra, and lorentzian pulses in magnetically confined plasmas," Phys. Rev. Lett. **107**, 185003 (2011).

[62] J. E. Maggs and G. J. Morales, "Origin of lorentzian pulses in deterministic chaos," Phys. Rev. E **86**, 015401 (2012).

[63] J. E. Maggs and G. J. Morales, "Exponential power spectra, deterministic chaos and lorentzian pulses in plasma edge dynamics," Plasma Phys. Control. Fusion **54**, 124041 (2012).

[64] M. Shi, D. C. Pace, G. J. Morales, J. E. Maggs, and T. A. Carter, "Structures generated in a temperature filament due to drift-wave convection," Phys. Plasmas **16**, 062306 (2009).

[65] R. D. Sydora, G. J. Morales, J. E. Maggs, and B. Van Compernolle, "Three-dimensional gyrokinetic simulation of the relaxation of a magnetized temperature filament," Phys. Plasmas **22**, 102303 (2015).

[66] David C. Pace, *Spontaneous Thermal Waves and Exponential Spectra Associated with a Filamentary Pressure Structure in a Magnetized Plasma*, Ph.D. thesis, University of California, Los Angeles (2009).

[67] H. M. Mott-Smith and Irving Langmuir, "The theory of collectors in gaseous discharges," Phys. Rev. **28**, 727–763 (1926).

[68] Francis F. Chen, "Langmuir probe analysis for high density plasmas," Phys. Plasmas **8**, 3029 (2001).

[69] R. L. Merlino, "Understanding langmuir probe current-voltage characteristics," Am. J. Phys. **75**, 1078 (2007).

[70] B. Van Compernolle and G. J. Morales, "Avalanches driven by pressure gradients in a magnetized plasma," Phys. Plasmas **24**, 112302 (2017).

[71] M. J. Poulos and G. J. Morales, "Transport properties of a hollow pressure filament in a magnetized plasma," Phys. Plasmas **23**, 092302 (2016).

[72] M. J. Poulos, "Model for the operation of an emissive cathode in a large magnetized-plasma," Phys. Plasmas **26**, 022104 (2019).

[73] R. D. Sydora, S. Karbashewski, B. Van Compernolle, M. J. Poulos, and J. Loughran, "Drift-alfvén fluctuations and transport in multiple interacting magnetized electron temperature filaments," J. Plasma Phys. **85**, 905850612 (2019).

[74] J. D. Huba, *NRL Plasma Formulary* (Naval Research Laboratory, Washington, DC, 2013) p. 37.

[75] S. Karbashewski, R. D. Sydora, B. Van Compernolle, and M. J. Poulos, "Driven thermal waves and determination of the thermal conductivity in a magnetized plasma," Phys. Rev. E **98**, 051202 (2018).

[76] G. Zhang, J.and Xie, C. Wang, and A. Mandelis, "Laser induced thermal-wave fields in multi-layered spherical solids based on green function method," J. Applied Phys. **112**, 033521 (2012).

[77] L. D. Landau and E. M. Lifshitz, *Mechanics*, 2nd ed., edited by J. B. Sykes and J. S. Bell (Pergamon Press, Oxford, UK, 1969) Chap. 7, pp. 131–154.

[78] H. Goldstein, C. Poole, and J. Safko, *Classical Mechanics*, 3rd ed. (Addison Wesley, San Francisco, USA, 2000) Chap. 8, 10.

[79] O. D. Johns, "Canonical transformations with time as a coordinate," Am. J. Phys. **57**, 204–215 (1989).

[80] J. Struckmeier and C. Riedel, "Invariants for time-dependent hamiltonian systems," Phys. Rev. E **64**, 026503 (2001).

[81] J. Struckmeier and C. Riedel, "Canonical transformations and exact invariants for time-dependent hamiltonian systems," Annalen der Physik **11**, 15–38 (2002).

[82] J. Struckmeier, "Hamiltonian dynamics on the symplectic extended phase space for autonomous and non-autonomous systems," J. Phys. Math. Gen. **38**, 1257–1278 (2005).

[83] A. V. Tsiganov, "Canonical transformations of the extended phase space and integrable systems," Theor. Math. Phys. **124**, 918–937 (2000).

[84] A. V. Tsiganov, "The maupertuis principle and canonical transformations of the extended phase space," J. Nonlinear Math. Phys. **8**, 157–182 (2001).

[85] A. Mandelis, S. B. Peralta, and J. Thoen, "Photoacoustic frequency-domain depth profiling of continuously inhomogeneous condensed phases: Theory and simulations for the inverse problem," J. Applied Phys. **70**, 1761–1770 (1991).

[86] T. de Donder, *Théorie invariante du calcul des variations,*, nuov. ed. (Gauthiers-Villars, Paris, 1935).

[87] H. Weyl, "Geodesic fields in the calculus of variation for multiple integrals," Ann. Math. **36**, 607 (1935).

[88] J. Struckmeier, D. Vasak, and H. Stoecker, "Extended canonical field theory of matter and space-time," Astronomische Nachrichten **336**, 731–738 (2015).

[89] J. Struckmeier, "General relativity as an extended canonical gauge theory," Phys. Rev. D **91**, 085030 (2015).

[90] J. von Rieth, "The hamilton–jacobi theory of de donder and weyl applied to some relativistic field theories," J. Math. Phys. **25**, 1102–1115 (1984).

[91] H. C. Bryant, "Heat waves and ångström's method," Am. J. Phys. **31**, 325–327 (1963).

[92] S. Jin, M. J. Poulos, B. Van Compernolle, and G. J. Morales, "Plasma flows generated by an annular thermionic cathode in a large magnetized plasma," Phys. Plasmas **26**, 022105 (2019).

[93] I. H. Hutchinson, *Principles of Plasma Diagnostics*, 2nd ed., Cambridge (Cambridge University Press, 2002) p. 85.

[94] M. J. Poulos, B. Van Compernolle, and G. J. Morales, "Tornado-like transport in a magnetized plasma," in *APS Meeting Abstracts* (2017).

[95] P. W. Terry, "Suppression of turbulence and transport by sheared flow," Rev. Mod. Phys. **72**, 109–165 (2000).

[96] J.R Peñano, G. J. Morales, and J. E. Maggs, "Properties of drift waves in a filamentary density depletion," Phys. Plasmas **4**, 555 (1997).

[97] J. E. Maggs and G. J. Morales, "Exponential power spectra, deterministic chaos and lorentzian pulses in plasma edge dynamics," Plasma Phys. Control. Fusion **54**, 124041 (2012).

[98] J.P. Nolan, *Univariate Stable Distributions: models for heavy tailed data* (Springer Nature, 2020).

[99] S. Karbashewski, R. D. Sydora, B. Van Compernolle, and M. J. Poulos, "Stimulated excitation of thermal diffusion waves in a magnetized plasma pressure filament," Phys. Plasmas **28**, 092112 (2021).

[100] O. A. Rosso, H. A. Larrondo, M. T. Martin, A. Plastino, and M. A. Fuentes, "Distinguishing noise from chaos," Phys. Rev. Lett. **99**, 154102 (2007).

[101] W. Gekelman, B. Van Compernolle, T. DeHaas, and S. Vincena, "Chaos in magnetic flux ropes," Plasma Phys. Control. Fusion **56**, 064002 (2014).

[102] W. Gekelman, S. W. Tang, T. DeHaas, S. Vincena, P. Pribyl, and R. Sydora, "Spiky electric and magnetic field structures in flux rope experiments," Proc. Natl. Acad. Sci. U.S.A. **116**, 18239–18244 (2019).

[103] P. J. Weck, D. A. Schaffner, M. R. Brown, and R. T. Wicks, "Permutation entropy and statistical complexity analysis of turbulence in laboratory plasmas and the solar wind," Phys. Rev. E **91**, 023101 (2015).

[104] C. Bandt and B. Pompe, "Permutation entropy: A natural complexity measure for time series," Phys. Rev. Lett. **88**, 174102 (2002).

[105] M.T. Martin, A. Plastino, and O.A. Rosso, "Generalized statistical complexity measures: Geometrical and analytical properties," Physica A **369**, 439–462 (2006).

[106] Edward N. Lorenz, "Deterministic nonperiodic flow," J. Atmos. Sci. **20**, 130 – 141 (1963).

[107] H. G Schuster and W. Just, *Deterministic Chaos: An Introduction*, 4th ed. (John Wiley & Sons, 2006).

[108] R. M. May, "Simple mathematical models with very complicated dynamics," Nature **261**, 459–467 (1976).

[109] H. E. Hurst, "Long-term storage capacity of reservoirs," Trans. Am. Soc. Civil Eng. **116**, 770–799 (1951).

[110] Vinita Suyal, Awadhesh Prasad, and Harinder P. Singh, "Nonlinear time series analysis of sunspot data," Solar Phys. **260**, 441–449 (2009).

[111] B. Van Compernolle, W. Gekelman, P. Pribyl, and C. M. Cooper, "Wave and transport studies utilizing dense plasma filaments generated with a lanthanum hexaboride cathode," Phys. Plasmas **18**, 123501 (2011).

APPENDIX A

Green Function Solutions

This appendix presents the derivation of the Green function solutions to Eq. (3.5) for the two geometries of the two-dimensional homogeneous model presented in Section 3.2. The derivations are drawn from solutions of similar geometries presented in Ref. [23] but for isotropic conductivities; the task of repeating for anisotropic conductivities is not difficult but is presented here to stimulate more interest in this approach to thermal waves within the plasma community. The Green function equation for an impulsive ring source at r_0 and z_0 is,

$$\frac{\partial^2}{\partial z^2}\tilde{G} - \frac{\kappa_\perp}{\kappa_\parallel}\frac{1}{r}\frac{\partial}{\partial r}\left(r\frac{\partial}{\partial r}\tilde{G}\right) - k_\parallel(\omega)^2\tilde{G} = -\frac{1}{2\pi\alpha_\parallel r}\delta(r-r_0)\delta(z-z_0) \tag{A.1}$$

where $\tilde{G} = \tilde{G}(r,z|r_0,z_0;\omega) = \mathcal{F}[G(r,z|r_0,z_0;t)]$. We begin with a zeroth-order Hankel transform ($\mathcal{H}_0$) of Eq. (A.1) with respect to the radial coordinate ($r \to \lambda$),

$$\left(\frac{\partial^2}{\partial z^2} - s^2\right)\bar{G} = -\frac{J_0(\lambda r_0)}{2\pi\alpha_\parallel}\delta(z-z_0) \tag{A.2}$$

where $k_\parallel(\omega)$ is defined in Eq. (3.6), $\bar{G} = \bar{G}(\lambda,z|r_0,z_0;\omega) = \mathcal{H}_0[\tilde{G}(r,z|r_0,z_0;\omega)]$, and

$$s = s(k_\parallel,\lambda) = \sqrt{k_\parallel(\omega)^2 + \frac{\kappa_\perp}{\kappa_\parallel}\lambda^2} \tag{A.3}$$

A.1 Semi-infinite Geometry

For the semi-infinite geometry, the conditions on $\bar{G}$ are,

$$\bar{G}\Big|_{z=z_0^+} - \bar{G}\Big|_{z=z_0^-} = 0 \tag{A.4}$$

$$\frac{\partial}{\partial z}\bar{G}\bigg|_{z=z_0^+} - \frac{\partial}{\partial z}\bar{G}\bigg|_{z=z_0^-} = -\frac{J_0(\lambda r_0)}{2\pi\alpha_\parallel} \tag{A.5}$$

$$\frac{\partial}{\partial z}\bar{G}\bigg|_{z=0} = 0 \tag{A.6}$$

Taking into account boundedness at infinity $\bar{G}$ can be solved for using simple techniques,

$$\bar{G} = \begin{cases} A_1 e^{-sz} & z \geq z_0 \\ A_2 e^{sz} + A_3 e^{-sz} & 0 \leq z \leq z_0 \end{cases} \tag{A.7}$$

whereupon solving for the coefficients using the boundary conditions yields,

$$\bar{G}(\lambda, z|r_0, z_0; \omega) = \frac{J_0(\lambda r_0)}{4\pi\alpha_\parallel s}\left(e^{-s|z-z_0|} + e^{-s(z+z_0)}\right) \tag{A.8}$$

Finally, taking the source to be a surface source at $z_0 = 0$ and inverting the Hankel transform gives for the semi-infinite Green function,

$$\tilde{G}_{SI}(r, z|r_0; \omega) = \int_0^\infty \frac{J_0(\lambda r_0) J_0(\lambda r)}{2\pi\alpha_\parallel s} e^{-sz}\lambda \, d\lambda \tag{A.9}$$

which is identical to Eq. (3.12).

A.2 Laterally Infinite Geometry

For the laterally infinite geometry, the conditions on $\bar{G}$ are,

$$\bar{G}\Big|_{z=z_0^+} - \bar{G}\Big|_{z=z_0^-} = 0 \tag{A.10}$$

$$\frac{\partial}{\partial z}\bar{G}\Big|_{z=z_0^+} - \frac{\partial}{\partial z}\bar{G}\Big|_{z=z_0^-} = -\frac{J_0(\lambda r_0)}{2\pi\alpha_\parallel} \tag{A.11}$$

$$\frac{\partial}{\partial z}\bar{G}\Big|_{z=0} = 0 \tag{A.12}$$

$$\bar{G}\Big|_{z=L} = 0 \tag{A.13}$$

$\bar{G}$ takes the form,

$$\bar{G} = \begin{cases} A_1 e^{sz} + A_2 e^{-sz} & z \geq z_0 \\ A_2 e^{sz} + A_3 e^{-sz} & 0 \leq z \leq z_0 \end{cases} \tag{A.14}$$

whereupon solving for the coefficients using the boundary conditions yields,

$$\bar{G}(\lambda, z|r_0, z_0; \omega) = \frac{J_0(\lambda r_0)}{4\pi\alpha_\parallel s(1 + e^{-2sL})} \times \left(e^{-s|z-z_0|} + e^{-s(z+z_0)} - e^{-s(2L-|z-z_0|)} - e^{-s(2L-(z+z_0))}\right) \tag{A.15}$$

Finally, taking the source to be a surface source at $z_0 = 0$ and inverting the Hankel transform gives for the laterally infinite Green function,

$$\tilde{G}_{LI}(r, z|r_0; \omega) = \int_0^\infty \frac{J_0(\lambda r_0) J_0(\lambda r)}{2\pi\alpha_\parallel s(1 + e^{-2sL})} \left(e^{-sz} - e^{-s(2L-z)}\right) \lambda \, d\lambda \tag{A.16}$$

which is identical to Eq. (3.16).

A.3 Thermal Wave Fields

Once the Green functions are known for different geometries the thermal wave field for arbitrary distributions of surface flux sources at $z = 0$ can be found using,

$$\tilde{T}_e(\mathbf{r}, \omega) = \frac{2\pi\alpha_\parallel}{\kappa_\parallel} \int_0^\infty \tilde{q}(r_0, \omega) \tilde{G}(r, z|r_0; \omega) r_0 \, dr_0 \tag{A.17}$$

Substituting $\tilde{q}$ given by Eq. (3.18) and interchanging the integration order on $\tilde{G}$ and $\tilde{T}_e$ yields the integral,

$$\int_0^\infty \Pi_c(r_0, a) J_0(\lambda r_0) r_0 \, dr_0 = a \frac{J_1(\lambda a)}{\lambda} \tag{A.18}$$

which can be recognized as the zeroth-order Hankel transform of the cylinder function Π_c. This reduces the computation to a single integral for both thermal wave fields,

$$\tilde{T}_{eSI}(r, z|r_0; \omega) = \frac{q_0 a}{2\kappa_\parallel} \int_0^\infty \frac{J_0(\lambda r) J_1(\lambda a)}{s} e^{-sz} \, d\lambda \tag{A.19}$$

$$\tilde{T}_{eLI}(r, z|r_0; \omega) = \frac{q_0 a}{2\kappa_\parallel} \int_0^\infty \frac{J_0(\lambda r) J_1(\lambda a)}{s(1 + e^{-2sL})} \left(e^{-sz} - e^{-s(2L-z)}\right) \, d\lambda \tag{A.20}$$

identical to Eqs. (3.19) and (3.20), respectively, and we remind the reader that $s = s(k_\parallel, \lambda)$ is given by Eq. (A.3) and $k_\parallel(\omega)$ is given by Eq. (3.6).

APPENDIX B

Chaotic Systems

In this appendix, we outline the chaotic signals and associated parameters used in the analysis of the complexity-entropy plane and Hurst exponent. These are all common chaotic systems with many resources available for further reading and only a basic description of each is given here.

B.1 Lorenz Attractor

The Lorenz System is a system of ordinary differential equations with solutions that exhibit chaotic behaviour for certain values of the constant parameters within the system; for parameters giving these chaotic solutions it is referred to as the Lorenz Attractor. The system is given by the equations [106],

$$\dot{x} = \sigma(y - x) \tag{B.1}$$

$$\dot{y} = x(\rho - z) - y \tag{B.2}$$

$$\dot{z} = xy - \beta z \tag{B.3}$$

where the system parameters $\rho = 40$, $\sigma = 10$, and $\beta = 8/3$ are used in our analysis to yield chaotic solutions.

B.2 Logistic Map

The Logistic Map is a simple discrete recurrence relation that exhibits chaotic behaviour for certain parameters and is defined as [108],

$$x_{n+1} = r x_n (1 - x_n) \tag{B.4}$$

and the system parameter $r = 3.9076$ is used to generate the chaotic signal used in our analysis.

B.3 Schuster Map

The Schuster Map is another discrete map that exhibits chaotic behaviour described by the relation [107],

$$x_{n+1} = x_n + x_n^Z \pmod 1 \tag{B.5}$$

where the parameter $Z = 3/2$ yields the chaotic series used in our analysis.